Diffusion resistance of claddings for corrosion protection of structural alloys in molten salt reactors

Cedric Eveleigh

Supervisor: Dr. John Luxat

Co-supervisor: Dr. Joey Kish

Department of Engineering Physics

McMaster University

Thesis submitted in partial fulfillment of the requirements for the Degree of

Master of Applied Science

January 2019

McMaster University

Abstract

Corrosion is a major challenge in the use of molten fluoride salt as a coolant in molten salt reactors (MSRs). A promising way of satisfying the two requirements of high strength and corrosion resistance is to clad structural alloys with a corrosion resistant material.

Four candidate cladding and structural alloy combinations—stainless steel 316L and Incoloy 800H structural alloys either diffusion bonded to Hastelloy N or electroplated with nickel—were thermally aged at 700 °C for two to eight months. Based on measured concentration profiles, the diffusion resistance of the four material combinations was compared and diffusion results were extrapolated to an end of reactor lifetime. The most important conclusion from this work is that Hastelloy N is highly likely to be significantly more diffusion resistant than nickel. The difference in diffusion resistance between Incoloy 800H and stainless steel 316L is relatively small.

Two methods were used for extrapolating experimental diffusion results: (1) a diffusion model and calculated diffusion coefficients and (2) simulations with Thermo-Calc DICTRA. Some simulations were carried out with a corrosion boundary condition of near-zero chromium concentration, demonstrating the potential of simulations for predicting diffusion-limited corrosion in molten fluoride salts. A surprising result of these simulations is that decreasing the thickness of Ni plating did not increase the thickness of diffusion zones in underlying structural alloys.

Acknowledgments

I would like to thank Professor John Luxat for encouraging me to explore my research interests both at McMaster and abroad, and Professor Joey Kish for sharing his materials wisdom and for inspiring me to have fun and to be curious. Thanks are also due to Jim Garrett for his help in the labs which made much of this project possible, and to Professor Michael Short of MIT and Luke Olson of Savannah River National Laboratory for the immensely helpful discussions.

I'm deeply grateful to Rob Bodner, David LeBlanc, Steve Shelestynsky, and everyone at Terrestrial Energy whose support made this project possible and whose guidance was crucial for its success. Their willingness to support fledgling engineers such as myself while taking on a massively ambitious project is commendable.

This project was funded through the Mitacs Accelerate program. I thank everyone at Mitacs who is involved with this grant program, and I recommend it to all Canadian engineering graduate students for the real-world, impactful experience that it can provide.

These past two years have been a highlight of my life. Much of this can be attributed to the research experience and graduate student lifestyle—but Koko, my lover and best friend, deserves most of the credit. She has had to tolerate my "never-ending crunch time" more than anyone else, and her patience is something that I will be forever grateful for.

Finally, I wish to thank my parents, Martha and Philippe, for their unconditional support throughout all phases of my life. This work is dedicated to you.

Table of contents

List of figures

List of tables

Nomenclature

Roman Symbols

$\Delta\overline{G}_{F_2}$	Fluorine potential
ΔG°	Standard free energy of formation
a	Activity
C	Concentration
D	Diffusion coefficient
d	Average grain size
D_0	Pre-exponential factor
D_{eff}	Effective diffusion coefficient
D_{gb}	Grain boundary diffusion coefficient
D_l	Lattice diffusion coefficient
D_m	Displacement mixing diffusion coefficient
D_{rad}	Radiation diffusion coefficient
D_{th}	Thermal diffusion coefficient
E_a^{gb}	Grain boundary activation energy
E_a^l	Lattice activation energy
E_a	Activation energy
f	Volume fraction of grain boundaries
l	Minimum thickness for the semi-infinite thickness approximation
p	Partial pressure
q	Numerical factor for grain shape
R	Gas constant
T	Temperature
t	Time
x	Position normal to interface

Greek Symbols

δ	Grain boundary width

Acronyms / Abbreviations

ASME	American Society of Mechanical Engineers
BPVC	Boiler and Pressure Vessel Code
BSE	Backscatter electron
CVD	Chemical vapor deposition
DMSR	Denatured Molten Salt Reactor
dpa	Displacements per atom
EBSD	Electron backscatter diffraction

EDS	Energy-dispersive X-ray spectroscopy
FCC	Face-centered cubic
FHR	Fluoride-salt-cooled high-temperature reactor
FLiBe	$LiF–BeF_2$ (66.7–33.3 mol%)
FLiNaK	LiF–NaF–KF (46.5–11.5–42 mol%)
HVOF	High-velocity oxy-fuel
ID	Inner diameter
IMSR	Integral Molten Salt Reactor
LWR	Light-water reactor
MSR	Molten salt reactor
MSRE	Molten Salt Reactor Experiment
OD	Outer diameter
ORNL	Oak Ridge National Laboratory
PCHE	Printed circuit heat exchanger
PVD	Physical vapor deposition
SE	Secondary electron
SEM	Scanning electron microscope
SS304	Stainless steel 304
SS316	Stainless steel 316

Chapter 1

Introduction

1.1 The importance of molten salt reactors

Molten salt reactors (MSR) are a class of nuclear fission reactors in which the primary reactor coolant is a low-pressure molten salt mixture containing dissolved fuel and fission products. Compared to conventional water-cooled reactors, MSRs have several advantages. First, they have excellent safety characteristics, such as small quantities of volatile fission products contained in the fuel, low vapor pressure and high heat capacity of molten salt, and the possibility of passive cooling for removal of decay heat. These safety characteristics may enable MSRs to be more economically competitive than water-cooled reactors. Second, MSRs consume less fuel resources and produce less nuclear waste than water-cooled reactors because of the higher energy conversion efficiency that comes with higher temperature operation (around 650 °C in MSRs versus 300 °C in water-cooled reactors) and because of the higher burnup enabled by continuous removal of fission products (e.g. xenon, which bubbles out of salt). Third, MSRs could reduce the cost of breeding fuel cycles where actinides are partitioned and transmutated, resulting in high resource efficiency and drastically reduced quantities and radiotoxicity of nuclear waste. Fourth, MSRs make possible the use of thorium as nuclear fuel—a significant advantage for countries with limited uranium reserves,

such as China and India[1]. Fifth, MSRs can be used for powering industrial processes that require high-temperature heat. To summarize, MSRs are safer, cleaner, more versatile, and potentially cheaper than conventional water-cooled reactors.

There are multiple MSR R&D efforts around the world. Large government-funded programs are underway in China and India. In western nations, there are several startups pursuing MSR designs, one of which is Terrestrial Energy, headquartered in Oakville, Ontario. This research project was supported by Terrestrial Energy (with matching funds from the Canadian government) and is therefore oriented towards being applicable to Terrestrial Energy's MSR design, but this research is nonetheless broadly applicable to fluoride-salt-cooled reactors.

1.2 Introduction to materials challenges for molten salt reactors

One of the main technological uncertainties in the development of MSRs is the performance and reliability of materials after years of exposure to high temperatures (550–750 °C), irradiation, and fuel-bearing molten fluoride salt. This challenge is complemented by a strong economic incentive to develop materials with maximized durability because their useful lifetime puts an upper limit on the economic competitiveness of MSRs.

For most MSR designs, the two main materials exposed to fuel salt are structural alloys and graphite (moderator). Graphite does not react with salt, but it does present a challenge due to irradiation-induced volume changes, and it can absorb molten salt and volatile fission products such as xenon.

The requirements for structural alloys in MSRs are high-temperature strength, formability, weldability, irradiation resistance, and corrosion resistance to molten fluoride salts without

[1]The drawback of thorium fuel cycles is potentially difficult nuclear safeguarding, contrary to what is often touted in the media. For more information, see Section 10.4.2 of [1].

being prohibitively expensive. Unfortunately, most high-temperature alloys have been developed for corrosion resistance in oxygen environments and lack corrosion resistance in molten fluoride salts. This is because the corrosion behavior of molten fluoride salts is fundamentally different than that of oxygen environments: The surface oxide layers that are protective in oxygen environments are stripped by molten fluoride salts, and the chromium that is added to encourage surface oxide formation in oxygen environments is selectively attacked by molten fluoride salts. Along with chromium depletion, intergranular void networks have been observed to form up to hundreds of micrometers in depth for various stainless steels and nickel-based alloys as a result of molten fluoride salt exposure.

The conditions that accelerate corrosion rates are presence of free fluorine (oxidant), thermal gradients, water and other impurities, nuclear fuel, irradiation, and dissimilar materials in contact with the same salt; these are discussed in Section 2.1. Simulating the worst corrosion environment in MSRs is extremely difficult because the aforementioned conditions can behave synergistically. Flowing salt loops are commonly used for investigating thermal-gradient-induced corrosion, and research reactors or prototype reactors are needed for neutron irradiation. The MITR research reactor at MIT and the High Flux Reactor at Petten in the Netherlands are equipped for in-core, static (non-flowing) molten salt corrosion tests where materials are simultaneously exposed to irradiation and molten salt. There are plans to equip the Petten reactor with a flowing loop of uranium-containing salt. To give an understanding of how these research methods compare, Figure 1.1 illustrates the various levels of MSR corrosion research with time and funding requirements increasing from the bottom-up.

Structural alloys that are used in nuclear reactors must be approved by nuclear regulators, and nuclear regulators require these alloys to be included in specific codes and standards, such as the Boiler and Pressure Vessel Code (BPVC) from the American Society of Mechanical Engineers (ASME), which have specifications for allowed usage conditions. The few alloys

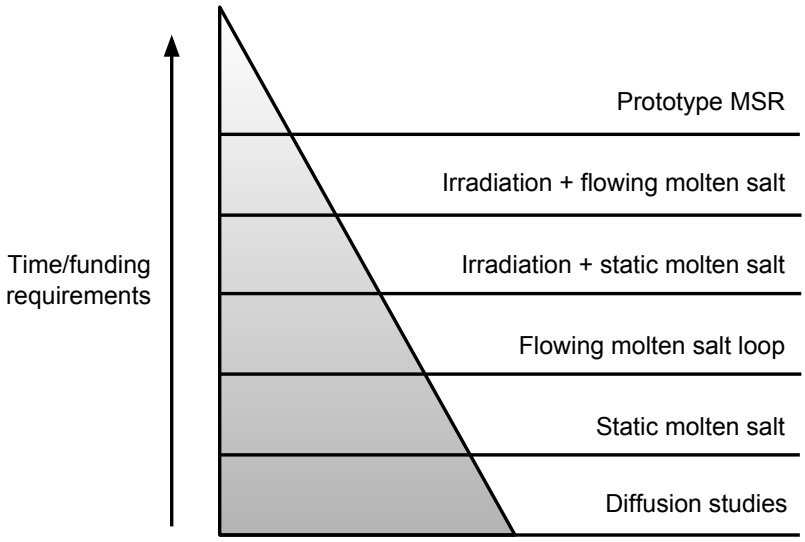

Figure 1.1: The various levels of materials research for MSRs, where "static/flowing molten salt" refers to corrosion tests exposing materials to molten salt, and "diffusion studies" refers to thermal aging experiments without salt exposure.

that are codified in the ASME BPVC for high-temperature use in nuclear reactors have undesirably high chromium content. The challenge for near-term MSR commercialization efforts, such as Terrestrial Energy's IMSR®, is that these codified alloys are the only option if the expensive process of codifying another alloy is to be avoided. If codified alloys are used, it may be possible to sufficiently limit corrosion by controlling the redox potential of molten salt coolants (i.e. redox control). There are three factors that limit the viability of this approach:

1. There is limited information about the corrosion resistance of codified alloys in molten fluoride salt that is flowing, redox-controlled, bears fuel and fission products, and is exposed to dissimilar material, such as graphite.
2. The cost of reactor-scale redox control systems is uncertain. A requirement for aggressive redox control may significantly increase reactor cost.

3. The extent to which fuel-bearing salt can be made reducing is limited by reactions of uranium precipitation and formation of uranium-carbides (at the surface of the graphite core).

1.3 The case for cladding heat exchanger tubes

> The increasing demands in advanced nuclear applications (temperature, corrosive environment) can most probably only be accommodated with surface protection.
>
> Wolfgang Hoffelner, *Materials for Nuclear Plants*

An approach that avoids the challenges of exposing codified structural alloys to fuel salt is cladding these with a non-codified corrosion resistant material. Since the presence of fuel and fission products in fuel salt complicates the task of preventing corrosion (discussed in Section 2.1), claddings are most needed on materials exposed to fuel salt[2]. And among the reactor components exposed to fuel salt, primary heat exchanger tubes are in most need of corrosion protection because of their thin walls and their exposure to severe thermal conditions. The reliability of these tubes must be outstanding because heat exchangers are directly related to overall system efficiency and safety. An example of clad tubes is shown in Figure 1.2.

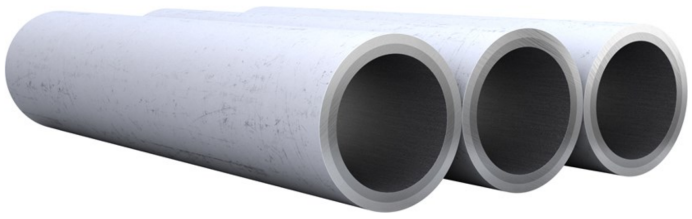

Figure 1.2: Clad tubes manufactured by Sandvik (sleeve coextrusion process). These are also known as composite tubes. [2]

[2]If temperatures are high enough (e.g. 850 °C), claddings are also advantageous on materials exposed to non-fuel-bearing salts. For example, claddings are of interest for high-temperature operation of fluoride-salt-cooled high-temperature reactors (FHR), which use molten salts to cool solid fuel and not as a fuel-bearing medium.

Claddings can improve heat exchanger performance by reducing wall thickness requirements, they enable the use of less corrosion resistant but stronger structural alloys (e.g. Incoloy 800H instead of stainless steel 316H), and they allow for more latitude in system operating parameters of temperature and salt redox potential. The high-temperature operation advantage of claddings is exemplified in a paper by Greene et al. [3] on salt-cooled reactors, where Hastelloy N is suggested for 700 °C operating temperatures and nickel-clad high-temperature alloys (and other advanced materials) are suggested for 850 °C operating temperatures. For components such as reactor vessels, claddings may serve to reduce reactor costs by enabling the use of less corrosion-resistant structural alloys that are less expensive, such as stainless steel 304H [4].

The focus of this research is on the application of claddings to heat exchanger tubes even though they are applicable to other components in MSRs (e.g. reactor vessels). Tubes aren't used in some types of heat exchangers, such as printed circuit heat exchangers (PCHE) and plate heat exchangers, but these are less technologically mature than tubular heat exchangers and are less likely to be employed. The primary heat exchanger of the molten salt reactor experiment (MSRE) at Oak Ridge National Laboratory (ORNL) used a shell and tube design; the assembled tube bundle is shown in Figure 1.3. Furthermore, the focus of this research is on the application of claddings for molten fluoride salt corrosion protection. This is specified because there are additional application for claddings in MSRs, such as tritium permeation prevention[3] and corrosion protection in chemical fuel processing equipment[4].

Claddings have been used in the nuclear industry for corrosion protection of steel components exposed to water. Siemens pressure vessels use stainless steel claddings in control rod drive mechanism nozzles fabricated by coextrusion. Some light-water reactor (LWR) pressure vessels use stainless steel weld overlay claddings on wetted surfaces to prevent

[3] At MSR temperatures, tritium diffuses through structural alloys, and primary heat exchangers are a significant escape path. Therefore, heat exchanger tubes could be clad with a tritium-permeation-resistant material, such as tungsten silicide [5].

[4] An example fuel processing corrosion medium is liquid bismuth, for which tungsten or molybdenum claddings might be used [6, Sec. 16.6].

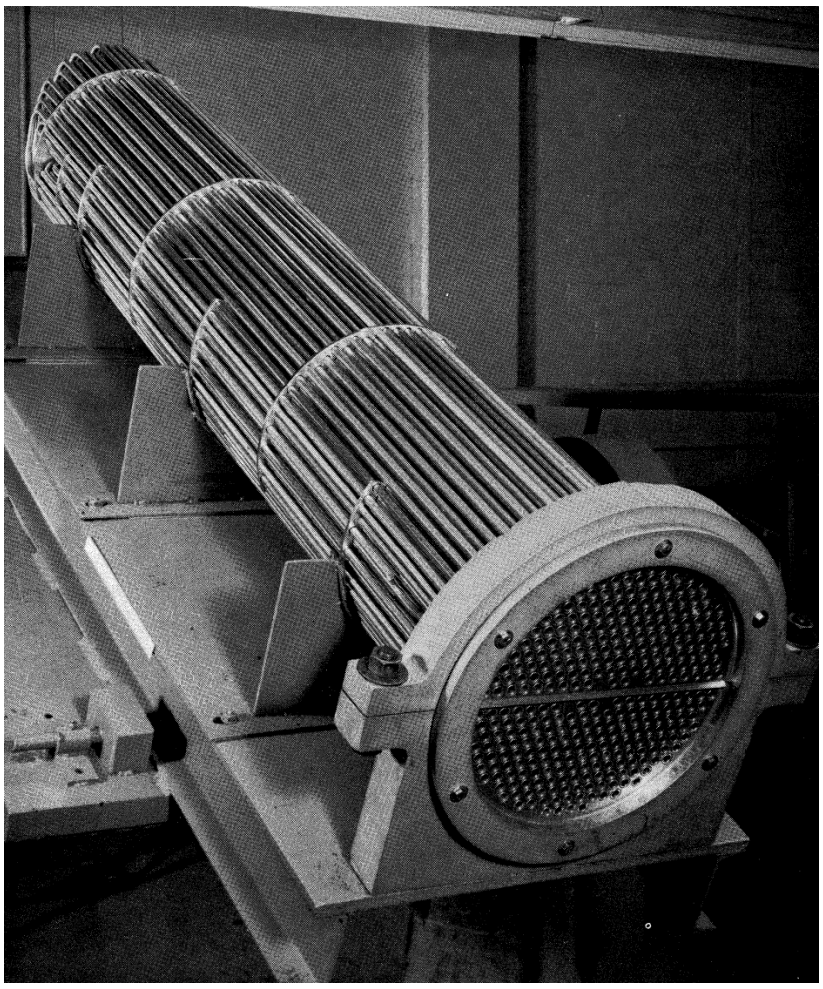

Figure 1.3: MSRE primary heat exchanger tube bundle fabricated out of Hastelloy N (called INOR-8 at the time). The tube bundle is roughly 2.5 m long. [7]

corrosion. The experience base for claddings in nuclear reactors could aid the development of claddings for MSRs—for example, by informing about required technology readiness demonstrations.

Molten fluoride salts have been proposed for use in solar power towers [8] and in fusion reactors [9], and claddings developed for MSRs may also be applicable to these energy systems. The molten nitrate salts currently used in solar power towers are stable only up to around 600 °C. Higher temperature operation (e.g. 750 °C) would improve the economics of concentrated solar power towers by increasing energy conversion efficiency. However, higher temperature operation requires the use of alternate salts, such as fluoride, chloride, or carbonate salts. For fusion reactors, molten LiF-BeF_2 (66-33 mol%) salt (FLiBe) could be used as a self-cooled tritium breeder in a fusion blanket system [9]. Concentrated solar power towers are limited by a need for direct sunlight (no clouds) and are subject to seasonal intermittency, and fusion reactors are a long-term endeavor whose economics have yet to be proven, but these are nonetheless promising as non-carbon-emitting sources of power. These additional applications of claddings for corrosion protection in fluoride salts add to the value of developing the technology.

1.4 Performance requirements for claddings

Claddings on primary heat exchanger tubes must satisfy the following performance requirements for the operating lifetime of a reactor:

1. **Corrosion resistance:** Claddings should consist of elements that are thermodynamically stable with low solubility in molten fluoride salts (e.g. nickel and molybdenum).
2. **Irradiation resistance:** Claddings should satisfy the performance requirements in this list while exposed to expected irradiation conditions. This includes satisfying corrosion resistance requirements when corrosion is accelerated by synergistic effects

with irradiation, and it includes satisfying mechanical integrity requirements despite any irradiation-induced embrittlement.

3. **Resistance to fission-product-induced embrittlement:** Claddings should be resistant to intergranular embrittlement from tellurium and other elements that are present in fuel salt.

4. **Minimal neutron absorption:** Cladding materials should not be neutron poisons so as to avoid affecting reactor physics.

5. **Mechanical integrity:** Claddings should be free of pinholes, voids, surface cracks, and significant internal cracks that could cause a breach in the corrosion barrier. This implies that claddings must have sufficient ductility so as to avoid cracking or delamination, and must remain ductile upon exposure to high temperatures for extended periods of time (i.e. must not excessively embrittle when thermally aged).

6. **Thermal expansion:** The thermal expansion coefficients of claddings must be reasonably close to those of structural alloy substrates to minimize thermal stresses and to maximize thermal fatigue resistance.

7. **Substrate compatibility:** Claddings must have excellent adhesion to structural alloy substrates, and the interface should be ductile. The material in interfacial diffusion zones should not undergo microstructural changes which could jeopardize mechanical integrity.

8. **Wear resistance:** Cladding materials must be hard enough to resist fretting wear from heat exchanger tube vibrations and abrasive wear from coolant flow.

9. **Diffusional resistance:** Cladding materials should resist diffusion in order to minimize the rate at which corrosion-prone elements reach salt–cladding interfaces and to minimize the growth rate of the diffusion zone in underlying structural alloys.

10. **Minimal thickness:** The thickness of claddings should be minimized. The fact that the structural layer must provide all of the strength for the composite means that the composite must be slightly thicker than the same part made out of the bare structural alloy. In heat exchangers, this increased thickness results in worse heat transfer and increased pump work due to greater pressure drops.
11. **Uniform thickness:** Claddings must have reasonably uniform thickness to enable conformation to engineering design specifications.
12. **Weldability:** If clad heat exchanger tubes will be welded to tubesheets, the properties of the weld interface must be known.
13. **Cost:** Claddings must be affordable and industrially scalable. Ideally, they should be commercially available with a minimum of setup and development cost.

1.5 Outline

Chapter 2 presents the background information necessary to understand various aspects of this thesis. Chapter 3 details the methods and parameters used in experiments and subsequent analysis. Chapter 4 presents results of microstructural analysis and diffusion measurements for cladding and structural alloy composites. Chapter 5 presents a discussion of the reliability of the diffusion experiment and it presents the results of extrapolating experimental diffusion results to a seven-year reactor lifetime. Chapter 6 summarizes the results of this thesis, mainly with respect to the diffusion resistance of the composites, and includes recommendations for future work.

Chapter 2

Background

2.1 Characteristics of molten fluoride salt corrosion

The surface oxide layers usually relied upon for corrosion protection are stripped by molten fluoride salts. Exposed metal must therefore be intrinsically resistant to dissolving into salt as metal fluorides—that is, metal fluoride corrosion products must be thermodynamically less stable than the components of the salt (less negative free energy of formation). However, satisfying this condition alone is not enough to determine if and how much corrosion occurs. To fully understand corrosion in molten fluoride salts, we must look at the various corrosion mechanisms, the four types of which are intrinsic corrosion, impurity-driven corrosion, dissimilar material corrosion, and thermal-gradient-driven corrosion [10, 11]. Erosion corrosion (mechanical abrasion) is an additional corrosion mechanism that should also be considered, although it isn't specific to fluoride salts and it won't be discussed here. In the rest of this section, the four corrosion mechanisms in fluoride salts are described, and the corrosion behavior of fuel salt versus secondary ("clean") salt is discussed.

Intrinsic corrosion

Intrinsic corrosion is the most basic corrosion mechanism in that it involves only the metal exposed to salt, chemically pure salt, and the salt's fluorine potential. As such, it is "intrinsic" and does not involve impurities in the salt, dissimilar materials exposed to the same salt, or thermal gradients. Intrinsic corrosion is described by the following generalized oxidation reaction in molten fluoride salts, where M is a metal such as chromium [12]:

$$\mathrm{MF_n} + \frac{1}{2}\,\mathrm{F_2(g)} = \mathrm{MF_{n+1}} \quad \text{where } 0 \leqslant n \leqslant 4. \tag{2.1}$$

For a given temperature, the extent of possible intrinsic corrosion is governed by the standard Gibbs free energy of formation of the corrosion product and by the fluorine potential (redox condition) of the system [12]. The equilibrium activity (concentration) of a metal fluoride corrosion product ($a_{\mathrm{MF_2}}$) in salt is related to its standard free energy of formation ($\Delta G^{\circ}_{\mathrm{MF_2}}$) and the fluorine potential of the system ($\Delta\overline{G}_{\mathrm{F_2}}$):

$$RT \ln a_{\mathrm{MF_2}} = \Delta\overline{G}_{\mathrm{F_2}} - \Delta G^{\circ}_{\mathrm{MF_2}} \tag{2.2}$$

This equation gives the activity of $\mathrm{MF_2}$ that is in equilibrium with the pure metal M when the temperature and fluorine potential of the system are specified. The Gibbs free energy of formation of salt fluorides and structural metal fluorides are listed in Table 2.1. Of the elements found in significant quantities in the alloys considered for use in MSRs, chromium has the most stable fluoride and is therefore most prone to being attacked by molten fluoride salts. Iron is also prone to attack, although to a lesser extent than chromium. A similar list with more metal fluorides but for values limited to 1000 K is found in [13, p. 155].

Unlike the standard Gibbs free energy of formation of metal fluorides, fluorine potential is variable and can be controlled. One way of thinking about fluorine potential is in terms

Table 2.1: Gibbs free energies of formation of metal fluorides for the temperature range of 773 K to 1000 K, ordered from most to least stable. [14]

	Compound[a]	ΔG° (kJ/mol-F)	ΔG° (1000 K) (kJ/mol-F)
Diluent fluorides	$LiF_{(l)}$	$-593.3 + 6.95 \times 10^{-2}\,T$	-524
	$ThF_{4\,(d)}$	$-513.8 + 6.51 \times 10^{-2}\,T$	-449
	$BeF_{2\,(l)}$	$-510.2 + 6.28 \times 10^{-2}\,T$	-447
	$UF_{3\,(d)}$	$-471.4 + 5.62 \times 10^{-2}\,T$	-415
	$UF_{4\,(d)}$	$-466.4 + 6.06 \times 10^{-2}\,T$	-406
	$ZrF_{4\,(d)}$	$-473.8 + 6.81 \times 10^{-2}\,T$	-406
Structural metal fluorides	$CrF_{2\,(d)}$	$-359.4 + 4.48 \times 10^{-2}\,T$	-315
	$FeF_{2\,(d)}$	$-323.6 + 4.56 \times 10^{-2}\,T$	-278
	$NiF_{2\,(d)}$	$-307.3 + 7.59 \times 10^{-2}\,T$	-231
	$MoF_{6\,(g)}$	$-258.6 + 4.85 \times 10^{-2}\,T$	-210

[a] The standard state for LiF and BeF_2 is the molten $2\,LiF \cdot BeF_2$ liquid; that for $MoF_{6\,(g)}$ is the gas at one atmosphere; that for all species with subscript (d) is that hypothetical solution with the solute at unit mole fraction and with the activity coefficient it would have at infinite dilution.

of partial pressure of fluorine gas[1]. Equation 2.3 is the relation between fluorine potential and partial pressure (p_{F_2}) [12]. Combined with Equation 2.2, we can see that for a higher equilibrium concentration of free fluorine (F_2), there must be a higher equilibrium concentration of corrosion product. And as discussed earlier, the less negative the Gibbs free energy of formation of the exposed metal, the less it will tend to be corroded.

$$\Delta\overline{G}_{F_2} \equiv RT \ln p_{F_2} \tag{2.3}$$

Three ways of controlling a salt's fluorine potential are (1) controlling the ratio of a H_2/HF gas in contact with the salt, (2) exposing the salt to its constituent metals in metallic form (e.g. Be or Li for FLiBe), and (3) controlling the ratio of a minor salt constituent such as CeF_3/CeF_4 or UF_3/UF_4. The thermodynamics of these methods are described in [12].

[1] It is not necessary that F_2 be physically present in the system—a metal and its fluoride can be enclosed in a gas-free container, yet still exhibit a fluorine pressure [12].

The control of fluorine potential is a central part of corrosion control in MSRs. The importance of fluorine potential is underlined by the need for it to be defined in order for corrosion data to be interpreted. However, there are limits to the extent to which corrosion can be limited with redox control, in particular for fuel-bearing salt. Overly reducing fluoride salt will tend to precipitate metallic uranium and cause formation of uranium carbides in reaction with graphite moderator material [1, p. 201]. The fluorine potential in fuel salts must be kept within a range, with the size of that range (and the challenge of redox control) depending on the corrosion resistance of exposed metals, among other factors.

Impurity-driven corrosion

Impurities have been observed to significantly increase corrosion rates in molten fluoride salts. Moisture impurities are particularly problematic because water reacts with alkali fluorides[2] (for example, LiF) to form highly corrosive hydrofluoric acid [16]:

$$\mathrm{LiF} + \mathrm{H_2O} \longrightarrow \mathrm{LiOH} + \mathrm{HF} \tag{2.4}$$

$$2\,\mathrm{LiF} + \mathrm{H_2O} \longrightarrow \mathrm{Li_2O} + 2\,\mathrm{HF} \tag{2.5}$$

The hydrofluoric acid can then react with structural metal constituents (for example, Cr):

$$2\,\mathrm{HF} + \mathrm{Cr} \longrightarrow \mathrm{CrF_2} + \mathrm{H_2} \tag{2.6}$$

Tritium from transmutation reactions is another source of hydrogen for hydrofluoric acid formation. Impurity-driven corrosion is also caused by metal fluoride impurities such as

[2]For an explanation of the Lewis acid-base property of salts, see [15, pp. 51–54] or [10, p. 244]. ZrF_4 and BeF_2 are examples of Lewis acids and LiF is an example of a Lewis base.

NiF_2 and FeF_2:

$$Cr + NiF_2 \longrightarrow CrF_2 + Ni \tag{2.7}$$

$$Cr + FeF_2 \longrightarrow CrF_2 + Fe \tag{2.8}$$

or oxide films initially present on metals exposed to salt [14]:

$$NiO + BeF_2 \longrightarrow NiF_2 + BeO \tag{2.9}$$

followed by Equation 2.7 in the case of NiF_2. While these are some of the more important impurity-driven corrosion reactions, there are several more described in [10, 13, 14].

An important aspect of impurity-driven corrosion is that it proceeds until virtually all impurities have been reacted, and this can be early relative to the useful life of MSR fuel salt, depending on initial salt purity and the amount of inleakage of impurities.

Thermal-gradient-driven corrosion

Thermal-gradient-driven corrosion is caused by the temperature dependence of the solubility of corrosion products in salt, and it is characterized by material removal at higher temperatures and deposition at lower temperatures in components such as heat exchangers. While material removal at high temperatures can jeopardize structural integrity, material deposition at low temperatures can interfere with proper heat transfer and reactor operation.

In fuel salts, thermal-gradient driven corrosion can proceed by the temperature-dependent[3] reaction of UF_4 with chromium [14]:

$$Cr + 2\,UF_4 \rightleftharpoons 2\,UF_3 + CrF_2 \tag{2.10}$$

[3]The temperature dependence of this reaction depends on salt composition; the equilibrium constant is higher for NaF–LiF–KF–UF_4 than LiF–BeF_2–UF_4 [14].

Unlike impurity-driven corrosion, thermal-gradient driven corrosion is a sustained mechanism, and it can become the dominating corrosion mechanism once impurities have been reacted. For instance, Equation 2.10 was found to be the dominating corrosion mechanism in thermal convection loop tests described in [17]. Hence, "sealed isothermal tests are not a measure of sustained corrosion as might be seen in real engineered heat transfer systems" [18].

Dissimilar material corrosion

Dissimilar material corrosion occurs when certain pairs of dissimilar materials are in direct contact with the same salt. According to Ai et al. [19], the main dissimilar corrosion mechanism is nonelectric transfer when the dissimilar materials are electrically isolated, and a second mechanism is galvanic corrosion which accelerates corrosion when dissimilar materials are in electrical contact. The experiments of Ai et al. [19] are the only ones known to have differentiated the two mechanisms of dissimilar material corrosion by testing with and without electrical contact. There is potential for more work in this area.

With regard to claddings, a critical example of dissimilar material salt exposure is between structural alloys and claddings. In the event of a breach in claddings (e.g. hole or crack), dissimilar material corrosion will cause the underlying structural alloy to corrode more quickly than if there was no cladding at all. For this reason, it is crucial for claddings to be examined for absence of discontinuities prior to their use in reactors and for claddings to remain intact during reactor operation.

Corrosion behavior of fuel salt versus secondary salt

There are three main differences in corrosion behavior between fuel salt and secondary salt: (1) redox control of fuel salt is challenging and limited, so fuel salt is generally more

corrosive, (2) fuel salt contains fission products which deposit and can be protective or can cause embrittlement, and (3) irradiation may affect corrosion rates.

Corrosion control in fuel-bearing salts is complicated by the fact that the fission of actinides affects redox potentials. The reason for this is described in a 1995 ORNL report titled "Molten fluoride fuel salt chemistry" [20]:

> Redox control would be a simple matter were it not for the fact that fission of the actinides produces changes in the redox potential of the melt. This arises because, for example, in the case of UF_4 fissioning, the net oxidation state of the fission products is less than four and yet four fluorine atoms are released, leaving a slightly oxidizing event for each fission. In the case of PuF_3 fission, it is expected that the net oxidation state of the fission products will be slightly greater than three while only three fluorine atoms are released to produce a slightly reducing event for each fission.

In the MSRE, noble metal fission products plated out into an angstrom-thick layer on Hastelloy N components, and this deposit was hypothesized to have slowed corrosion [21, p. 129]. This effect of fission products on corrosion rates may partially alleviate the redox control challenges associated with fuel-bearing salts[4].

An important difference between fuel salt and secondary salt is the presence of neutron irradiation in fuel salt. The literature on the effect of irradiation on fluoride salt corrosion rates is scarce despite the MSRE because the salt in non-irradiation corrosion tests does not match the greater corrosiveness of the MSRE fuel circuit [22, p. 79]. A Hastelloy N corrosion loop experiment was conducted with the Oak Ridge Research Reactor for a few hundred hours with $^7LiF–BeF_2–ZrF_4$ (64.8–30.1–5.1 mol%) salt, and "there was no indication of any aggravation of corrosion by irradiation" [23, Sec. 15.6]. Zhu et al. [24] investigated the microstructural effects of irradiating GH3535 (Chinese-made Hastelloy N) with helium ions

[4]The drawback is that fission products can be highly radioactive, and upon deposition, impart this property to reactor components.

and exposing it to molten LiF-NaF-KF (46.5-11.5-42 mol%) eutectic salt (FLiNaK salt). The irradiation introduced helium bubbles and cavities into the microstructure, which greatly increasing intragranular corrosion. The problem with charged-particle irradiation studies is that results may be neutron-atypical. Zheng et al. [25] performed static corrosion tests of SS316L and Hastelloy N in FLiBe salt both out-of-reactor and in a neutron radiation field in the MIT reactor, and the neutron irradiation was found to significantly accelerate corrosion. There is a need for more research on the effect of neutron irradiation on molten fluoride salt corrosion.

Synergy of corrosion mechanisms

Accurate simulation of the worst corrosion conditions in MSRs requires irradiation, temperature gradients, dissimilar materials, and control of redox potential and chemical composition (including impurities, fuel, and fission products). Synergistic effects, such as from combining irradiation with salt exposure, make it difficult to claim conservative in-reactor corrosion rates from corrosion tests that do not reproduce all of the aforementioned conditions.

2.2 Cladding durability

The purpose of claddings is to protect structural alloys from corrosion. The most obvious way in which claddings can fail at this purpose is by having been breached—for example, by delamination and cracking. If maintaining mechanical integrity isn't the bottleneck, the durability of claddings is determined by their ability to prevent underlying structural alloys from forming diffusion- or corrosion-induced voids or from undergoing excessive change in composition. In such a case, the durability of claddings should be thought of as the durability of structural alloy and cladding systems (referred to as *composites* in this thesis).

Chromium is prone to dissolving into molten fluoride salts, and the durability of composites can be limited by their resistance to chromium diffusion from the structural alloy, through the cladding layer, and into molten salt. Figure 2.1 illustrates a chromium concentration profile in a composite that initially has less chromium in the cladding than in the structural alloy. In this thesis, the *diffusion zone in the structural alloy* is the layer of structural alloy that cannot be considered to contribute structurally due to excessive change in composition. The use of claddings and structural alloys that are more diffusion resistant results in slower growth of the diffusion zone in the structural alloy and less required initial structural alloy thickness to compensate for the lost material. It should be noted that other elements than chromium may determine the maximum thickness of structural alloy that has been compositionally jeopardized. The emphasis is placed on chromium because it is a major alloying element in candidate structural alloys and because its diffusion is accelerated by leaching into salt.

Some elements that do not get leached into salt, such as carbon, can have their concentration homogenize throughout a composite without excessive change of their concentration in the structural alloy. However, for elements that do get leached into salt, such as chromium, homogenization implies near-zero concentration throughout the composite (an undesirable outcome).

2.2.1 Defining the diffusion zone in structural alloys

Having established the concept of the diffusion zone in clad structural alloys, the question becomes: What change in composition of a structural alloy is required for it to no longer be considered to contribute structurally? At first, one would assume the answer is provided by the alloy composition specifications in the relevant code, such as the ASME BPVC (e.g. for chromium in stainless steel 316H, the specification is 16–18 wt%). However, these composition specifications are not practical as a threshold for determining whether a structural alloy is compositionally jeopardized because the initial composition of structural alloys can

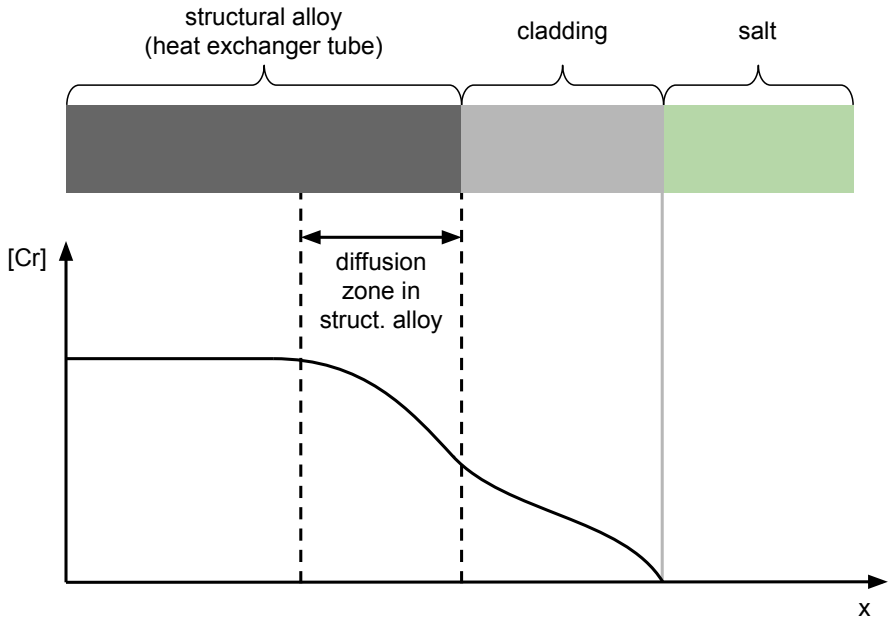

Figure 2.1: Schematic illustration of chromium diffusion from a structural alloy, through a cladding, and into salt. The diffusion zone in the structural alloy is the thickness of structural alloy that can no longer be considered to contribute structurally. The boundary condition of near-zero chromium concentration assumes that the corrosion is diffusion-limited—i.e. diffusion of chromium to the salt–cladding interface is slower than the chemical reactions forming chromium fluoride and the transport of chromium fluoride away from the salt–cladding interface.

be anywhere in the specified ranges, so diffusion zone thickness would vary depending on initial alloy composition. To illustrate the point, a batch of nickel-clad structural alloy could theoretically have exactly the lower limit of a composition specification (e.g. 16 wt% for stainless steel 316H), and as soon as diffusion starts, the entire alloy could not be considered to contribute structurally (i.e. the diffusion zone would be as thick as the structural alloy layer).

There is probably flexibility built into regulator requirements for defining the diffusion zone in structural alloys. No guidelines from ASME could be found for allowable diffusion-induced compositional change, but guidelines can be inferred from those for corrosion allowance found in ASME B31.1 [26]: "When corrosion or erosion is expected, an increase in wall thickness of the piping shall be provided over that required by other design requirements. This allowance *in the judgment of the designer* shall be consistent with the expected life of the piping." (emphasis added). It follows that allowable diffusion-induced composition change could be decided by reactor design engineers.

A practical definition of the diffusion zone in structural alloys is the depth of material that has undergone enough compositional change for it to have lost the mechanical properties that characterize the alloy. For example, if a structural alloy is precipitation-strengthened, the amount of compositional change at which it starts losing precipitates and their strengthening effect could be the limit that defines the diffusion zone.

2.2.2 Diffusion theory and modeling

The purpose of modeling diffusion is to determine the coefficients that allow for quantitative comparisons of the diffusion resistance of claddings and structural alloys and to predict diffusion for longer durations than thermal aging or corrosion experiments. Diffusion modeling is also used for predicting diffusion at different temperatures than in experiments and for the same materials but with different grain sizes.

The textbook *Diffusion in Condensed Matter* by Heitjans and Kärger [27] includes a detailed description of the diffusion theory. This section presents the concepts that are relevant to the diffusion alloying elements between structural alloys and claddings in MSRs.

For the simplest scenario where diffusion coefficients are independent of the concentration of the diffusing species, the change in concentration C at a given location x in the diffusion gradient is described as

$$\frac{\partial C}{\partial t} = D\frac{\partial^2 C}{\partial x^2} \tag{2.11}$$

where D is the diffusion coefficient. In reality, the diffusion coefficient depends on concentration because diffusion is proportional to the gradient of chemical potential, which is directly proportional to the logarithmic gradient of concentration [27]. Concentration-dependent diffusion coefficients are termed interdiffusion coefficients (or chemical diffusion coefficients) and they are represented by the symbol $\tilde{D}$. For simplifying the task of measuring diffusion coefficients, they can be approximated as concentration-independent ($\tilde{D} \approx D$). However, doing so can result in significant error. If it's known that diffusion coefficients are highly concentration-dependent, inaccuracy is avoided by using Boltzmann–Matano analysis to numerically calculate concentration-dependent interdiffusion coefficients from concentration profiles for binary or multicomponent systems using the equations in [28, pp. 175–179].

The following equation is the solution to Equation 2.11, describing the concentration profile of an element diffusing from one layer of material into another at time t [29].

$$C(x,t) = \frac{C_{base}}{2}\operatorname{erfc}\left(\frac{x}{2\sqrt{Dt}}\right) \tag{2.12}$$

C_{base} is the initial concentration of the diffusing element in the base alloy, with zero initial concentration in the cladding. The x-axis has its origin at the interface of the two layers[5] and

[5]More rigorously, the origin of the x-axis (called the Matano interface) is the interface where there is a balance of mass; that is, where the amount of diffusing species lost on one side is equal to the amount gained on the other side [30].

is positive towards the cladding. If the cladding has an initial concentration of the diffusing element (C_{clad}), Equation 2.12 takes the following, more general form:

$$C(x,t) = C_{clad} + \frac{C_{base} - C_{clad}}{2} \text{erfc}\left(\frac{x}{2\sqrt{Dt}}\right) \tag{2.13}$$

The time-dependence of Equation 2.13 is illustrated in Figure 2.2. If thermal aging time is known, the diffusion coefficient D can be determined by fitting Equation 2.13 to measured concentration profiles.

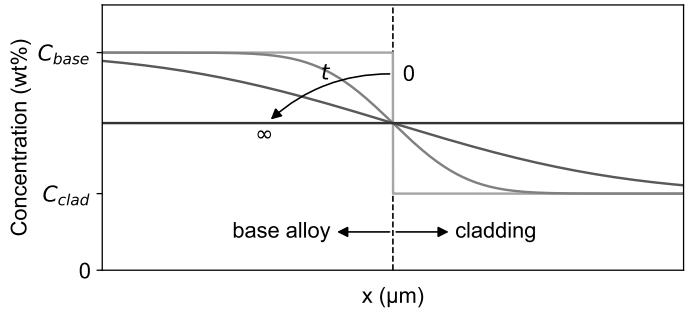

Figure 2.2: Plot of concentration versus position showing the behavior of Equation 2.13 for increasing thermal aging time. The profile is square for $t = 0$ and approaches the gray, horizontal line for $t = \infty$.

The use of Equation 2.13 relies on the assumption that both layers of materials can be approximated as semi-infinite in thickness, meaning that there is negligible change in the concentration of the diffusing element at the outer surfaces of the layers. The following equation is the condition for semi-infinite thickness, where l is the minimum layer thickness [31, p. 129]:

$$l > 10\sqrt{Dt} \tag{2.14}$$

The temperature dependence of diffusion coefficients is described by an Arrhenius relation:

$$D = D_o \exp\left(-\frac{E_a}{RT}\right) \tag{2.15}$$

where D_0 is denoted as the pre-exponential factor, E_a is the activation energy of diffusion, R is the gas constant, and T is temperature.

Classification of diffusion kinetics

In polycrystals, diffusion through lattices and along grain boundaries occurs simultaneously. Grain boundary diffusion and lattice diffusion are described by the diffusion coefficients D_{gb} and D_l, respectively. Due to the lower atomic packing density at grain boundaries, these act as accelerated paths for diffusion (i.e. $D_{gb} \gg D_l$). For this reason, grain boundary engineering (GBE) could serve to reduce diffusion rates and increase the durability of composites in MSRs, especially for cladding techniques, such as electroplating, that produce claddings with small grains.

According to Harrison's classification of diffusion kinetics, there are three kinetic regimes for diffusion: (1) type A kinetics, where lattice diffusion dominates; (2) type B kinetics, where both lattice and grain boundary diffusion play important roles; and (3) type C kinetics, where grain boundary diffusion dominates. The difference between these three regimes is illustrated in Figure 2.3 (the variables in this figure are defined later).

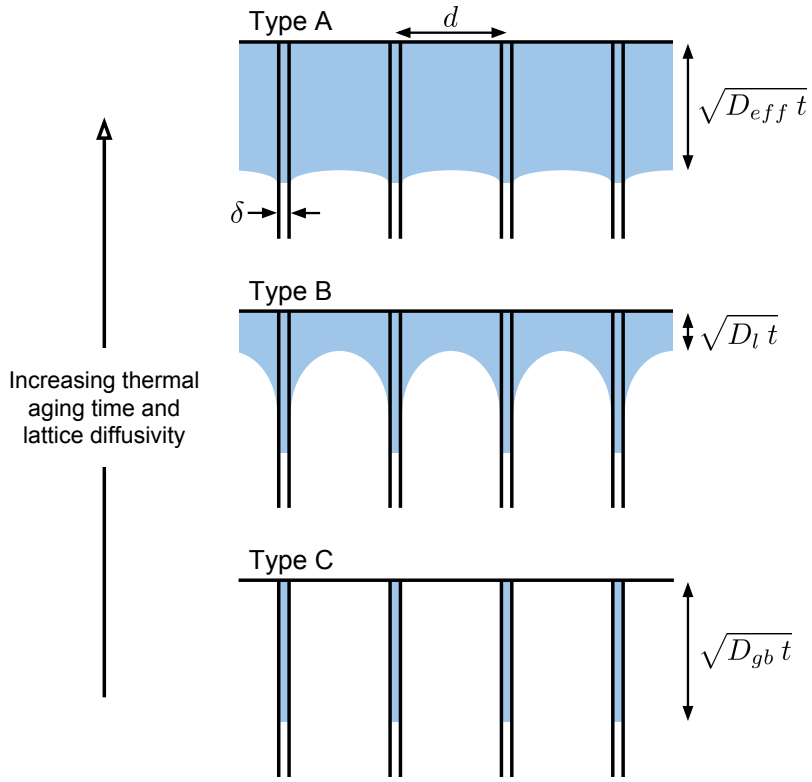

Figure 2.3: Schematic illustration of type A, B, and C diffusion kinetic regimes in Harrison's classification. The grains are parallel and the blue area represents a diffusing element. (Based on [27, Fig. 8.7].)

In **type A kinetics**, lattice diffusion distances are greater than grain sizes, and lattice diffusion fields of neighboring grain boundaries fully overlap. The condition for the type A regime [27] is

$$\sqrt{D_l\,t} \gg d \tag{2.16}$$

where d is average grain size. Often, the limit for type A kinetics is more precisely taken as $\sqrt{D_l\,t}\cdot d^{-1} > 0.4$ [27, 32].

The diffusion coefficient that includes the effect of both lattice and grain boundary diffusion is termed the effective diffusion coefficient D_{eff} [27]:

$$D_{eff} = fD_{gb} + (1-f)D_l \tag{2.17}$$

f is the volume fraction of grain boundaries, itself defined as:

$$f = \frac{q\,\delta}{d} \tag{2.18}$$

where δ is grain boundary width (normally assumed to be 0.5 nm), and q is a numerical factor that depends on grain shape ($q = 1$ for parallel grains and $q = 3$ for square grains). When D in Equation 2.13 is obtained from measured concentration profiles of type A diffusion, it is effectively D_{eff} because the observed diffusion is a result of both grain boundary diffusion and lattice diffusion (and the contribution of dislocations and other imperfections).

The temperature dependence of D_{gb} and D_l are modeled by two separate Arrhenius relations of Equation 2.15 with the same pre-exponential factor but different activation energies, E_a^{gb} and E_a^l. The ratio of E_a^{gb} over E_a^l is 0.4 to 0.6 for most metals [27]. The effect of grain boundary diffusion on overall diffusion is illustrated in Figure 2.4. In general, grain boundary diffusion becomes important below 75–80% of melting temperatures in degrees Kelvin [33, p. 106]. For example, Olson et al. [34] observed the effect of grain size on diffusion of chromium in Ni-plated Incoloy 800H to be significant below approximately 1100 °C.

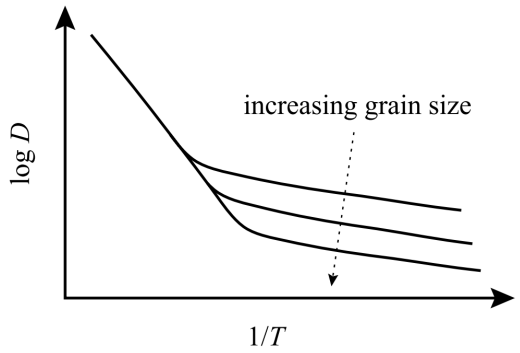

Figure 2.4: The effect of grain size on effective diffusion coefficients as a function of temperature. Below a certain temperature, grain boundary diffusion becomes significant. [35]

In **type B kinetics**, grain boundaries are isolated in that the lattice diffusion fields of neighboring grain boundaries do not overlap. The condition for the type B regime [27]:

$$\delta \ll \sqrt{D_l t} \ll d \tag{2.19}$$

Diffusion kinetics tend toward the type B regime as temperature and exposure time decrease, and as grain size increases. Due to the complicated nature of type B kinetics, D_l must first be known (measured from concentration profiles of type A diffusion) before the product δD_{gb} can be determined from measured concentration profiles. Type B diffusion concentration profiles cannot be fit to Equation 2.13; the equations in [27, pp. 341–342] must be used instead. The measurement of type B (and type C) concentration profiles requires methods of measuring grain boundary diffusion; the radiotracer serial sectioning method is commonly used [27]. These measurements are difficult because of the low concentrations of diffusing species in grain boundaries. Despite these challenges, the type B regime comprises the widest and the most convenient temperature range for diffusion measurements [27].

In **type C kinetics**, diffusion takes place predominantly along grain boundaries. The condition for the type C regime [27]:

$$\sqrt{D_l t} \ll \delta \tag{2.20}$$

Diffusion kinetics tend toward the type C regime as temperature and exposure time decrease. For MSRs, type C kinetics are unlikely to be relevant for the diffusion of alloying elements from structural alloys into claddings but can be relevant for diffusion of fission products, such as tellurium, into alloys.

Multiphase diffusion

The presence of multiple phases in an alloy is problematic for concentration profile measurements because diffusion is activity gradient driven (although it is typically modeled as concentration gradient driven), and the varying activity of diffusing elements in different phases can produce discontinuous concentration changes that do not match models such as Equation 2.12. Unfortunately, complete solutions for concentration profiles in multi-phase diffusion are complex [33, p. 109]. Figure 2.5 is an example of multiphase diffusion for an Al–Ni diffusion couple, where two intermetallic phases have formed in the diffusion zone. Interestingly, a plot of activity versus position would give a relatively smooth curve.

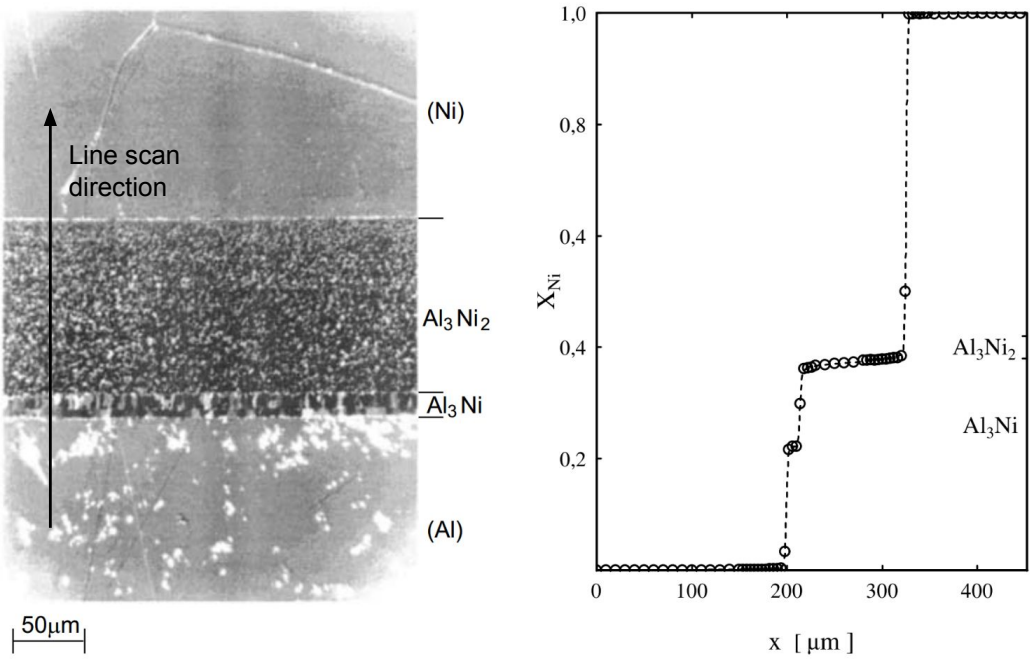

Figure 2.5: Optical micrograph (left) and composition profile (right) of an Al–Ni diffusion couple after a diffusion anneal (modified from source). Note the lack of resemblance between this profile and the complementary error functions in Figure 2.2. [27, p. 55]

Diffusion-induced phase transformation

Along with thermodynamic driving forces, kinetic mechanisms, such as diffusion, can induce phase transformations [36, p. 420]. Diffusion-induced phase transformation, as it's called,

should be taken into consideration when evaluating the possibility of phase transformations in interfacial diffusion zones.

2.2.3 Simulating diffusion and corrosion

As long as the semi-infinite thickness condition is satisfied (i.e. no significant amounts of diffusing atoms reach the surface of claddings) and as long as the assumption of concentration-independence of diffusion coefficients is sufficiently accurate, the diffusion model of Equation 2.13 can be used to predict lifetime diffusion. However, there is a performance advantage to minimizing the thickness of claddings on heat exchanger tubes, and when cladding thickness is minimized, it's likely that the semi-infinite thickness condition will not hold and that significant amounts of diffusing atoms will reach the surface of claddings. In such a case, the correct boundary condition at salt–cladding interfaces is zero flux for the elements that are not leached into salt and a certain flux for the elements that are leached into salt. There is no mathematical diffusion model that can include this boundary condition. Therefore, predicting diffusion in systems with a non-semi-infinite boundary condition probably requires numerical methods (computational simulations). Numerical methods also have the advantage of being able to take into account the concentration-dependence of diffusion.

2.2.4 The effect of carbon content on diffusion and corrosion

Alloys with high carbon content and carbide-forming elements, such as chromium, tend to form carbide precipitates when exposed to the temperatures found in molten salt reactors. In addition to affecting mechanical properties, these precipitates also affect diffusion and corrosion rates. As illustrated in Figure 2.6, the precipitation of carbides at grain boundaries creates an adjacent zone that is depleted of the carbide-forming element. In aqueous environments, intergranular chromium carbide precipitation leads to grain boundary attack due to galvanic action between anodic depleted zones and cathodic carbide precipitates. In

molten fluoride salts, presence of intergranular chromium carbides can cause accelerated corrosion due to direct attack of these chromium carbides [16]. Contrary to what occurs in aqueous solutions, the chromium-depleted metal around the carbides is not attacked because decreasing the chromium content in iron- and nickel-based metals increases their resistance to corrosion in molten fluoride salts [16]. Unlike chromium carbides, molybdenum carbides are corrosion resistant [37], so alloys that form molybdenum carbides (such as Hastelloy N) are less vulnerable to grain boundary attack.

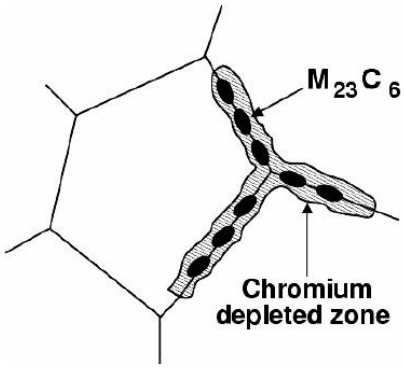

Figure 2.6: Schematic illustration of chromium carbide precipitation and localized chromium depletion around grain boundaries. [38]

Intergranular chromium carbide precipitates have been shown to inhibit chromium diffusion along grain boundaries [37, 39, 40]. As discussed in Section 2.2.2 the dominating diffusion pathway transitions from along grain boundaries to within bulk metal for increasing duration of thermal exposure. Accordingly, the effect of grain boundary carbide formation on diffusion rates should decrease with increasing temperature and duration of exposure, or in other words, as diffusion kinetics tend towards the type A kinetic regime.

Given that corrosion in molten fluoride salts is often diffusion-limited [41], one would expect the diffusion-slowing effect of intergranular chromium carbides to also slow fluoride salt corrosion. However, it's possible for intergranular chromium carbides to accelerate fluoride salt corrosion in the event that their being directly attacked by fluoride salt causes formation of intergranular void networks that are interconnected and allow salt to penetrate the

metal. Whether these void networks are interconnected may depend on the alloy; for instance, Olson [16, p. 132] performed corrosion tests with FLiNaK and observed intergranular voids that were interconnected in Inconel 617 and Haynes 230, but disconnected in Incoloy 800H and Hastelloy X. Molybdenum carbides probably slow diffusion as well, but in contrast with chromium carbides, molybdenum carbides also resist corrosion.

Even if a cladding has low carbon content (e.g. electroplated nickel), its carbon content can increase with time due to carbon diffusion from structural alloys and due to carbon deposition from salt that is in contact with graphite[6]. In nickel and γ-iron, diffusion coefficients of carbon at 700 °C are on the order of 10^{-13} m^2 s^{-1}, several orders of magnitude greater than diffusion coefficients of chromium, for example. This is due to differing diffusion mechanisms: carbon diffuses by a direct interstitial mechanism, whereas metal lattice elements (e.g. chromium) diffuse by a vacancy mechanism [27]. The rapid diffusion of carbon makes carbide formation possible in claddings that initially have low carbon content, but this of course also depends on the presence of carbide-forming elements, such as chromium.

2.2.5 Microstructural stability in diffusion zones

It's important for the interface between claddings and structural alloys to remain free of brittle material phases throughout the operating lifetime of reactors. The microstructural evolution of candidate structural alloys and cladding materials is well understood, but there is much less knowledge about the microstructural evolution of the mixed zone at the interface of these materials. As a result, it's necessary for candidate cladding and structural alloy combinations to be tested for microstructural stability at their interface. These tests must be performed for the range of temperatures that the composites will be exposed to (e.g. 550–700 °C). In diffusion studies, one can focus on the highest temperatures that the composites

[6] Although graphite is chemically inert in molten salt, it may be dissolved in the form of colloids or it may be partially soluble as carbon fluoride [42].

will be exposed to (e.g. 700 °C) because diffusion rates increase with temperature, so design decisions based on diffusion at these highest temperatures are conservative.

2.2.6 Tellurium-induced embrittlement

A challenge with fuel-bearing salts is intergranular cracking caused by the fission product tellurium[7]. This effect was observed for Hastelloy N in the MSRE and—along with irradiation embrittlement—was one of the technical reasons for the cancellation of the MSR program in the 1970s [43]. The penetration of tellurium into Hastelloy N in the MSRE was limited and did not cause any problems, but it is not well-understood if it could become problematic for longer reactor lifetimes and different conditions. Tellurium-induced embrittlement can be greatly reduced by making salt sufficiently reducing (see Figure 2.7), and fortunately, doing so also makes salt less corrosive. However, there are limits to the extent to which salt can be made reducing, as discussed in Section 1.2. Resistance to tellurium-induced embrittlement is an important factor in the selection of cladding materials, as it can be the determining factor for durability of metals exposed to fuel salt, especially at higher temperatures [13]. Information about resistance to tellurium-induced embrittlement is available for a very limited number of alloys—mainly Hastelloy N and its variants.

2.2.7 Irradiation effects

Radiation has a number of effects on metals; among these are hardening, embrittlement, segregation, phase precipitation, swelling, accelerated diffusion, and accelerated creep. The prevalence of these effects depends strongly on temperature and irradiation conditions. This section discusses the effects of irradiation on microstructure and mechanical properties. The effect of irradiation on corrosion in molten fluoride salts is discussed in Section 2.1.

[7] Tellurium-induced embrittlement could be included as a corrosion mechanism in Section 2.1.

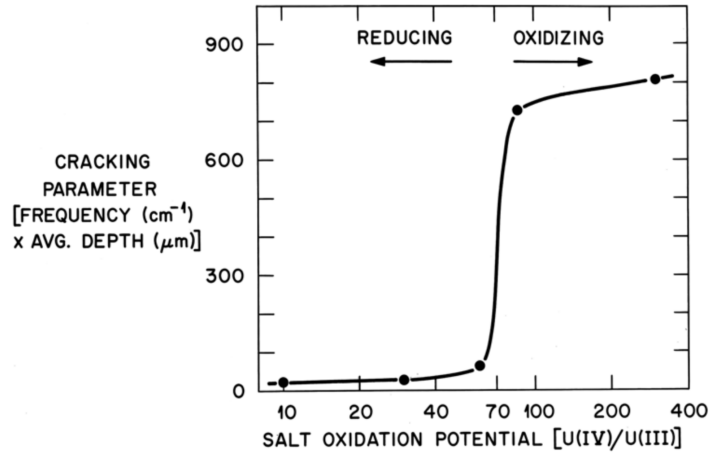

Figure 2.7: Effect of redox potential on tellurium-induced cracking in Hastelloy N. [44]

In nickel-bearing alloys, point defect generation is caused primarily by two mechanisms [45]:

1. Direct displacement by neutrons.
2. Charged particle-emitting reactions such as (n,α) or (n,p) from the following two-stage processes involving transmutation, where both the emitted particles and the recoiling nuclei may cause displacements.

$$^{58}\text{Ni} + \text{n} \longrightarrow {}^{59}\text{Ni} + \text{n} \longrightarrow {}^{56}\text{Fe} + {}^{4}\text{He} \tag{2.21}$$

$$^{58}\text{Ni} + \text{n} \longrightarrow {}^{59}\text{Ni} + \text{n} \longrightarrow {}^{59}\text{Co} + \text{H} \tag{2.22}$$

$$^{58}\text{Ni} + \text{n} \longrightarrow {}^{59}\text{Ni} + \text{n} \longrightarrow {}^{60}\text{Ni} + \gamma \tag{2.23}$$

Hydrogen production from Equation 2.22 dominates for fast spectrums, and helium production from Equation 2.21 dominates for thermal spectrums. Helium can also originate from neutron capture of boron impurities followed by alpha decay, although this source burns out quickly compared to nickel because of its large (thermal) cross section and small concentration in alloys [35]:

$$^{10}\text{B} + \text{n} \longrightarrow {}^{7}\text{Li} + {}^{4}\text{He} \tag{2.24}$$

At 30–60% of melting temperatures (in degrees Kelvin)—which, for candidate structural and cladding alloys, overlaps with fuel salt temperature ranges of most MSR designs—void swelling, embrittlement, and irradiation creep are common material degradation mechanisms [45].

Similarly to differences in thermal expansion, differences in the amount of void swelling between structural and cladding layers in a composite can create significant interfacial stress. Void swelling is highly dependent on temperature and irradiation dose (measured in displacements per atom (dpa) in the irradiated metal).

Radiation-induced segregation causes enrichment or depletion of alloying elements in regions near surfaces, dislocations, voids, grain boundaries, and phase boundaries. It typically occurs at 30–50% of alloy melting temperatures [46]. Radiation-induced enrichment or depletion of a solute can cause or modify the precipitation (or dissolution) of phases. Thus, exposing alloys to irradiation can lead to the formation of precipitates that would not be present otherwise (termed irradiation-induced phase formation).

Irradiation can decrease the creep performance, tensile strength, and ductility of materials. The significance of irradiation-induced evolution of mechanical properties depends on temperature and irradiation dose. Irradiation embrittlement is of particular concern for claddings in MSRs given the need for claddings to remain intact and avoid cracking in order to prevent corrosion of the underlying structural alloy.

Irradiation can accelerate diffusion where macroscopic concentration profiles exist [35]. Therefore, irradiation can reduce the durability of composites in MSRs, and this implies a possible limitation of experimental diffusion and corrosion studies that don't include irradiation. Figure 2.8 compares thermal and radiation diffusion coefficients in a nickel-based alloy in function of temperature and shows that, for this material and displacement rate, radiation-enhanced diffusion is dominant below 700 °C. Similar data for the materials and displacement rates of interest should be obtained from the literature or experimentally. If

such data also shows that irradiation only has an effect below 700 °C, for example, it may be possible to ignore the effect of irradiation on diffusion when designing for a maximum temperature of 700 °C (or higher). This is because the thickness of layers in composites will be selected for the conditions where diffusion is fastest; for the aforementioned example, this corresponds to 700 °C, and above this temperature, irradiation does not enhance diffusion.

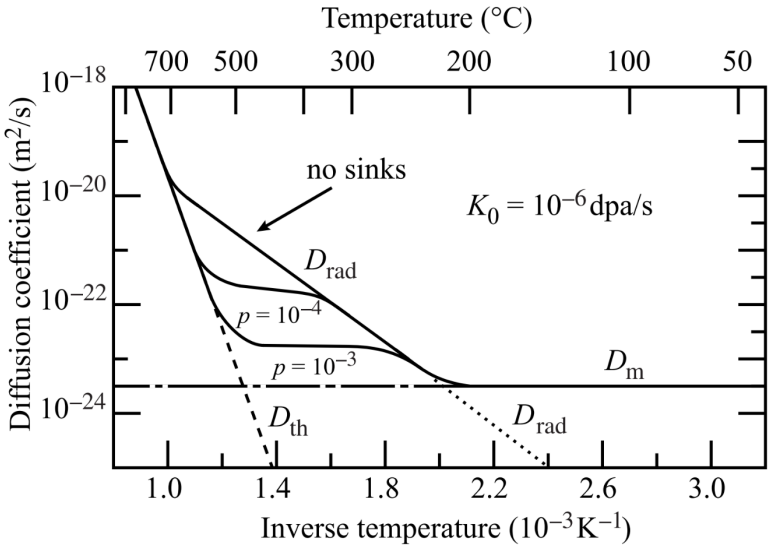

Figure 2.8: Diffusion coefficients as a function of inverse temperature in a nickel-based alloy during irradiation at a displacement rate of 10^{-6} dpa/s. D_{rad} is the radiation diffusion coefficient, D_{th} is the thermal diffusion coefficient (i.e. without irradiation), and D_m is the diffusion coefficient from displacement mixing. D_{rad} is calculated from rate theory for various sink annihilation probabilities (p). [35, p. 207]

2.3 Literature review of claddings for corrosion protection in molten fluoride salts

There are numerous cladding techniques available for the application of corrosion protection in molten fluoride salts. A distinguishing factor among cladding techniques is their capability to be used to clad surfaces which aren't directly accessible. Some cladding techniques require direct line-of-sight (unobstructed) access to the substrate. For example, the inside of small

diameter heat exchanger tubes require non-line-of-site cladding techniques, whereas reactor vessel walls can be clad with line-of-sight techniques. Non-line-of-sight cladding techniques include electroplating, electroless plating, chemical vapor deposition (CVD), and coextrusion. Line-of-sight cladding techniques include physical vapor deposition (PVD), laser cladding, thermal spray, cold spray, and weld overlay. Research into these cladding techniques requires consideration of the geometry of the components that will be clad, and some of the techniques are better suited for coating industrial-scale components than others. A report from ORNL by Muralidharan et al. [47] summarizes the advantages and disadvantages of several techniques for cladding nickel on nickel-based alloys, although their work is non-exhaustive and more can be done for assessing cladding techniques for molten fluoride salt applications.

The main considerations for selecting a cladding material are corrosion resistance, substrate compatibility (diffusion resistance, bond adhesion, ductility, and matching thermal expansion), repairability, wear resistance, irradiation resistance, and cost. Nickel is a promising cladding material due to the instability of nickel fluoride in molten salt (less negative Gibbs free energy of formation). Molybdenum is another candidate cladding material due to its corrosion resistance in molten fluoride salts, and it has the added benefit of being more resistant to chromium and iron diffusion than nickel. However, unlike nickel, molybdenum has significantly different thermal expansion characteristics than candidate structural alloys, which diminishes its viability as a cladding material. Olson [16] investigated plasma-sprayed molybdenum on Incoloy 800H and found that it delaminated in molten FLiNaK salt, although thermal testing demonstrated compatibility with the Incoloy 800H substrate. Several causes were suggested for the delamination, but more work is required for identifying the cause of the failure in order to continue investigating plasma-sprayed molybdenum as a corrosion barrier. At ORNL, Hastelloy N was investigated as a cladding material for heat exchanger tubes by coextruding it with stainless steel 316 [48]. High-temperature mechanical tests confirmed that stainless steel 316/Hastelloy N composite has adequate mechanical properties, and it

was concluded that no major difficulties should be expected in the fabrication of a stainless steel 316/Hastelloy N heat exchanger. A different class of cladding materials is carbides. Brupbacher et al. [49] investigated binder-free Cr_3C_2 coatings on H230 (Ni-Cr-W) alloy produced by carburization of plasma sprayed and cold sprayed chromium coatings. High porosity levels lead to the conclusion that this material may not be suitable for preventing corrosion from molten fluoride salts.

Olson et al. [16, 34] investigated nickel plating (sulfamate process) on Incoloy 800H for corrosion protection in molten fluoride salts. They performed static salt corrosion tests of Ni-plated 800H, bare 800H, and Ni 201 (99% pure nickel) at 850 °C for 500 h in FLiNaK salt with a graphite crucible. The nickel plating drastically reduced the amount of corrosion as measured from sample weight loss and chromium concentration increase in the salt. Figure 2.9 illustrates the surface of these materials after the corrosion tests; the bare 800H underwent significant surface pitting whereas the Ni-plated 800H and Ni 201 were relatively undamaged. However, it's important to note that this corrosion test was short relative to a reactor lifetime of several years. Because it takes time for chromium to diffuse from a structural alloy substrate through nickel and into salt, the aforementioned results don't inform of the long-term durability of nickel claddings.

Olson et al. [34] determined effective diffusion coefficients of chromium in Ni-plated 800H and a Ni-plated Fe–Ni–Cr model alloy at various temperatures (600–1200 °C). The Fe–Ni–Cr model ternary alloy allowed the investigation of chromium diffusion without the interference of trace constituents and secondary phases. Effective penetration depths calculated with the chromium diffusion coefficients compared favorably with the diffusion observed from molten salt corrosion tests. However, error may have been introduced by assuming that the diffusion coefficients are concentration-independent and that the diffusion kinetic regime is type A [16, 34]. From these tests, it was concluded that the diffusion

resistance of nickel claddings may be insufficient depending on temperature, thickness, and microstructure [34].

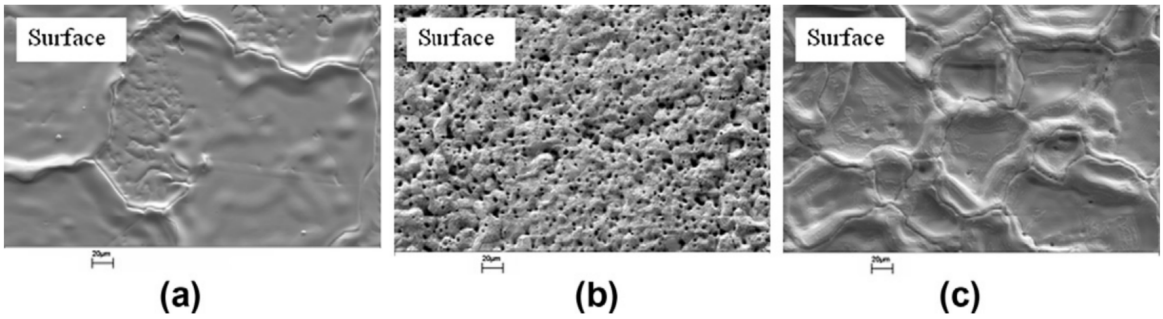

Figure 2.9: SEM images of the surface of (a) Ni 201 (>99% nickel), (b) 800H, and (c) Ni-plated 800H after a corrosion test in FLiNaK salt at 850 °C for 500 h. [34]

Since grain boundaries act as accelerated pathways for diffusion and electroplated nickel typically has nanometer-sized grains, it may be possible to slow diffusion in electroplated nickel by increasing its grain size (decreasing grain boundary surface area). Motivated by this possibility, Olson [16] experimented with thermomechanical processing methods to promote secondary recrystallization and large grain growth in electroplated nickel. Unfortunately, for the thermomechanical processing parameters that were tested, increasing the grain size of nickel plating had minimal effect on diffusion rates.

According to McNabb and McCoy [50, Sec. 13.9], "duplex tubing has been proposed for steam generator service with Incoloy 800 on the inside (steam side) and nickel 280 (pure nickel with 0.05% AI_2O_3 for grain size control) on the outside or salt side". The addition of AI_2O_3 for grain size control contrasts with the aforementioned desirability of maximized grain size for slowing diffusion. McNabb and McCoy [50, Sec. 13.9] mechanically tested co-extruded Incoloy 800/nickel 280 with positive results, but they also found that the nickel 280 is not compatible with steam, and this is a significant drawback due to the possibility of a leak. They did not report having done any fluoride salt corrosion tests of the coextruded Incoloy 800/nickel 280.

The introduction of an oxide layer between structural alloys and claddings has been proposed as a means of improving their durability by slowing diffusion. Experiments have shown that chromium and iron diffusion is four orders of magnitude slower in Cr_2O_3 than in nickel [51]. However, the desirability of interfacial oxide layers is questionable because these probably increase the likelihood of cladding delamination.

Xu et al. [52] developed a method for fabricating a Cr_2O_3 layer between stainless steel 310 and nickel cladding by cold spraying a 20–50 µm thick inner layer of Ni(O) and a 150–200 µm thick outer layer of oxygen-free nickel followed by annealing at 900 °C to form a 2 µm thick interfacial layer of Cr_2O_3. The cold spraying process allows oxygen in the Ni(O) to be retained. During annealing, chromium preferentially reacts with oxygen from the Ni(O) to form Cr_2O_3. The diffusion-suppressing effect of the Cr_2O_3 layer during heat treatment at 750 °C for 100 h is shown in Figure 2.10. The advantage of this fabrication technique compared to processes of applying claddings without destroying initially present surface oxides (e.g. electroplating without first chemically stripping surface oxides) is that it may result in better adhesion between the ceramic diffusion barrier and sandwiching metals.

Xu et al. [53] also tested an Al_2O_3 diffusion barrier by combining three cold sprayed layers of NiCoCrAlY, Ni(O), and oxygen-free nickel on a stainless steel 304 substrate followed by annealing at 900 °C. Since stainless steel 304 does not contain aluminum, the NiCoCrAlY layer is used to supply aluminum which preferentially reacts with oxygen from the Ni(O) layer. In heat treatment tests, the NiCoCrAlY/Al_2O_3/nickel cladding exhibited similar diffusion blocking to the Cr_2O_3/nickel cladding mentioned above. NiCoCrAlY is commonly used for bonding ceramics to superalloys, and according to Xu et al. [53], it facilitates the coating deposition procedure of Ni(O) and Ni.

Muralidharan et al. [47] investigated nickel claddings fabricated by CVD (nickel carbonyl process) and laser cladding on Inconel 617 and Incoloy 800H base alloys for molten fluoride salt corrosion protection. Significantly more mixing of alloying elements was observed for

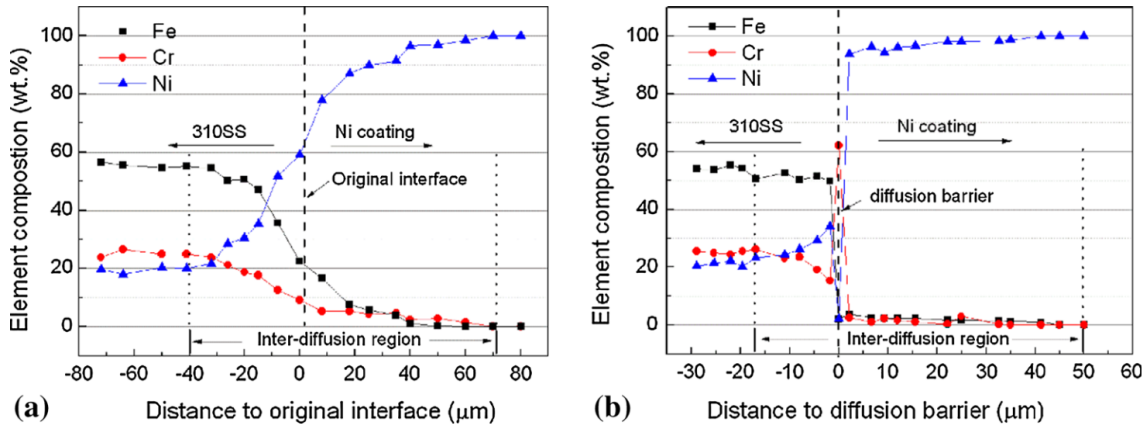

Figure 2.10: Diffusion profiles of alloying elements from stainless steel 310 into nickel after a heat treatment at 750 °C for 100 h (a) without and (b) with an interfacial Cr_2O_3 layer. [52]

the laser cladding process than the CVD process, and the Cr_2O_3 surface layer on the base alloys remained intact during CVD but not during laser cladding. The CVD cladding had no pinholes or cracks, whereas the laser cladding had a few voids, pinholes, and cracks. Similarly, Shi et al. [4] weld-overlayed nickel on stainless steel 304H and characterized its microstructure. Neither Muralidharan et al. [47] nor Shi et al. [4] reported having done thermal aging or corrosion tests for assessing the durability of these claddings.

Wilson [54] investigated CVD nickel cladding on Alloy 214 for the application of fission chambers exposed to fluoride salts. The nickel cladding was delaminated at several areas, and after annealing at 850 °C for 1000 h, it contained significant porosity. The results in [47, 54] suggest that a process that removes surface oxides from substrates prior to CVD cladding and ensures consistent metallurgical bonding would have to be developed before CVD cladding could be used on reactor components.

Coextrusion is a promising cladding technique, although the process development is resource-intensive. A detailed study was undertaken by Short [55] on coextruded tubes of Fe–12Cr–2Si-clad F91 alloy for corrosion protection in Pb–Bi eutectic coolant (for use in Pb–Bi eutectic cooled nuclear reactors). While the requirements for this coolant are different than those for molten fluoride salts, a similar research process could lead to the development

of coextruded tubes for use in MSRs. Moreover, there is little information available in the literature about welding clad high-temperature alloys, but the work by Short [55] is an example of what would be required, which includes a preliminary demonstration of weldability followed by commercial weldability certification in accordance with ASME standards.

MAX phase materials are a recently developed class of material that may be suitable as a corrosion barrier in molten salts. MAX phase materials have the strength and thermal conductivity of metals and the chemical resistance of ceramics—an ideal combination of properties for corrosion barriers in heat transfer applications. Rodriguez et al. [56] tested MAX phase materials as a corrosion barrier on Haynes 230 in molten $MgCl_2$–KCl salt at 850 °C. The coatings were either cold sprayed Ti_2AlC or physical vapor deposited (PVD) and annealed Ti_2AlC or Zr_2AlC. The quantitative extent of corrosion resistance is not clear from the results presented in [56]. In general, 117 µm of cold sprayed Ti_2AlC and 3.6 µm of PVD Zr_2AlC were more protective than 3.9 µm of PVD Ti_2AlC. The degradation of cold sprayed Ti_2AlC from exposure to molten $MgCl_2$–KCl salt is shown in Figure 2.11. It should be noted, however, that chloride salts have different corrosion behavior than fluoride salts. Rodriguez et al. [56] made no mention of the applicability of MAX phase coatings to corrosion protection in fluoride salts, but given the corrosion susceptibility of zirconium, aluminum, and titanium in fluoride salts, the coatings that Rodriguez et al. [56] tested might not be viable for fluoride salt applications (depending on Gibbs free energies). Granted, there are several other known MAX phases [57], and some of these, such as Mo_2GaC, might be corrosion resistant in fluoride salts.

Alternatively to the cladding techniques described above, corrosion barriers could be formed in-situ during exposure to molten salt. Cheng et al. [58] performed a corrosion test on stainless steel SS316L and Hastelloy N at 850 °C for 1000 h in static molten FLiNaK salt with zirconium additions to the salt, which caused the formation of zirconium coatings on

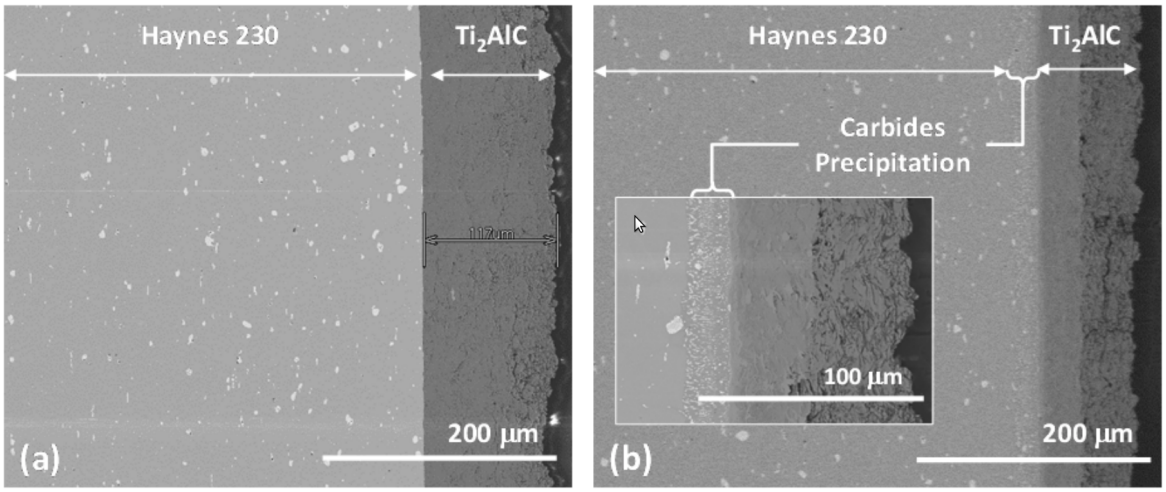

Figure 2.11: Cross-sectional SEM images of Haynes-230 cold sprayed with 117 µm of Ti_2AlC (a) before and (b) after exposure to molten $MgCl_2-KCl$ salt at 850 °C for 100 h. [56]

the SS316L and Hastelloy N samples. These coatings prevented the outward diffusion of iron and chromium in favor of nickel, resulting in a corrosion resistant layer of Zr–Ni alloy on both the SS316L and Hastelloy N samples. A thicker zirconium deposit was observed on Hastelloy N than SS316L due to the larger electromotive potential difference between nickel and zirconium than between iron and zirconium (Hastelloy N is nickel-based whereas SS316L is iron-based). The Ni–Zr alloy is an intermetallic phase which is more brittle than the base alloys, and differences in thermal expansion coefficients could potentially cause cracking of the coatings. While preliminary results are promising for non-fuel-bearing FLiNaK salt, this corrosion control technique is probably not viable for fuel-bearing salts because the Gibbs free energy of formation of ZrF_4 is very close to that of UF_4 (see Table 2.1), and therefore, exposing UF_4-containing salt to metallic zirconium may cause undesirable precipitation of metallic uranium.

Summary of literature review

In this review, the issue of chromium diffusion from structural alloys into claddings is highlighted. While nickel has excellent corrosion resistance, chromium diffusion in electroplated

nickel (and subsequent dissolution of chromium into salt) may be excessive depending on temperature, thickness, and microstructure [34]. Molybdenum is also corrosion-resistant and chromium diffusion rates are slower in molybdenum than in nickel, but molybdenum's thermal expansion characteristics don't match those of candidate structural alloys, and plasma sprayed molybdenum delaminated when exposed to molten fluoride salt [16]. A potential solution to the problem of chromium diffusion is interfacial oxide diffusion barriers (e.g. Cr_2O_3 or Al_2O_3) between claddings and structural alloys. More work could be done to assess the effect of oxide diffusion barriers on the mechanical performance of cladding, as sharp composition gradients may cause adhesion problems. Additional claddings that have been investigated are binder-free Cr_3C_2 produced by carburization of plasma sprayed or cold sprayed chromium coatings [49], Hastelloy N coextruded with stainless steel [48], MAX phase materials produced by CVD or cold spraying [56], and Zr–Ni alloy formed in-situ by adding zirconium to molten salt [58].

Based on this literature review, there is a need for evaluating the mechanical performance of claddings with oxide diffusion barriers, further evaluating the diffusion resistance of various cladding material and structural alloy combinations (without oxide diffusion barriers), and testing claddings in the worst foreseeable conditions of irradiation and corrosion in molten fluoride salts.

2.4 Selection of codified structural alloys

Section III, Division 5, Class B (High Temperature Reactors) of the ASME Boiler and Pressure Vessel Code (BPVC) is the most applicable ASME code for components that form the reactor pressure boundary in high-temperature nuclear reactors, such as the primary heat exchanger in MSRs. There are currently five alloys in this section. Two of them are not suitable for use at the temperatures found in MSRs (2 1/4Cr–1Mo steel, class 1, and a modified 9Cr–1Mo–V steel known as Grade 91 steel), and the other three are stainless

steel 304H, stainless steel 316H, and Incoloy 800H, referred to as SS304H, SS316H, and 800H in this thesis. SS304H and SS316H are less expensive than 800H. The three alloys ranked in increasing order for high-temperature creep strength are SS304H, SS316H, and 800H. There are temperature limitations defined in the ASME BPVC: for primary stress up to 300 000 h, service temperature is limited to 760 °C for 800H and 815 °C for SS304H and SS316H; fatigue curves are provided for temperatures up to 760 °C for 800H and 704 °C for SS304H and SS316H.

In their unclad form, SS316H is often favored over SS304H and 800H because it has better creep strength and creep–rupture strength than SS304H [59, p. 22–143] and better corrosion resistance than 800H. The disadvantage of the inferior corrosion resistance of 800H compared to SS316H is avoided if it is clad with a corrosion resistant material. For the application of heat exchanger tubes, the non-clad side of clad 800H can be exposed to secondary salt if this salt is made highly reducing (beyond what is possible for fuel salt). However, it is feasible to clad heat exchanger tubes on both sides of the structural alloy. Also, one should also consider the possibility of cladding breaches, which would expose structural alloy to fuel salt. This possibility favors SS316H over 800H because of its corrosion resistance.

It should be noted that this discussion of structural alloy selection is specific to heat exchanger tubes. For cladding reactor vessel walls, which involve significantly more material and which are subject to less demanding conditions than heat exchanger tubes, SS304H becomes favorable as a structural alloy because of its lower cost [4].

Depending on the cladding and structural alloy combination, there may be phases (e.g. intermetallics or carbides) formed at their interface that would affect the viability of specific material combinations and that would affect the selection of the structural alloy. However, there are scarcely any data in the literature about the interfacial microstructure stability of the alloy combinations of interest.

For applications with significant radiation dose, the radiation resistance of structural alloys must be taken into account. Radiation swelling characteristics would have to be compared with those of cladding materials. Too large a difference in radiation-induced volume changes can lead to excessive stress a the interface of structural alloys and claddings. The concern of stress from mismatched expansion equally applies to thermal expansion. In Figure 2.14, the thermal expansion of both SS316 and 800H is compared with that of potential cladding materials; 800H is slightly better than SS316 in this respect.

From the considerations discussed above, it was decided that both 800H and SS316H should be investigated as structural alloys for clad heat exchanger tubes. Their nominal composition is presented in Table 2.2.

Table 2.2: Nominal composition (weight %; excluding the trace elements phosphorus and sulfur) of SS316H and 800H from the 2015 ASME BPVC. [60]

Material		Fe	Ni	Cr	Mo	Si	Mn	C	Al	Ti	Cu
SS316H	min.	bal.	10.0	16.0	2.00	-	-	0.04	-	-	-
	max.		14.0	18.0	3.00	0.75	2.0	0.10	-	-	-
800H	min.	39.5	30.0	19.0	-	-	-	0.05	0.15	0.15	-
	max.	-	35.0	23.0	-	1.00	1.50	0.10	0.60	0.60	0.75

2.5 Selection of cladding materials

When selecting cladding materials for MSRs, the two classes of materials to be considered are ceramics and metals. For ceramics, we know that graphite was used as the core material of the MSRE and that it's inert in molten fluoride salts. The question arises: why not use graphite? The challenge with graphite and other ceramics lies in their thermo-mechanical properties and microstructure. Although some ceramic–ceramic composites (e.g. C–C and SiC–SiC composites) have high strength up to extremely high temperatures, their properties are not compatible with metallic substrates. In addition to mismatched thermal expansion

coefficients, lattice parameters, bond types (metallic vs. covalent), and ductility, there are the issues of swelling due to irradiation (an important concern with graphite reactor cores) and the difficulty of joining ceramics to metals compared to joining metals to metals. The focus is therefore on metal claddings.

The first question to ask when selecting metallic cladding materials is whether they will corrode. As discussed in Section 2.1, the constituent elements of such claddings must be thermodynamically resistant to dissolving in molten fluoride salts. And as seen from Table 2.1, nickel and molybdenum are some of the more corrosion resistant elements.

2.5.1 Nickel

Molten fluoride salt corrosion studies have shown that nickel is virtually immune to attack [16]. Nickel claddings can be pure if fabricated with methods such as electroplating or chemical vapor deposition (CVD), or they can be nearly pure if fabricated from Ni 201, a commercially available alloy (>99 wt% nickel; composition in Table 2.3), with methods such as coextrusion or thermal spray. As shown in the literature review in Section 2.3, nickel has been the focus of previous research into claddings for molten salt reactors. The drawback of nickel is that its chromium diffusion resistance may be insufficient depending on temperature, operating time, cladding thickness, and microstructure.

Molybdenum is also corrosion resistant, and chromium diffusion rates are slower in molybdenum than in nickel, but molybdenum is brittle and its thermal expansion doesn't match that of candidate structural alloys (see Figure 2.14). The facts accumulate to suggest that the ideal cladding material is an alloy of nickel and molybdenum.

Table 2.3: Nominal composition (weight %) of Ni 201. [61]

Material		Ni	Fe	Si	Mn	C	Cu
Ni 201	min.	99.0	-	-	-	-	-
	max.	-	0.40	0.35	0.35	0.02	0.25

2.5.2 Electroplated Ni–Mo alloy

In Ni–Mo alloys, molybdenum imparts strength and diffusion resistance, but its concentration should be less than around 20 wt% to avoid formation of embrittling intermetallic phases and large molybdenum carbide particles [7]. For example, Hastelloy B3 is a commercially available Ni–Mo alloy with a molybdenum content of 28.5 wt% and a chromium content of 1.5 wt%, giving it excellent corrosion resistance in molten fluoride salts [62], but it is ruled out of consideration as a cladding material because of its tendency to embrittle in the temperature range of 500 °C to 900 °C. This embrittlement results from the precipitation of intermetallic Ni–Mo phases (the most deleterious being Ni_4Mo [63]) that would occur early on in a reactor lifetime of several years.

With Ni–Mo phase diagrams like the one in Figure 2.12, relative concentrations of nickel and molybdenum can be selected so as to avoid precipitation of intermetallics. For the denatured molten salt reactor (DMSR) design from ORNL, the primary heat exchanger inlet and outlet temperatures are approximately 550 °C and 700 °C [64]. For this temperature range, we can see from Figure 2.12 that intermetallics shouldn't precipitate in a Ni–Mo alloy with less than 7 at% (i.e. 11 wt%) molybdenum. This statement involves some uncertainty due to the possibility of irradiation-induced phase precipitation (discussed in Section 2.2.7). And although not done by the present author, the possibility of precipitation of intermetallics during reactor temperature ramp up and ramp down should be evaluated from the kinetics of phase transformations at lower temperatures.

There are no commercially available Ni–Mo alloys with 11 wt% molybdenum, but fortunately, such an alloy can be electroplated. (Interestingly, molybdenum cannot be electroplated by itself.) The literature on the mechanical properties of electroplated Ni–Mo is scarce, although it's known to have high hardness due to internal stress and a nanocrystalline structure [66, 67]. Nee et al. [68] investigated the effect of annealing Ni–Mo plating at 300 °C for 1 h and found that both yield strength and elongation increased, with elongation

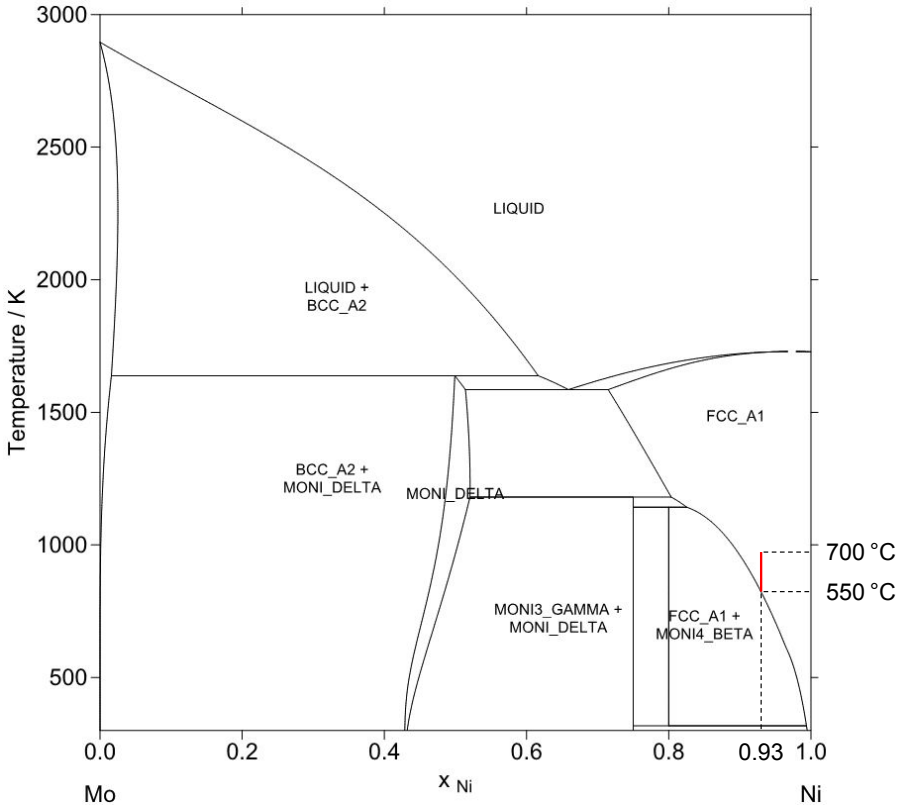

Figure 2.12: Calculated Ni–Mo phase diagram, modified from source with a red line at 7 at% molybdenum from 550 °C to 700 °C. [65]

increasing from 2 to 5 wt%. There was very little recrystallization, so the strength increase was probably due to recovery leading to relief of internal stresses. The increase in elongation to 5 wt% is probably an insufficient improvement in ductility (age-embrittled Hastelloy B3 elongates more). Mousavi et al. [69] heat treated Ni–Mo (76–34 wt%) plating for 25 min at 200, 400, and 600 °C; an inverse Hall–Petch relationship (i.e. hardness is increasing function of grain size) was observed for grain sizes from 5 to 24 nm. Similarly, DeLima-Neto et al. [70] observed a positive correlation between hardness and heat treatment temperature for Ni–Mo (87–13 wt%) plating and 1 h heat treatments. The inverse Hall–Petch relationship applies mainly to nano-sized grains; past a certain grain size, hardness will decrease as grain size is increased. The question remains whether higher temperature and/or longer duration heat treatment for grain growth could sufficiently increase the ductility of Ni–Mo plating.

One should also consider the possibility of underlying structural alloys being adversely affected by heat treatments that are optimized for Ni–Mo plating.

For Ni–Mo plating, no information could be found about its fluoride salt corrosion resistance (although it should be excellent), irradiation resistance, or tellurium embrittlement resistance. Additionally, several plating shops were contacted and none had experience with electroplating Ni–Mo, so the process most likely lacks commercial availability. Ni–Mo plating would require considerable research and development before implementation in an MSR, but it has potential to be a highly corrosion and diffusion resistant cladding material.

2.5.3 Haynes 242 (Ni–Mo–Cr alloy)

While the presence of chromium in alloys generally worsens their corrosion resistance in fluoride salts, it can have beneficial effects on the microstructure and mechanical properties of Ni–Mo alloys. Haynes 242 is a Ni–Mo–Cr alloy with high molybdenum content (25 wt%) and high-temperature strength because of the microstructure that results from its 8 wt% chromium content (its full composition is shown in Table 2.4). It has tensile and creep strength up to 705 °C which are as much as double those for solid solution strengthened alloys, but with retained ductility after long-term exposure to high temperatures. These properties are due to the formation of long-range ordered microdomains of $Ni_2(Mo,Cr)$ which are stable and less brittle than other phases such as Ni_4Mo (which forms in Hastelloy B3). As seen in Figure 2.13, Haynes 242 is far more ductile after exposure to 650 °C for 4000 h (∼167 days) than Hastelloy B.

Table 2.4: Nominal composition (weight %) of Haynes 242. [63]

Material		Ni	Cr	Mo	Fe	Si	Mn	C	Co	Al
Haynes 242	min.	65*	7.0	24.0	-	-	-	-	-	-
	max.		9.0	26.0	2.0	0.80	0.80	0.03	2.5	0.5

* Balance

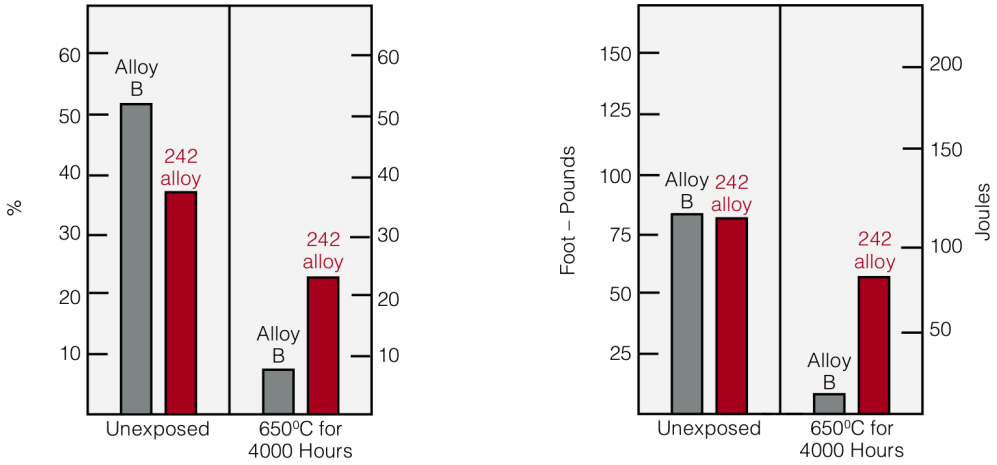

Figure 2.13: Comparison of ductility and impact strength between Hastelloy B ("Alloy B") and Haynes 242 ("242 alloy"): room-temperature tensile elongation (left) and impact strength (right). (modified from source) [63]

Theoretical results have shown that Haynes 242 is not as corrosion resistant to fluoride salts as Hastelloy N [71]. From corrosion tests in FLiNaK, Haynes 242 exhibited "good corrosion resistance"[8], although in the same study, Hastelloy B2 was more corrosion resistant [72]. Ouyang et al. [73] performed static corrosion tests with moisture-containing FLiNaK salt (3.19 wt%) at 600 °C for 100 and 300 h, and found that Haynes 242 underwent nearly twice the mass loss compared to Hastelloy N. However, the presence of moisture created additional mass loss mechanisms, such as oxidation of molybdenum, and therefore, these results do not translate to corrosion performance in salts with low moisture contents. In general, there is a lack of data about the corrosion resistance of Haynes 242 in fluoride salts, especially when compared with what is available for Hastelloy N.

A disadvantage of Haynes 242 is its thermal expansion, which is less than that of SS316H and 800H and more so than nickel or Hastelloy N (see Figure 2.14). Therefore, there would be more interfacial stress between Haynes 242 and underlying structural alloys than between nickel or Hastelloy N and underlying structural alloys.

[8]The details of this study are not known due to lack of a translated copy from Chinese.

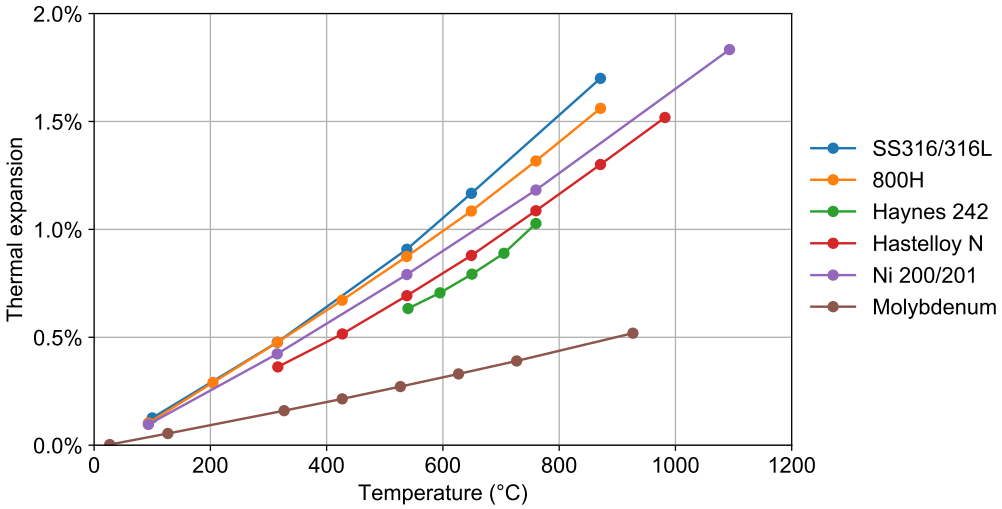

Figure 2.14: Thermal expansion from room to elevated temperature for cladding alloys compared to structural alloys. Incoloy 800H and Ni 200/201 have the closest matching thermal expansion. The limited data that could be found for SS316H matches the data for SS316/316L that is shown here.

2.5.4 Hastelloy N (Ni–Mo–Cr alloy)

Hastelloy N (UNS N10003, with the Chinese-made version known as GH3535) is a Ni–Mo–Cr alloy developed at ORNL during the Aircraft Reactor Experiment explicitly for compatibility molten fluoride salts, and it was extensively used in the MSRE (Figure 2.15). It has excellent fluoride salt corrosion resistance and high-temperature strength, and it has the most data to justify its use as a fuel-salt-exposed material in MSRs. However, it lacks codification: "[Hastelloy N] is currently codified for use in ASME Code Section VIII under Code Case 1315 for use in pressure vessels at up to 704 °C, but it is not explicitly approved for nuclear construction within ASME's Section III" [74].

Hastelloy N is nickel-based with 16 wt% molybdenum and 7 wt% chromium. Chromium was added for air-side oxidation resistance at the expense of worsened molten salt corrosion resistance. This oxidation resistance is unnecessary in cladding materials because they are not exposed to air. Similarly to Haynes 242, the chromium in Hastelloy N may have positive

effects on microstructure and mechanical properties, and it probably slows tellurium diffusion (see Section 2.5.5).

Table 2.5: Nominal composition (weight %) of Hastelloy N. [75]

Material		Ni	Cr	Mo	Fe	Si	Mn	Va	C	Co	Cu	W	Al+Ti
Hastelloy N	min.	71[a]	7[b]	16[b]	-	-	-	-	0.06[b]	-	-	-	-
	max.				4	1	0.8	0.5		0.2	0.35	0.5	0.5

[a] Balance
[b] No min. or max. specified

Hastelloy N performed well for the duration of the MSRE, but two problems were discovered that put into question the viability of its use in MSRs with longer operational lifetimes: (1) the alloy embrittled at elevated temperatures as a result of exposure to thermal neutrons (radiation damage), and (2) grain boundary embrittlement occurred at surfaces exposed to fuel salt as a result of inward diffusion of the fission product tellurium. It was subsequently discovered that tellurium-induced embrittlement can be significantly decreased by making fuel salt sufficiently reducing. After the MSRE had been retired, Hastelloy N variants were developed at ORNL with improved irradiation and tellurium embrittlement resistance. More recently, further improved Hastelloy N variants were developed by Ignatiev et al. [13] at the RRC-Kurchatov Institute. These modified versions of Hastelloy N have superior performance, but they are difficult to obtain and there is a relative lack of usage experience in full reactor conditions. The composition of standard Hastelloy N, two versions of modified Hastelloy N developed at ORNL, and HN80MTY are compared in a table in [76, p. 274]. Their composition is similar enough that the results of corrosion and diffusion studies of standard Hastelloy N are likely to be applicable to modified Hastelloy N alloys.

As mentioned in Section 2.3, Hastelloy N has been successfully coextruded with SS316 [48]. However, it's unknown if an 800H/Hastelloy N composite has ever been fabricated.

A drawback of Hastelloy N is its unavailability in wire or powder form, making it challenging to research as a coextruded or thermal sprayed cladding (this is further discussed

in Section 2.7). However, Hastelloy N is produced in wire form according to Clark et al. [77] who cite an ORNL report: “Although about 200 000 pounds of Alloy N were used in the ORNL Molten Salt Reactor Experiment, only about 3,000 pounds per year are currently made in various product forms (plate, wire, tubing, sheet), being rather specialized (and seemingly proprietary) in use”.

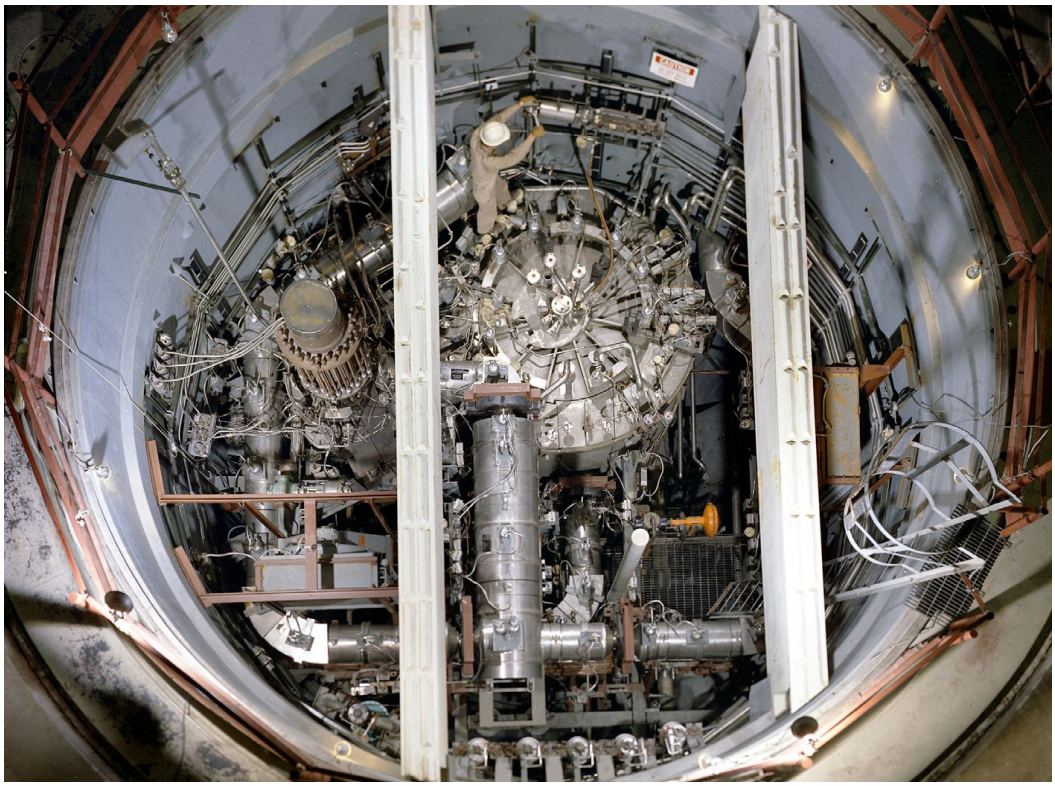

Figure 2.15: Top view of the MSRE. Every component exposed to molten salt was fabricated out of Hastelloy N. The primary heat exchanger is the large cylindrical component in the lower middle of the image, the primary pump is the tall object on the left, and a person is standing on the reactor vessel. [78]

2.5.5 Comparison of cladding alloys

Comparison of resistance to tellurium-induced embrittlement

McCoy and McNabb [79, Sec. 10.1] tested a number of alloys for tellurium-induced embrittlement by electroplating tellurium onto their surface, followed by annealing, straining, and

examination. Both Hastelloy N and Ni 200 formed intergranular cracks. Carlson et al. [79, Sec. 10.4] conducted tellurium diffusion experiments which indicated that tellurium-induced cracking is correlated with depth of tellurium diffusion. They also found that tellurium diffused into Ni 200 more rapidly than in Hastelloy N; this result was confirmed by recent studies (with more accurate measurements) by Cheng et al. [80] for tellurium diffusion into pure nickel and a Ni–16Mo–7Cr wt% alloy (similar composition to Hastelloy N). McCoy [79, Sec. 10.2] suggested that chromium reduces cracking due to reactions between chromium and tellurium at grain boundaries. Jia et al. [81] conducted tellurium diffusion experiments with Ni–7Cr and Ni–15Cr wt% alloys, and their results support McCoy's hypothesis about the beneficial effect of chromium. These experiments indicate that the ideal amount of chromium in alloys exposed to fuel salt is not zero, but rather, some amount that balances tellurium-embrittlement resistance and corrosion resistance (since chromium worsens corrosion resistance).

The slower diffusion of tellurium in Hastelloy N versus in nickel favors Hastelloy N as a cladding material. However, to fully evaluate this advantage, both alloys should be exposed to tellurium-containing molten salt with realistic chemical conditions, such as controlled redox potential (see Figure 2.7), and then creep and fatigue tested. Furthermore, no information could be found in the literature about the resistance of Haynes 242 or Ni–Mo plating to tellurium-induced embrittlement.

Comparison of resistance to irradiation damage

The irradiation conditions that are most relevant to this study are those in the primary heat exchanger of Terrestrial Energy's IMSR®. Due to a lack of knowledge about these irradiation conditions and difficulties finding irradiation resistance data, a comparison of the resistance of cladding materials to irradiation damage was not done by the present author. Before in-depth R&D is conducted for any particular cladding material, a comprehensive review of

their irradiation resistance should be completed. For the irradiation effect of swelling, such a review must compare cladding materials with the structural alloys discussed in Section 2.4.

Comparison of chromium diffusion resistance

Based on measurements by Koger et al. [82], the chromium diffusion coefficient in Hastelloy N at 700 °C is $2.9 \times 10^{-18}\,m^2\,s^{-1}$. This value is more than an order of magnitude smaller than the chromium diffusion coefficient from Olson et al. [34] of $9.5 \times 10^{-17} \pm 3.5 \times 10^{-17}\,m^2\,s^{-1}$ for electroplated Ni on 45.3Fe–31.6Ni–20.4Cr wt% (model alloy for Incoloy 800H). However, these coefficients were measured with entirely different methods, and large variations are common for diffusion coefficients reported in the literature. For these and other reasons, there is a need for more data on the diffusion resistance of candidate structural and cladding alloy combinations.

2.5.6 Cladding materials selected for this research

Nickel and Hastelloy N were selected as cladding materials for thermal aging experiments in this research. Electroplated Ni–Mo and Haynes 242 are worth investigating, but the focus was placed on nickel and Hastelloy N because there is less uncertainty about their suitability as cladding materials.

2.6 Alloy metallurgy

This section summarizes the metallurgical characteristics of the cladding and structural alloys used in this research for the temperatures found in MSRs.

2.6.1 Stainless steel 316H

Stainless steel 316H (SS316H) has an austenitic (face-centered cubic) microstructure that is stabilized by its 10–14 wt% nickel content. σ-phase is the main intermetallic precipitate in SS316H, and its precipitation is caused by the 2–3 wt% molybdenum in the alloy [83]. Based on the time-temperature-transformation (TTT) diagram in Figure 2.16, σ-phase precipitation initiates in SS316H after a few hundred hours of thermal aging at 700 °C, and χ and η (Laves) phases can also form at this temperature. σ, χ, and η phases are intermetallics and embrittle SS316H.

SS316H is less common than its lower carbon variants, SS316 and SS316L, which are often used to avoid intergranular carbide precipitation at high temperatures (e.g. in heat affected zones during welding). In SS316H, $M_{23}C_6$-type carbides, with the metal component primarily consisting of chromium, precipitate in the operating temperature range of MSRs, especially at higher temperatures approaching 700 °C (see Figure 2.16).

Stainless steel 316L (low carbon)

SS316L was used instead of SS316H in this research; the reason for this is discussed in Section 3.1. A TTT diagram for SS316L is shown in Figure 2.17. Due to the lower carbon content in SS316L, $M_{23}C_6$ carbides take longer to appear and the formation of intermetallic phases (σ, χ, and η) is accelerated [84].

2.6.2 Incoloy 800H

Incoloy 800H (referred to as 800H) is an austenitic superalloy that is solid-solution strengthened primarily by chromium. It can be called a modified stainless steel [85, p. 26]. It is commonly used for high-temperature applications in large part because it does not form σ-phase above 649 °C [86]. γ' phase [Ni_3(Al,Ti)] is an intermetallic that precipitates homogeneously throughout the matrix, and while 800H is not primarily precipitation strengthened,

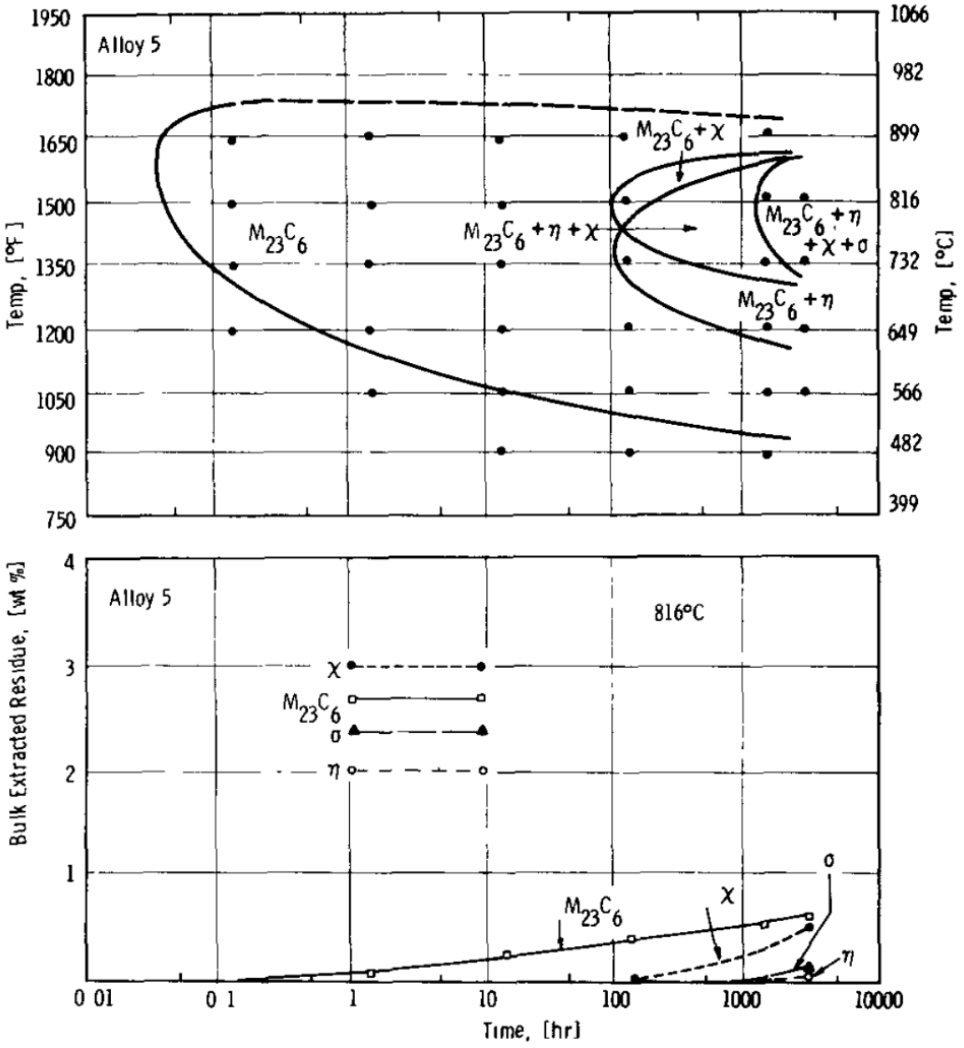

Figure 2.16: TTT diagram of precipitates in SS316 (0.066 wt% carbon content—within the nominal carbon concentration in SS316H), solution annealed for 1.5 h at 1260 °C and water quenched prior to aging. [84]

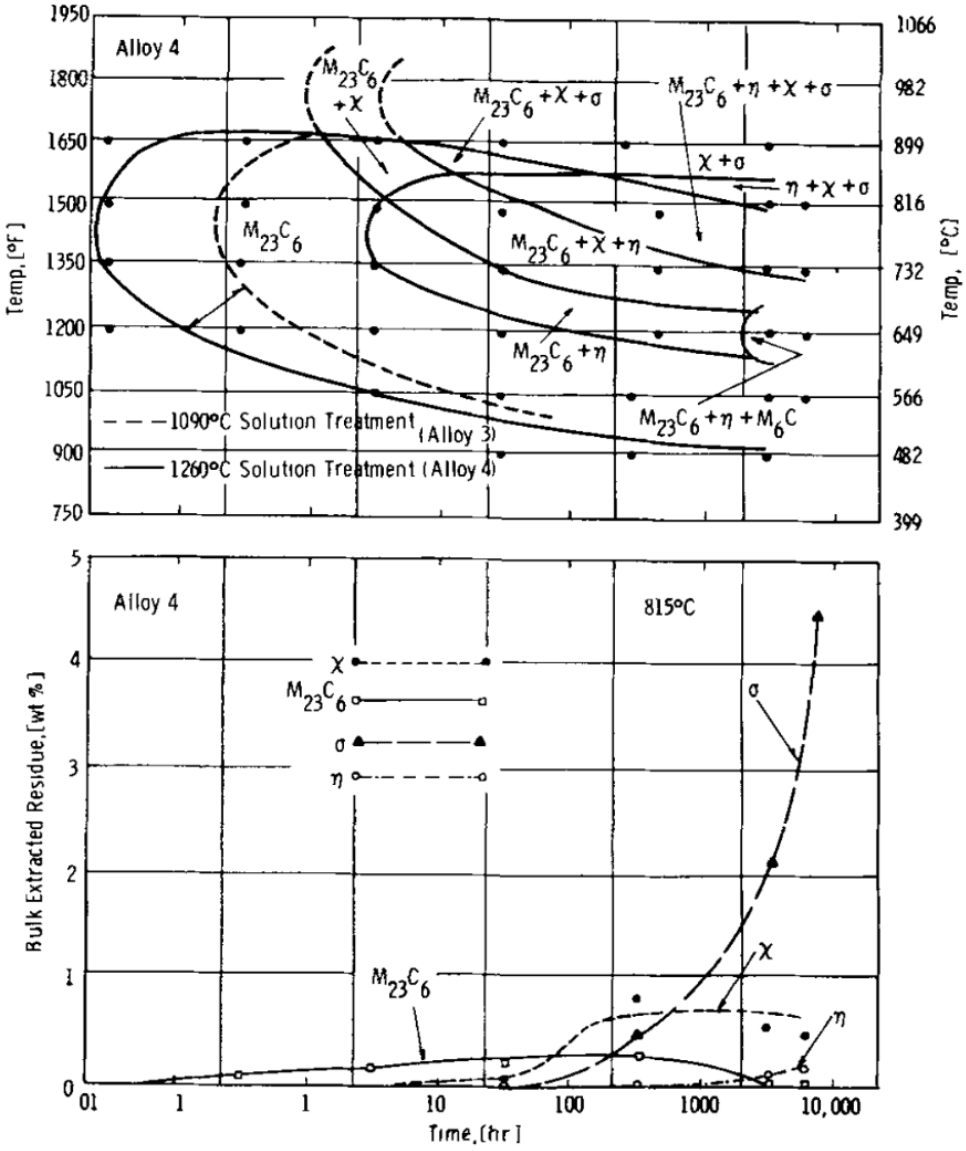

Figure 2.17: TTT diagram of precipitates in SS316L (0.023 wt% carbon content), solution annealed for 1.5 h, water quenched, and 20 pct cold worked prior to aging. [84]

γ' improves its high-temperature strength and creep resistance [87, 88]. Higher content of aluminum and titanium causes more γ' formation. 800H precipitates secondary titanium carbide (TiC) at approximately 850 °C, with $M_{23}C_6$-type carbides predominating at ∼700 °C [89]. This information is supported by the approximate TTT diagram shown in Figure 2.18, which includes $M_{23}C_6$, Ti(C, N), and γ' for an Al+Ti content of ∼0.8% in Incoloy 800. The nominal carbon content in Incoloy 800 is 0–0.10%, versus 0.05–0.10% in Incoloy 800H.

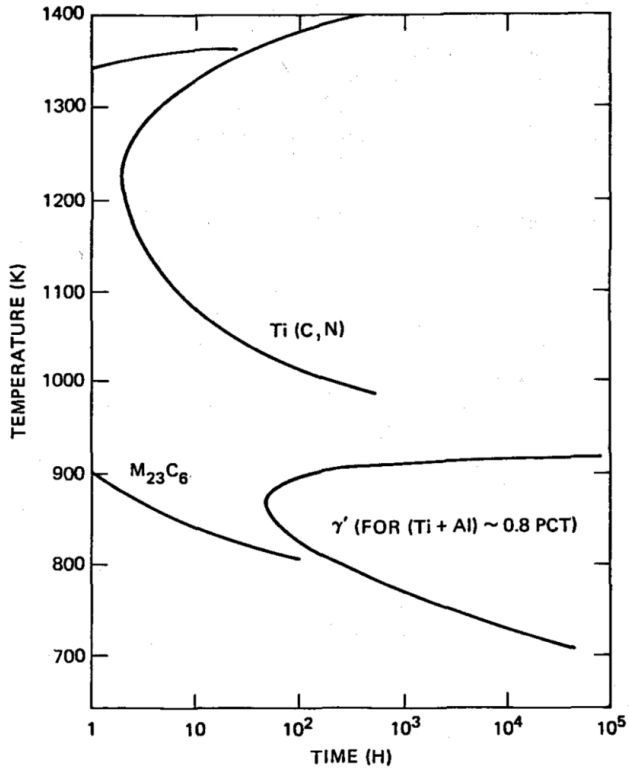

Figure 2.18: Approximate TTT diagram for precipitation of $M_{23}C_6$, Ti(C, N), and γ' in Incoloy 800. [90]

2.6.3 Nickel

Nickel has a face-centered cubic structure. Ni 201 and Ni 200 are commercially pure nickel (minimum 99.0 wt%). Ni 201 has a smaller upper limit on carbon content than Ni 200 (0.02 wt% versus 0.08 wt%). Ni 200 would not be used in MSRs because long-duration exposure to 425–650 °C causes precipitation of graphite and loss of ductility. Ni 201 is useful

for cladding techniques where the cladding precursor is metallic (powder, welding wire, etc.), such as in thermal spraying and coextrusion. Examples of non-metallic precursors are $Ni(NH_2SO_3)_2$ and $NiCl_2$ for electroplating and $Ni(CO)_4$ for chemical vapor deposition (CVD).

2.6.4 Hastelloy N

Hastelloy N is a solid-solution strengthened, nickel-based, austenitic superalloy. Its microstructure consists of stringers of silicon-rich M_6C-type carbides [$(Ni,Si,Fe)_3(Mo,Cr)_3C$] and more finely dispersed M_6C-type carbides concentrated in grain boundaries [22, 91]. The primary metal component of these carbides is molybdenum.

2.7 Selection of cladding techniques for heat exchanger tubes

This section describes and compares various techniques that can be used for fabricating claddings on heat exchanger tubes at a commercial scale. The following list includes the main cladding techniques that are applicable to components in MSRs. Their advantages and disadvantages are summarized in a report by Muralidharan et al. [47].

- Electroplating
- Electroless plating
- Physical vapor deposition (PVD) (vacuum evaporation, sputtering, etc.)
- Chemical vapor deposition (CVD)
- Thermal spray (high-velocity oxy-fuel (HVOF) spray, cold spray, plasma spray, etc.)
- Weld overlay
- Laser cladding
- Coextrusion

Cladding techniques must satisfy the requirements below, in addition to the performance requirements listed in Section 1.4.

1. **Scalability:** Cladding techniques should be scalable for large-scale manufacturing. This requirement ties into the cost requirement of claddings.
2. **Surface accessibility:** If the surfaces to be clad are inaccessible to line-of-site cladding processes or if they have complex geometry, certain cladding techniques are ruled out. For example, cladding the inner surface of tubes requires techniques that are non-line-of-sight, such as coextrusion.
3. **Maintain substrate integrity:** The depth of structural alloy substrate in which composition and microstructure is affected by the cladding fabrication process should be minimized. Thermal stresses from cladding fabrication should also be minimized.

Selection of cladding techniques requires consideration of their advantages and disadvantages with regard to (1) the cladding and substrate materials (e.g. most alloys cannot be electroplated), (2) the geometry of the clad part (e.g. tube or plate, and cladding thickness), and (3) the operating environment (e.g. mechanical stress). Here, the focus is on cladding the outer surface of thin-walled heat exchanger tubes. Examples of layer thicknesses are 0.2 mm for the cladding and 1 mm for the structural alloy. The first step in selecting a cladding technique is eliminating candidates based on their limitations with respect to the intended application. Electroless nickel plating is ruled out because it contains phosphorous contaminants that are undesirable for nuclear applications and because it has poor mechanical properties [47]. Weld overlay and laser cladding are ruled out because their high heat input to substrates make them unsuitable cladding thin-walled parts. According to Davis [92], laser cladding can affect substrates to a depth of 0.5 to 5 mm, with an effect on metallurgical structures similar to welding. It's worth noting, however, that these two cladding techniques are well suited for cladding reactor vessels. CVD is ruled out because it lacks technology readiness. For instance, the processing steps to remove surface oxides from substrates for

improved adhesion have not been developed [47]. In addition, CVD is expensive and lacks scalability. PVD is ruled out for similar reasons of poor adhesion, high cost, and lack of scalability. The remaining cladding techniques are:

- Electroplating
- Thermal spray
- Coextrusion

Hastelloy N cannot be electroplated whereas pure nickel can. Both, however, can be thermal sprayed and coextruded. The following subsections will compare electroplating, thermal spray, and coextrusion for nickel, and thermal spray and coextrusion for Hastelloy N.

2.7.1 Electroplating

Electroplating is a process that uses electric current to reduce metal cations from a plating solution (i.e. electrolyte) onto a component that acts as a cathode. The anode can act as a source of cations to maintain the solution's concentration. The amount of material that is plated depends on the amp-hours of current (i.e. number of electrons) that pass through a plating cell. Plating thickness varies over the surface of cathodes due to varied electrical resistance in the circuit (a result of varied distance between anodes and cathodes, the chemistry balance in the plating solution, and the geometry of the electrodes, which have their own internal voltage drops).

While electroplating does not require direct line-of-sight access, the geometry of components that can be plated is limited. For long tubes, it is considerably more challenging to plate their inner surface than their outer surface. Plating the inside of tubes can be done by running an anode wire down their center and by pumping solution through the tubes to maintain the right chemistry balance. The inner surface of long and narrow and also curved

tubes can be prohibitively difficult to plate. Nonetheless, electroplating remains versatile for cladding some complex geometries (e.g. the internal components of a pump).

Nickel electroplating is a widely used and inexpensive process. There are several different nickel plating solution chemistries, each involving different chemicals and plating parameters (voltage, temperature, pH, etc.). Nickel sulfamate plating is used for many engineering applications and is optimal for MSRs in part because it produces nickel plating with low internal stress and good ductility.

Electroplating typically produces metal with small grains, which is a disadvantage due to the diffusion-accelerating effect of increasing grain boundary area (see Section 2.2.2). Another drawback of electroplating is the lack of microstructural mixing at interfaces with structural alloy substrates compared to the cladding techniques of thermal spray and co-extrusion. Composites with sharp interfaces are prone to having greater interfacial stress from differences in thermal expansion and radiation-induced swelling. This can lead to delamination or cracking. The two disadvantages of small grain size and sharp interfaces are countered by heat treating electroplated claddings to increase their grain size and to cause interfacial mixing. Olson [16] investigated this approach and observed that increased grain sizes did not reduce diffusion rates, but they noted that more thermomechanical processing parameters could be tested.

Substrates immersed in plating baths are exposed to hydrogen from the small amount of water electrolysis that occurs simultaneously to the plating of metal ions. This can result in hydrogen embrittlement. From a cursory search of the literature, hydrogen embrittlement shouldn't be a problem for SS316 and 800H.

A disadvantage of electroplating is the limited compositions that are possible compared to melted alloys, which often include minor alloying additions for improving certain properties, such as irradiation resistance. For example, Ni–Mo plating may be diffusion resistant and

corrosion resistant, but its irradiation resistance may be inadequate and, compared to melted alloys, there is less flexibility for modifying its composition to improve irradiation resistance.

2.7.2 Coextrusion

Coextrusion is "the simultaneous extrusion of two or more metals to form an integral product" [93]. To form a heat exchanger tube with one or two clad sides, a two or three layered billet is extruded into a thin-walled composite tube. The cladding and structural alloys are metallurgically bonded together either during the hot extrusion step or during billet fabrication by weld overlaying the cladding layer. For the method of metallurgical bonding during extrusion, the billet consists of inner and outer sleeves depicted in Figure 2.20 (sleeve coextrusion). According to Short [55], weld overlaying is the best method for ensuring adhesion and microstructural mixing at the interface between the layers. The weld overlay process is illustrated in Figure 2.19. After weld overlaying, the billet is machined down so that the weld overlayed side is smooth. The billet is then hot extruded, which involves heating the billet to around 100–200 °C below melting points, applying a lubricant (e.g. molten glass), and rapidly forcing the billet through a die and mandrel. By controlling the thickness of the layers and the geometry of the die and mandrel, the end thickness of each layer can be controlled. After extrusion, the composite tube is cold pilgered (a longitudinal rolling process) to further reduce its diameter. "This method is favorable to others such as tube drawing, especially for a multilayer tube, because pilgering puts the entire composite under compressive forces. Tube drawing would apply tension to the layers, which could cause them to separate" [55].

While coextrusion doesn't require specialized extrusion equipment, the process does require significant investment to be developed for specific materials and dimensions. Once it is developed, however, long lengths of tubes can be fabricated efficiently with a high throughput. Also, a capability that is almost unique to coextrusion is cladding the inner

surface of tubes. This capability would be useful if fuel salt travels inside rather than outside heat exchanger tubes.

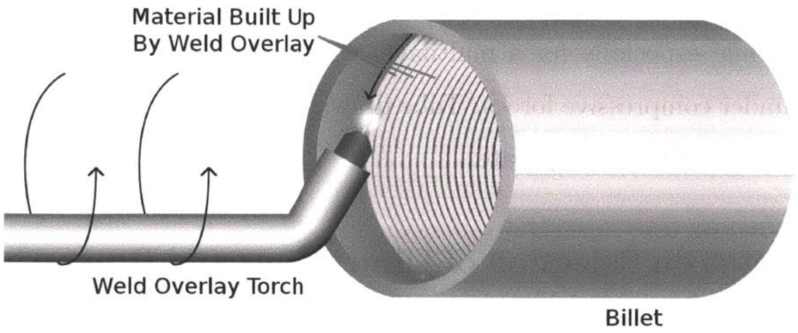

Figure 2.19: Schematic illustration of weld overlaying the inner surface of an extrusion billet: the welding torch rotates inside the bore, or the billet rotates around the torch, while the torch is slowly retracted. A spiral overlapping weld bead is deposited. Multiple passes can be made to build up a thicker coating. This process is equally applicable to weld overlaying the outer surface of an extrusion billet. [55]

2.7.3 Thermal spray

"Thermal spray is a generic term for a group of processes in which metallic, ceramic, cermet, and some polymeric materials in the form of powder, wire, or rod are fed to a torch or gun [...]" [95]. The resulting molten or nearly molten droplets of material or particles of solid material are accelerated in a gas stream and projected against a substrate. On impact, the droplets or particles flow into thin, overlapped and interlocked lamellar particles that are adhered to the substrate.

Unlike weld overlay or laser cladding, thermal spraying can be performed with minimal heating of substrates, making it viable for cladding thin-walled components. The bond strength between thermal sprayed claddings and their substrate is generally strong. Thermal spraying is a line-of-sight process; as such, it is only applicable on surfaces such as the outside of heat exchanger tubes. However, it has the advantage of being applicable for field fabrication or repair.

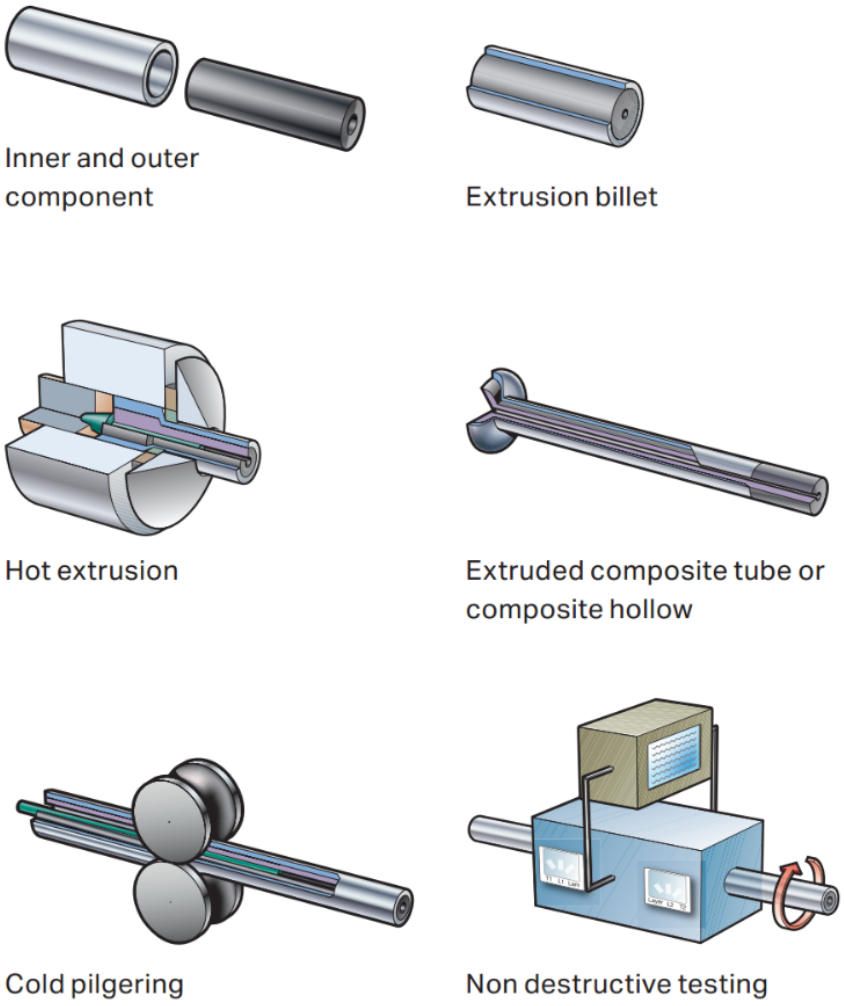

Figure 2.20: Sleeve coextrusion process steps used by Sandvik, a leading manufacturer of composite tubes. [94]

There are several types of thermal spray processes, each with varying cost and performance. For the application of claddings on heat exchanger tubes, the need for low porosity and high bond strength favors the thermal spray processes of high-velocity oxy-fuel (HVOF) spraying and cold spraying. Particles are sprayed at higher kinetic energies in HVOF and cold spraying than in other thermal spray processes. In the HVOF process, a mixture of fuel and oxygen is combusted continuously, producing a hot, high-pressure stream of gas. Metal powder is injected into this stream of gas, accelerated to supersonic velocities, and partially melted before depositing on a target. An image of HVOF spraying is shown in Figure 2.21. In the cold spray process, metal powder is propelled by pressurized inert gas at lower temperature than HVOF gas streams. The particles remain solid in-flight, but their high kinetic energy causes them to deform plastically upon impact and bond mechanically to the substrate. Due to lower temperatures and the oxygen-free carrier gas, cold spraying can produce coatings with fewer oxide impurities than HVOF. Also, due to the lower heat input, cold spraying reduces the need for substrate cooling and eliminates the issue of solidification stresses. However, cold spraying has the disadvantage of having only recently become commercially available and of there being relatively little cladding performance data compared to HVOF.

Figure 2.21: HVOF spraying of a tube or shaft. The flame that carries metal particles can be seen exiting the spray gun. In contrast, there is no flame in the cold spray process, but only an invisible stream of particles. [96]

Chapter 3

Experimental methods

The objective of this research project is to determine the high-temperature durability of four structural and cladding material combinations (composites) by exposing them to high temperatures for an extended period of time. This objective is divided into two streams of work:

1. Measuring concentration profiles of major (>1 wt%) alloying elements in thermally aged composites in order to extrapolate their diffusion to end of reactor lifetimes.
2. Identifying any embrittlement and microstructural changes in the interfacial zone of thermally aged composites.

Thermal aging experiments consisted of fabricating composite samples, heat treating them in an inert environment for an extended period of time, characterizing their microstructure, and measuring concentration profiles of diffusing elements in the direction normal to substrate–cladding interfaces. The two methods used for fabricating composite samples are diffusion bonding and electroplating. In the rest of this chapter, the methods used for performing experiments and subsequent analysis are described.

3.1 Alloy procurement

The structural alloys in this research are Incoloy 800H and stainless steel 316H. For diffusion bonding, the cladding alloys are Hastelloy N and Ni 200. It was not possible to source SS316H sheet—the thinnest SS316H that could be found is 9.5 mm plate from Sandmeyer Steel Company. Straight-grade SS316 has a carbon content of 0–0.08 wt%, which overlaps with the 0.04–0.10 wt% carbon content of SS316H between 0.04 and 0.08 wt%. However, it was not possible to find straight-grade SS316 with a carbon content between 0.04 and 0.08 wt% because this alloy is usually double specced as SS316L/316 which limits its carbon content to the upper limit of SS316L of 0.03 wt%. Therefore, SS316L was used instead of SS316H. This is suboptimal because SS316H is the only version of the 316 group that is codified in the ASME BPVC (see Section 2.4).

As discussed in Section 2.6.3, Ni 200 would not be used in MSRs because of its high carbon content and the resulting graphite and carbide precipitation. The reason Ni 200 was used is that McMaster-Carr, the supplier of Ni 200, provided a mill certificate which indicated that the alloy's carbon concentration was 0.01 wt%, which is within the specifications for Ni 201. After experiments were over, it was determined by independent carbon concentration measurement that the Ni 200 alloy used in this research has a carbon concentration of 0.05 wt%, which is not within the specifications for Ni 201. McMaster-Carr acknowledged that they provided the wrong mill certificate and then provided the correct one which is consistent with the independent carbon concentration measurement. The results for diffusion couples with Ni 200 are in Appendix B. For reasons shown in Appendix B, these results have far less relevance than if carbon concentration of the Ni 200 was within the spec for Ni 201, but they still retain value by highlighting the importance of not using cladding alloys with significantly greater carbon activity than underlying structural alloys.

The composition of the SS316L, 800H, Hastelloy N, and Ni 200 used in this research are shown in Table 3.1. SS316L and Ni 200 sheet were obtained from McMaster-Carr,

Hastelloy N sheet was provided by Haynes International, and Incoloy 800H sheet was obtained from ATI. Sheet thickness of ∼1.5 mm was selected to satisfy the semi-infinite condition of Equation 2.14 for the thermal aging temperatures and durations in this work (detailed in Section 3.4). The four alloys were received in the cold rolled and annealed condition.

Table 3.1: Composition (weight %) of alloys used in this study, according to their mill certificates.

	Fe	Cr	Ni	Mo	Mn	Al	Ti	Cu
800H	47.0	20.51	30.30	-	0.57	0.50	0.55	0.04
SS316L	bal.	16.76	10.03	2.02	1.55	-	-	0.35
Hast. N	4.13	7.22	bal.	16.82	0.49	(Al+Ti) = 0.23		0.06
Ni 200	0.01	-	99.70	-	0.15	-	-	0.02
	C	B	Si	N	Co	W	P	S
800H	0.07	-	0.32	0.011	0.04	-	0.010	0.0002
SS316L	0.025	-	0.25	0.040	-	-	0.028	0.015
Hast. N	0.060	0.004	0.25	-	<0.1	<0.1	<0.002	<0.002
Ni 200	0.05	-	0.07	-	-	-	-	0.001

3.2 Diffusion bonding

Diffusion bonding was used for fabricating diffusion couples (two-layered coupons) of cladding and structural alloys. In the diffusion bonding process, two materials are heated at recrystallization temperatures while in a vacuum and under several MPa of compressive load—enough to cause creep but below the materials' yield points. The oxide layers on the materials rupture due to microplastic deformation and dissolve into the metal lattices, resulting in a metallurgical bond (continuous metal–metal bond with no interfacial oxide layer, voids, or discontinuities). The stages of interface evolution during diffusion bonding are illustrated in Figure 3.1.

Diffusion bonding is rarely used for fabricating claddings at industrial scale, so it's unlikely to be used for fabricating claddings in MSRs, especially for tubes (note that diffusion bonding isn't included as a cladding technique in Section 2.7, which is a comparison of cladding techniques for heat exchanger tubes). The advantage of diffusion bonding is that it allows for many cladding and structural material combinations to be bonded with less cost and complexity than full-scale cladding processes. Ideally, however, thermal aging experiments would use the same cladding fabrication techniques that would be used at full scale because the microstructure that results from these fabrication techniques can affect diffusion and microstructural evolution.

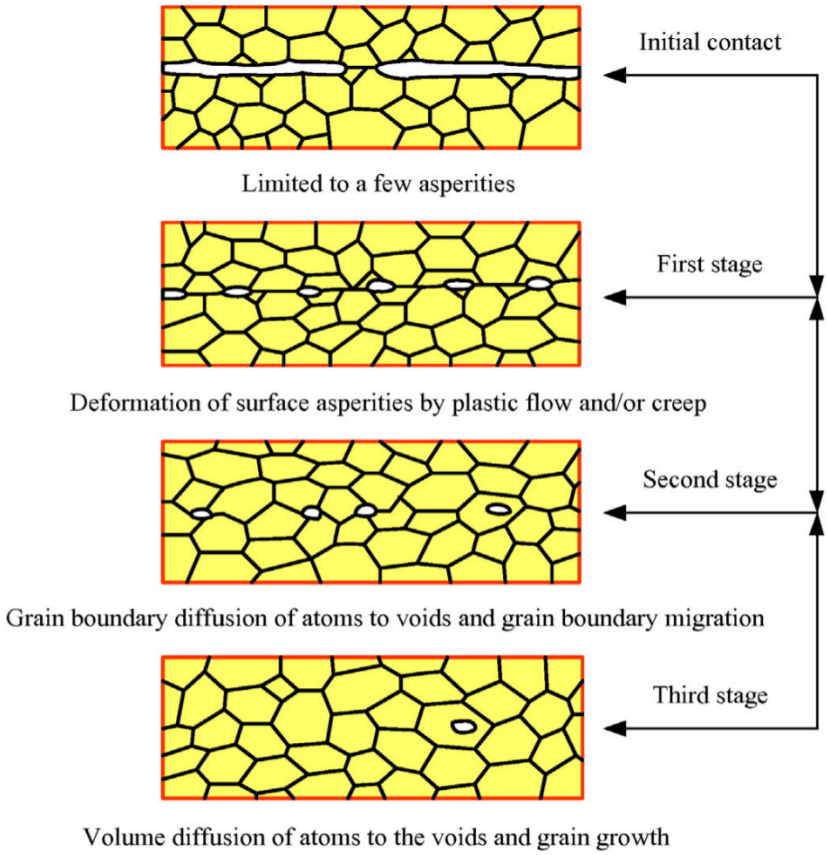

Figure 3.1: Schematic illustration of the microscopic evolution of bonding interfaces during diffusion bonding. [97]

3.2.1 System and process description

The diffusion bonding rig used in this research is shown in Figure 3.2. The assembly that holds the samples is in a vertical quartz tube under a vacuum on the order of 10^{-4} Torr. The samples were heated for 2 h at 900 °C in a furnace that surrounds the vertical quartz tube and compressed together by a static load of approximately 45 kg from a lever assembly to create approximately 7 MPa of bonding pressure. The 2 h duration was chosen for balancing bond quality and minimized diffusion during the bonding process. The accuracy of the furnace controller temperature readout was confirmed with a separate ice-bath-referenced type R thermocouple.

Figure 3.3a is a schematic illustration of the compression assembly. The graphite ball prevents transfer of torque so that interfacial bonding pressure is evenly distributed. Figure 3.3b shows the sample holder during the assembling of the compression rig. To avoid oxidation from residual oxygen in the vacuum, titanium getter foil was wrapped around the sample holder.

The temperature program for diffusion bonding is shown in Figure 3.4. At low temperatures, the temperature controller was incapable of adequately controlling temperature with the inner thermocouple because of thermal insulation from the vacuum between the inner thermocouple and the furnace coils. At high temperatures, the controller did not have this issue. A thermocouple outside the vacuum, between the quartz tube and the furnace coils, was used for the first part of the temperature ramp up, and the controller's temperature input was switched to the thermocouple inside the vacuum once the controller's readout reached 750 °C. The thermal inertia and thermal resistance of the diffusion bonding assembly required the temperature setpoint in the program to be reduced at the thermocouple switch. Temperature ramping was limited to 200 °C per hour to allow vacuum pressure stabilization and to avoid damaging the furnace. After the 2 h soak at 900 °C, furnace heating stopped and the diffusion bonding assembly air cooled from the outside while still under vacuum (the air

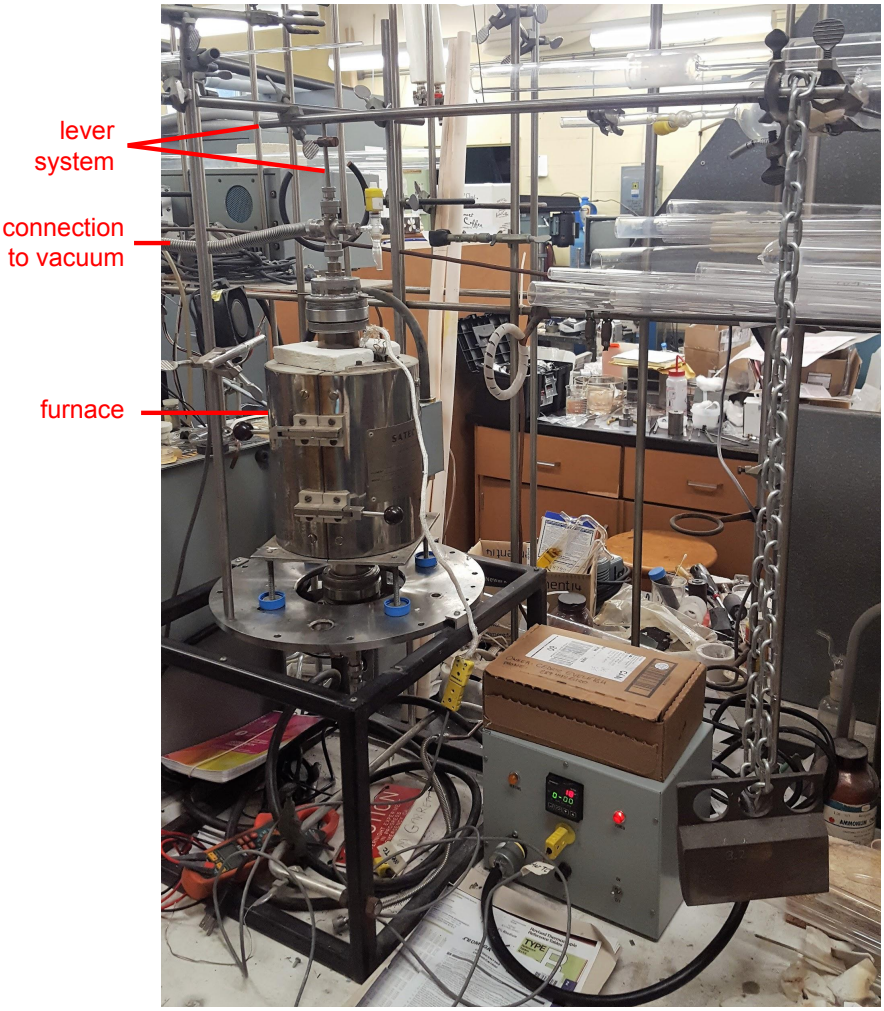

Figure 3.2: Diffusion bonding rig with a vertical tube furnace connected to a vacuum system and a lever system for applying compressive load to three diffusion couples in the furnace.

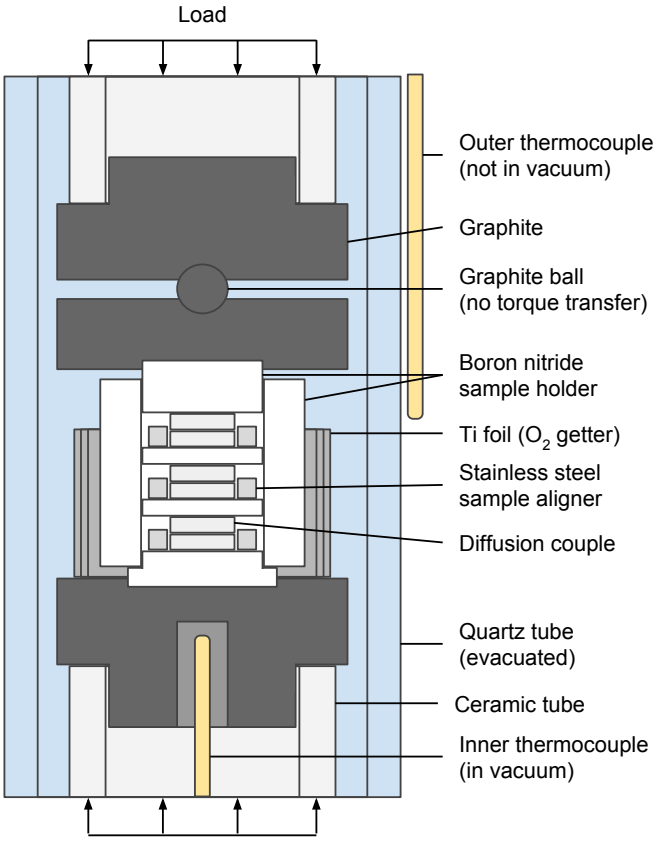

(a) Schematic illustration of the diffusion bonding compression assembly.

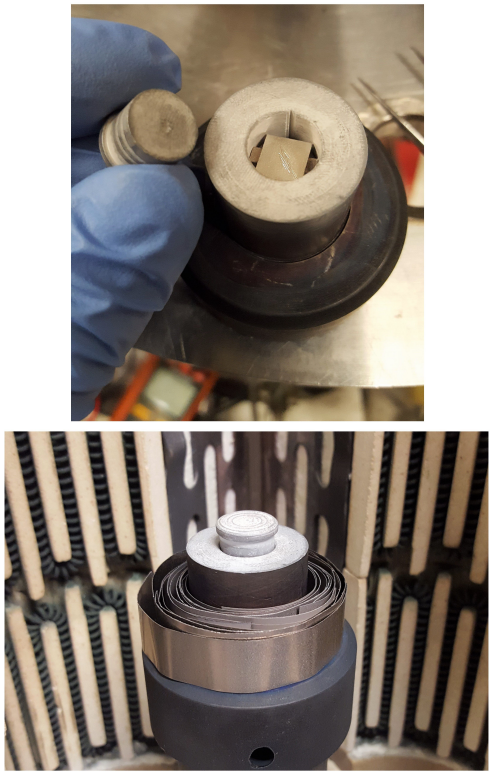

(b) Assembly of sample holder (top) and assembled sample holder with Ti foil (bottom).

Figure 3.3: Compression assembly in the diffusion bonding rig.

cooling segment in Figure 3.4 is roughly fit to measured temperature data). Boron nitride is hygroscopic and absorbs moisture when exposed to air, so temperature was held for 31 min at approximately 200 °C to allow the boron nitride sample holder to outgas. Also, the boron nitride sample holder was kept in a desiccator between diffusion bonding runs to minimize moisture absorption.

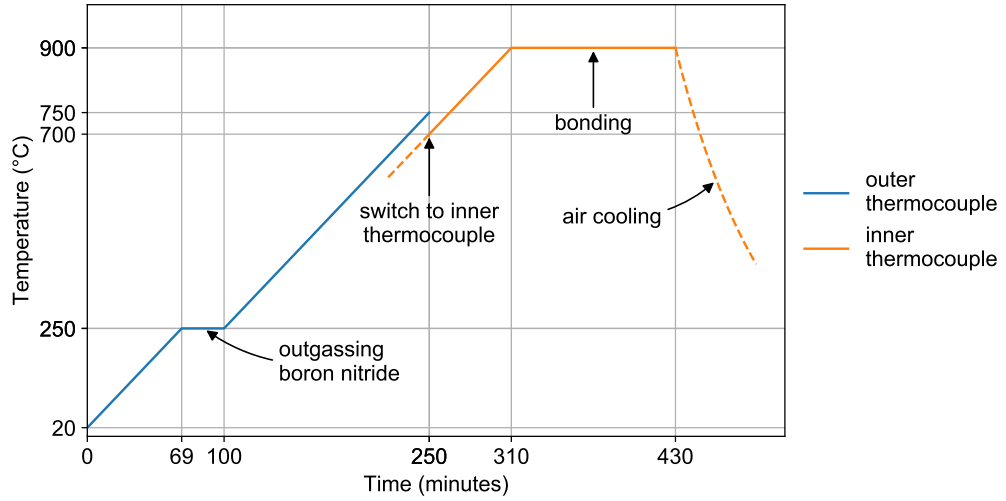

Figure 3.4: Temperature program for diffusion bonding. The inner thermocouple was located inside the vacuum near the samples, and the outer thermocouple was located outside the vacuum between the quartz tube and the furnace coils (see Figure 3.3a). The rate of temperature ramping was 200 °C per hour.

3.2.2 Pre-bonding sample preparation

8 mm × 8 mm coupons were sectioned from the 1.5 mm thick sheet materials of 800H, SS316L, Ni 200, and Hastelloy N. Coupons were mounted with thermosetting glue to the sample holder shown in Figure 3.5, which was custom fabricated for the purpose of holding coupons flat during grinding and polishing. With an auto-polish machine, the bonding side of coupons was ground with P500 and P1200 grit SiC paper, and polished with 3 µm and 1 µm diamond suspensions. Coupons were then cleaned in an ultrasonic acetone bath and rinsed with ethanol.

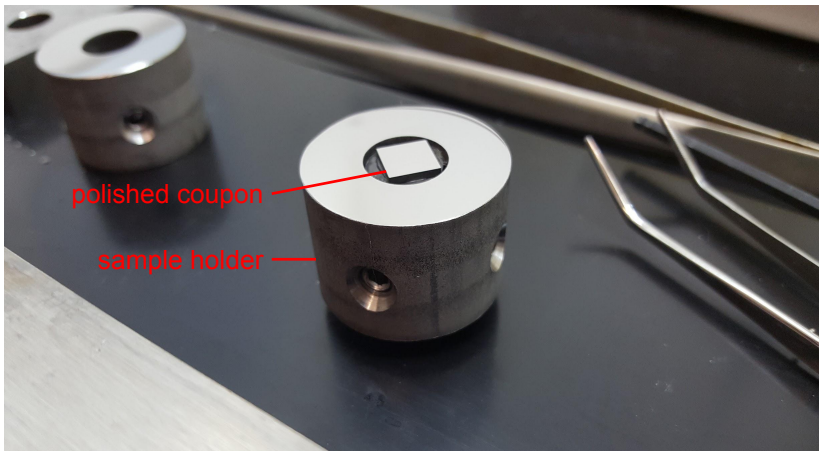

Figure 3.5: Sample holder custom fabricated to hold coupons flat during grinding and polishing. Six of these sample holders were used to prepare six coupons at a time with an auto-polish machine in order to make three diffusion couples.

3.2.3 Profilometry of bonding surfaces

The polished bonding surfaces of the four alloys were profiled with an Alicona InfiniteFocus optical microscope. Surface profilometry is useful for optimizing bonding surface preparation and for ensuring reproducibility of experimental procedures.

3.3 Nickel electroplating

Once initial microstructure characterization results had been obtained for diffusion couples with Ni 200, it was decided that nickel electroplating (referred to here as Ni plating) should be tested for comparison. In contrast with diffusion bonding, electroplating could be used in the fabrication of claddings for reactor components. 1.5 mm thick coupons of SS316L and 800H were ground using up to P2400 grit SiC sandpaper and Ni-plated by Cooper Plating Inc. in Ontario, Canada with the following process steps:

1. Soak clean
2. Electroclean to remove native oxides
3. Wood's nickel strike for adhesion to stainless steels

4. Nickel sulfamate plating

A current density of 86–108 $A\,m^{-2}$ was used for the nickel sulfamate process, and a minimum plating thickness of 0.1 mm was specified.

3.4 Thermal aging

Diffusion couples and electroplated samples were encapsulated in quartz ampoules (12 mm ID, 16 mm OD, and ∼120 mm length) evacuated to a pressure of approximately 10^{-4} Torr. Titanium foil was included in the ampoules to getter residual oxygen, except in the ampoules with Ni-plated samples due to a communication mistake, although there was no visible oxidation of samples in either case. Figure 3.7 shows the glassblowing process for ampoule fabrication, and Figure 3.6 is an image of ampoules prior to thermal aging. The ampoules were placed in an open-air box furnace at 700 °C for the times shown in Table 3.2. The thermal aging temperature of 700 °C was chosen because it is a commonly assumed upper temperature limit for the primary circuit of MSRs due to structural and corrosion limitations. The accuracy of the furnace controller temperature readout was confirmed with a separate ice-bath-referenced type R thermocouple.

Ideally, diffusion tests would be performed at several temperatures so that the pre-exponential factors and activation energies of diffusion coefficients can be determined, allowing diffusion to be predicted at temperatures other than those tested for in diffusion experiments. In this project, longer thermal aging times and multiple material combinations were prioritized in favor of thermal aging at multiple temperatures.

Control diffusion couples were fabricated for comparing microstructure and measuring the amount of diffusion that occurred during diffusion (necessary for calculating diffusion coefficients). For diffusion couples, each set of experimental parameters of material combination and thermal aging time was triplicated to decrease experimental uncertainty. The

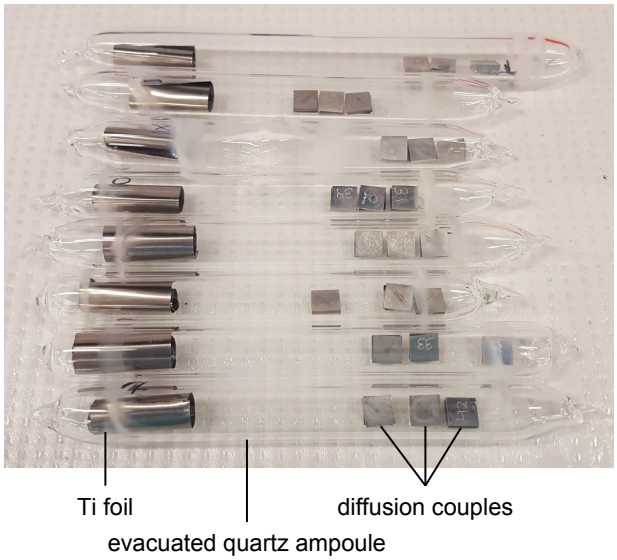

Figure 3.6: Evacuated quartz ampoules ($\sim$120 mm in length), each containing three diffusion couples and titanium foil as oxygen getter. This image was taken prior to thermal aging at 700 °C. Ampoules with Ni-plated samples are not shown.

Figure 3.7: Glassblowing process for fabricating ampoules. Left: constricting a quartz tube containing samples before evacuation. Right: collapsing the constriction with the tube under a $\sim 10^{-4}$ Torr vacuum. These images were taken through one of the lenses of a pair of glassblowing glasses.

expected sources of variability between triplicated diffusion couples are from pre-bonding grinding and polishing, and from diffusion bonding. For this reason, each group of three diffusion couples bonded at the same time was for one material combination and included one diffusion couple for each thermal aging time of 0 h (control), 1460 h, and 5840 h, so that diffusion measurements of control diffusion couples would be directly applicable to the thermally aged diffusion couples bonded at the same time. This is illustrated in Figure 3.8.

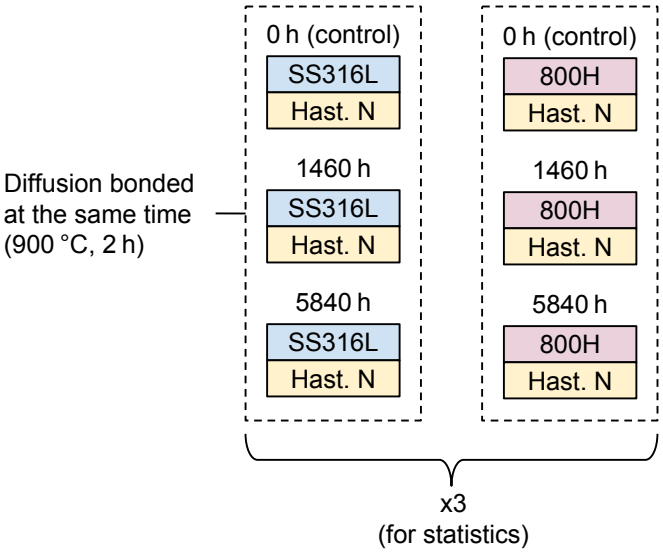

Figure 3.8: Graphical representation of the two diffusion bonding material combinations, of which diffusion couples are bonded at the same time, of which diffusion couples are thermally aged for how long, and of the triplication of each diffusion couple. This same experimental configuration was used for Ni 200 as a cladding material (for context, see Section 3.1).

For the thermal aging of diffusion couples (not the Ni-plated samples), an interruption in thermal aging occurred at 175 h of aging, where the furnace's temperature decreased to 630 °C over the span of 0.5 h and then rapidly resumed 700 °C. A more important interruption occurred at 1571 h of aging due to an university-wide power outage in the middle of the night. The furnace temperature decreased to 332 °C over a period of 9.5 h before power was resumed and the furnace temperature increased back up to 700 °C. The effect of these interruptions on effective thermal aging times was deemed negligible because they were both a small fraction of a percent of total aging time. However, the slow decrease in temperature during

the nine and a half hour loss of furnace power may have had an effect on the microstructure of diffusion couples.

Table 3.2: Thermal aging test matrix. The time values in months are approximate.

	Diffusion couples	Ni-plated samples
Aging temperature	700 °C	700 °C
Aging time	0 h (control) 1460 h (2 months) 5840 h (8 months)	0 h (control) 1461 h (2 months) 3855 h (5.3 months)

3.5 Analysis procedures

The materials characterization techniques that were used are optical microscopy; SEM microscopy; EDS line scans, point scans, and mapping; EBSD mapping; and microhardness line scans. Microhardness analysis provides high-level information about microstructure evolution and about whether interfacial embrittlement occurred. Microscopy, EDS, and EBSD analysis reveal information that is necessary for explaining microhardness results and interpreting diffusion results.

3.5.1 Sample preparation

Diffusion couples and Ni-plated samples were sectioned with a SiC blade in a precision cutting machine. The sectioned samples were then ground with P500 and P1200 grit SiC paper, and polished with 3 µm diamond, 1 µm diamond, and colloidal silica (OP-S) suspensions.

3.5.2 Etching and optical microscopy

Epoxy-mounted sections of samples were etched with an aqua regia solution of three parts hydrochloric acid, one part nitric acid, and two drops of glycerol per 40 mL of solution, and then they were analyzed with a Nikon Eclipse LV100 optical microscope. Compared to monolithic materials, composites are difficult to etch because the two materials that form a composite can require different etchants and they can act as a galvanic couple, causing one alloy to be overetched or stained while the other is left untouched. Careful masking or swabbing is sometimes required to properly etch all regions of composite samples. Fortunately, for the material combinations in this research, soak etching with aqua regia and stirring of the etching solution was effective at revealing grain boundaries and precipitates. Etch times were approximately 2 min for microscopy of as-received alloys and diffusion couple interfaces, 4 min for grain size analysis of as-received Hastelloy N, and 10 min for grain size analysis of diffusion bonded Hastelloy N (this 10 min etching time was needed because of the presence of adjacent structural alloys that are preferentially attacked by the etchant). Electron backscatter diffraction (EBSD, described later in Section 3.5.5) was also used for analyzing grain size and shape, particularly for Ni-plated samples. For grain size analysis, cross-sectional micrographs were perpendicular to interfaces, and this involves an assumption that grains were equiaxed. This is most likely a reasonable approximation because the sheet materials were received in the annealed condition.

Average grain sizes were calculated using the planimetric method described in the ASTM E112–13 standard. In grain size analysis for investigating the cause of changes in hardness, twin boundaries were considered as grain boundaries because twin boundaries act as a barrier to dislocation movement just like grain boundaries do. However, in grain size analysis for determining diffusion coefficient regimes, twin boundaries were *not* considered as grain boundaries because, compared to grain boundaries, twin boundaries are not a good pathway for accelerated diffusion.

3.5.3 SEM

Materials were micrographed with two scanning electron microscopes (SEM): a JEOL 6610LV and an FEI Versa 3D. In all SEM analysis, accelerating voltage was 15 keV and working distance was 10 mm. Both backscatter electron (BSE) and secondary electron (SE) imaging modes were used. BSE imaging reveals more information about compositional contrast and SE imaging reveals more information about surface morphology and topography.

3.5.4 EDS

Concentration profiles, point scans, and element distribution maps were collected with energy dispersive X-ray spectroscopy (EDS) in SEMs. An Apollo X SDD detector was used in the FEI SEM for line scans of non-thermally-aged and 1460-hour-aged diffusion couples, and an Oxford X-max 20 mm^2 silicon drift detector was used in the JEOL SEM for line scans of 5840-hour-aged diffusion couples and Ni-plated samples.

Line scans were taken at 9 locations for each sample. Due to triplication of diffusion couples, a total of 27 line scans were collected for each diffusion couple material combination and aging time. Ni-plated samples were not triplicated, so 9 line scans were collected for each Ni plating material combination and aging time.

For EDS line scans, the elements included in normalizations of concentration data were selected based on having concentrations greater than 1 wt% in the bulk alloys. Low-concentration and low-atomic-number elements (such as carbon) cannot be measured accurately with EDS, so including them in normalizations of concentration data would cause systematic error. This limitation of EDS is a drawback for the diffusion studies in this work. As discussed in Section 2.2.1, the thickness of the diffusion zone in structural alloys is probably defined by loss of mechanical properties from compositional change. Therefore, since low-concentration alloying elements—such as titanium and aluminum, which form strengthening γ' precipitates in 800H—can have a major effect on mechanical properties, the

diffusion of these elements should also be studied. This implies the use of other measurement techniques than EDS.

The working distance for EDS analysis was 10 mm and accelerating voltage was 15 keV. Dwell time was 5 s for line scans, 20–30 s for point scans, and 0.5 s for maps. The five elements of interest in these diffusion studies are Cr, Mn, Ni, Mo, and Fe. Kα energies are roughly 5.4 keV for Cr, 5.9 keV for Mn, 7.5 keV for Ni, 6.4 keV for Fe, and the Lα for Mo is roughly 2.3 keV. Beam energies are often recommended to be at least twice (or 4–5 keV higher than) the highest X-ray emission energy of the elements being analyzed, hence the decision to use a beam energy of 15 keV. Further increasing the beam energy would reduce the spatial resolution of the EDS analysis (because the diameter of interaction volumes increases with accelerating voltage).

There is a minimum diffusion length for concentration profiles to be measurable with EDS. This is because the spatial resolution of EDS is limited by the size of interaction volumes, which are typically 1–2 µm in diameter in SEMs, depending on the instrument's accelerating voltage and the material being analyzed. In this study, the spacing between EDS point measurements in line scans was generally 1–2 µm.

The EDS analysis in this study was standardless, meaning that no reference materials with known composition were used to determine matrix effect correction factors—rather, these were calculated by the instrument manufacturer's software. This is standard procedure for samples with varied composition, like diffusion couples, but is worth noting because it means that the EDS measurements in this study can only be considered semi-quantitative. Also, EDS measurements of elements with low concentration or with small atomic number (e.g. carbon) are qualitative. There are two main reasons why standardless analysis has become standard procedure for analysis such as line scans in diffusion couples: (1) EDS line scans analysis would be severely complicated by the use of reference materials. In composites, which have a range of composition at their interface, several reference materials would be required across

their interface in the direction of diffusion, with each reference sample resembling the local composition as closely as possible. (2) There is little improvement in quantitative accuracy from the use of reference materials up until a certain dwell time[1] (for a given X-ray count rate). For EDS line scans, which are several EDS point scans in a line, the dwell time needed for the use of reference materials to be helpful may lead to excessive analysis time.

The alloys in this work have known composition from mill certificates (Table 3.1). These known compositions were compared with EDS measurements outside diffusion zones (at the ends of line scans) for evaluating the systematic error from standardless analysis and also as a verification that no procedural mistakes took place.

3.5.5 EBSD

Electron backscatter diffraction (EBSD) was used for analyzing grain size and shape. Compared to etching and optical microscopy, it has the advantage of being unaffected by sharp composition changes at bonded interfaces and also of higher possible magnification. Its disadvantages are high cost and more time required to collect an image. The spatial resolution of EBSD maps in this work is 0.1–0.2 µm.

There was no drift correction available in the software used for EBSD data collection; as a result, some of the maps shown in this thesis are slightly curved. This measurement artefact does not affect qualitative results, but in the EBSD maps where it occurs, the reader is notified in corresponding figure captions.

3.5.6 Microhardness tests

Vickers microhardness profiles were measured with a Matsuzawa MMT-X hardness tester shown in Figure 3.9a. The diagonal length of indents was automatically measured by

[1] During a line scan, the electron beam is controlled by scanning coils to be held at fixed points along a pre-determined line for an amount called the dwell time, usually measured in microseconds. The longer this dwell time, the more X-rays will be detected, making it easier to separate the background from the peaks and to calculate the accurate X-ray intensity in these corrected peaks.

the instrument, with a few exceptions of unusual visual features of indents that prevented automatic measurement. An indentation force of 100 gf was used for all measurements.

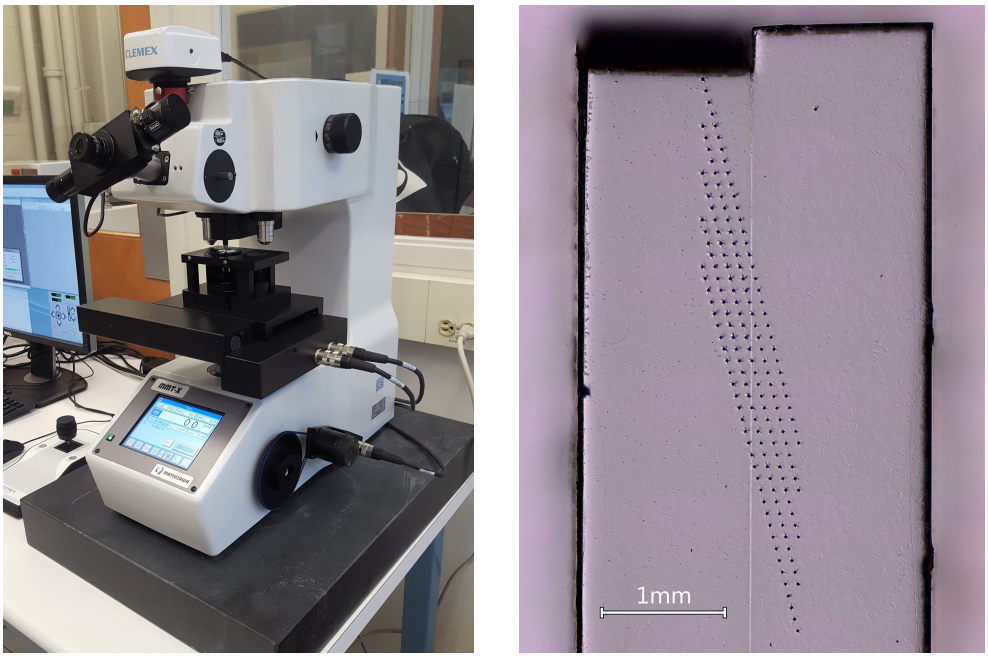

(a) (b)

Figure 3.9: Left: Automatic microhardness tester. Right: Cross-sectional optical micrograph a microhardness indentation pattern of five diagonal lines across the interface of a diffusion couple.

In order to avoid overlap of the plastic deformation zones around indents and the resulting measurement error, the distance between indents and between indents and the edges of samples was kept to a minimum of 2.5 times the diagonal length of indents, based on the recommendation in the ASTM E384–17 standard. Smaller indents allow for shorter distances between indents, thus improving the spatial resolution of microhardness line scans. However, there is a limitation as to how small indents can be with hardness measurements remaining accurate. A fixed error in measured diagonal lengths of indents results in exponentially increasing error as load and indent size is decreased (because of the inverse exponential relationship between diagonal length and Vickers hardness). According to [98], the measured Vickers hardness of materials can lose its load independence for forces under 100 gf. To

maximize spatial resolution while maintaining accuracy of hardness measurements, a force of 100 gf was used for microhardness measurements.

The largest indents had a diagonal length of approximately 40 µm, so 2.5 times that is 100 µm, which is the spacing used between indents in line scans. The distance between line scans perpendicular to their length was also 100 µm. Line scans were angled 15° from bonded interfaces to increase the spatial resolution of microhardness profiles to approximately 26 µm. Five microhardness line scans were taken for each diffusion couple and Ni-plated sample. For diffusion couples, this totaled 15 line scans per material combination and aging time because of diffusion couple triplication. In other words, each data point in microhardness plots for diffusion couples is an average of 15 measurements, and each data point in microhardness plots for Ni-plated samples is an average of 5 measurements. The indent pattern of five microhardness line scans on a diffusion couple is shown in Figure 3.9b.

3.6 Calculating diffusion coefficients

For diffusion couples, significant diffusion occurred during the 900 °C diffusion bonding process, making it necessary to take this diffusion into account in the calculation of effective 700 °C diffusion coefficients from thermal aging. It's unknown exactly when bonding occurs during diffusion bonding (i.e. t is unknown), so the combined term $(Dt)_{900\,^\circ\mathrm{C},bonding}$ in Equation 3.1 was calculated from EDS line scans of the non-thermally-aged (control) diffusion couples. The values for this combined term were then used in Equation 3.2 for calculating effective 700 °C diffusion coefficients.

$$C(x) = C_{clad} + \frac{C_{base} - C_{clad}}{2}\mathrm{erfc}\left(\frac{x}{2\sqrt{(Dt)_{900\,^\circ\mathrm{C},bonding}}}\right) \tag{3.1}$$

$$C(x, t_{700\,^\circ\mathrm{C}}) = C_{clad} + \frac{C_{base} - C_{clad}}{2}\mathrm{erfc}\left(\frac{x}{2\sqrt{(Dt)_{700\,^\circ\mathrm{C}} + (Dt)_{900\,^\circ\mathrm{C},bonding}}}\right) \tag{3.2}$$

For the Ni-plated samples, effective 700 °C diffusion coefficients were calculated by curve fitting Equation 2.13 to EDS line scan data. Equation 2.13 is the same as Equation 3.2 except that it doesn't have a $(Dt)_{900\,°\mathrm{C},bonding}$ term. The Ni-plated samples used for calculating these coefficients were not exposed to a diffusion bonding heat treatment before thermal aging; therefore, concentration profiles at the beginning of thermal aging were virtually square (Equation 2.13 for $t = 0$) due to electroplating being a low-temperature process. The lack of diffusion prior to thermal aging made measurement of Dt in control samples unnecessary.

Diffusion models were fit to measured concentration profiles using the least squares method. Python scripts (examples of which are included in Appendix D) were used for curve fitting, calculating average diffusion coefficients and their 95% confidence interval, and generating plots. Two variables were calculated for each curve fit: the diffusion coefficient (D) and a value to correct concentration profile data for it to be positionally aligned with the diffusion models at $x = 0$ (the interface). This removes the need to identify the location of interfaces based on microstructural features or with an inert marker added to initial interfaces. Bulk element concentrations in alloys, C_{base} and C_{clad}, were obtained from mill certificates of the purchased alloys (and are included in Table 3.1). The composition of Ni plating was assumed to be 100 wt% nickel.

It should be noted that the diffusion coefficients in Equation 3.1 and Equation 3.2 are effective diffusion coefficients, meaning that they take into account the effects of both grain boundary and lattice diffusion. The concept of effective diffusion coefficients is mathematically defined by Equation 2.17.

The diffusion models that were used assume both the presence of a single phase and concentration-independent diffusion. If it's known that diffusion coefficients are highly concentration-dependent, inaccuracy is avoided by using Boltzmann–Matano analysis to numerically calculate concentration-dependent interdiffusion coefficients from concentration profiles using the equations in [28, pp. 175–179] for multicomponent systems. The

extent to which error is induced from the assumptions of presence of a single phase and of concentration-independent diffusion can be evaluated by comparing the shape of measured concentration profiles with that of the diffusion model. The presence of additional phases, which may not be present in bulk alloys but may form during composite fabrication or thermal aging, can be evaluated by microstructural analysis.

3.7 Diffusion simulations with Thermo-Calc DICTRA

In order to extrapolate experimental diffusion results, diffusion was simulated with the diffusion module of Thermo-Calc software, called DICTRA. This software constructs full multi-component diffusivity matrices from built-in databases. Simulation results were curve fitted with experimentally measured concentration profiles in order to determine values of average grain size and activation energy ratio (E_a^{gb}/E_a^l) for extrapolating diffusion to an end of reactor lifetime. DICTRA has a built-in grain boundary model (based on Equation 2.17), for which lattice and grain boundary diffusion coefficients are assumed to have the same pre-exponential factor but different activation energies, and the default grain shape factor is one. Also, a grain boundary width of 0.5 nm was assumed for all simulations. Ideally, one would input an experimentally measured grain size average, but grain size varied considerably across the composites, and in DICTRA, there is no way to include a position dependent grain size contribution to diffusivity. Variation in both grain size and activation energy ratios in the grain boundary model has the equivalent effect on concentration profiles as varying thermal aging time—in other words, they affect how extended concentration profiles are, but not their shape. Therefore, it was possible to fix an average grain size in order for curve fitting to be reduced to the single variable of activation energy ratio. The drawback of this is that calculated activation energy ratios cannot be used with other grain sizes or for other materials or temperatures than those for which they were determined. Additional simulation conditions are listed below:

- Material phase: FCC (single phase)
- Thermodynamic database: Thermo-Calc's Steels/Fe-alloys v6.2 (TCFE6)
- Mobility database: Thermo-Calc's Alloys Mobility v2.7 (MOB2)
- Spatial resolution: 0.25–0.5 µm
- Only elements present as 0.5 wt% or more of the as-received alloys were included in the simulations in order to reduce simulation time. Test simulations were run to confirm that the effect of silicon, carbon, etc., is negligible.
- Initial element concentrations were the same as in Table 3.1, with the exception of nickel because it was set as the dependent component, meaning that the initial concentrations of nickel were those in Table 3.1 plus the summed concentration of elements that are less than 0.5 wt% of the as-received alloys.

In order to curve fit concentration profiles from simulations with those from experimental measurements, a Python script was used to average EDS line scan data in 1 or 2 µm bins and calculate the sum of the squared difference between the two datasets. Activation energy ratios were manually iterated for optimizing to the nearest 0.001 increment. Rather than calculating a single activation energy ratio from curve fitting with averaged EDS data, curve fits should be done for each EDS line scan followed by averaging of the calculated activation energy ratios. The reason why this was not done is that a large number of simulations would have been required and this would have been too time-consuming. In future work, this could be improved upon by calling Thermo-Calc DICTRA macros from a looping script, such as in Python, to automate the least square iteration process.

In some simulations for extrapolating diffusion results, a salt–cladding boundary condition of near-zero chromium concentration[2] was used to simulate corrosion in molten fluoride salts. This implies that corrosion was assumed to be fully diffusion-limited—a conservative

[2]More specifically, the boundary condition was chromium activity of 10^{-6}. Activity could not be fixed to exactly zero because doing so caused an error in DICTRA.

assumption. Aluminum and titanium, which are present in 800H, also leach into fluoride salts [99], and the same may be true for manganese (although the literature on leaching of manganese into fluoride salts is scarce). Boundary conditions of near-zero aluminum and titanium concentration should definitely be included in simulations, but unfortunately, doing so increased simulation time to the point of impracticality, so the near-zero concentration boundary condition was limited to chromium. Since initial concentrations of aluminum and titanium are low (see Table 3.1), the systematic error caused by this assumption is probably negligible.

Although corrosion rates in molten fluoride salts tend to be diffusion-limited[3], the extent to which this is the case depends on the chemical condition of the salt (redox potential and presence of impurities). An example of non-diffusion-limited molten fluoride salt corrosion for a Ni–20Cr alloy can be seen in [37, p. 143], where measured chromium concentration profiles tend towards $\sim$11 wt% rather than zero at the corrosion surface. These considerations suggest that a boundary condition of near-zero chromium concentration is not necessarily accurate. A more realistic boundary condition would be chromium flux that is a function of chromium activity in salt and at the surface of the corroded alloy (DICTRA has this functionality); this could be explored in future work in parallel with corrosion tests. However, near-zero surface chromium concentration is the worst case for molten fluoride salt corrosion, so taking this as a boundary condition is conservative and therefore useful.

Thermo-Calc DICTRA requires a substitutional element for the chromium that is simulated to leave at the boundary (leached into salt), and this was selected to be nickel. This is realistic only for corrosion induced by nickel fluoride impurities in salt with the reaction of Equation 2.7. Once impurities are depleted, either pores would form or the thickness of material would decrease as chromium is leached into salt. As mentioned in Section 2.1,

[3]For example, the corrosion observed in experiments during and after the operation of the MSRE was reported to be diffusion-limited [41], meaning that diffusion of chromium from within alloys to their interface with salt was slower than the chemical reactions forming chromium fluoride and the transport of chromium fluoride away from corrosion surfaces.

the impurities in molten fluoride salts can be mostly reacted early during reactor operation, making the dominating corrosion mechanism switch from impurity-driven corrosion to non-substitutional corrosion mechanisms, such as intrinsic corrosion, thermal-gradient-driven corrosion, or dissimilar material corrosion. Therefore, the assumption that all leached chromium is substituted for nickel—in other words, that impurity-driven corrosion is the only corrosion mechanism and only with nickel fluoride—is highly likely to be inaccurate, but the effect of this assumption on simulation results may be small.

Chapter 4

Results

In this chapter, the results for each test are summarized and are organized by material and type of analysis. The micrographs and microanalysis data that are included were chosen for communicating observed material properties while being kept to a minimum for the sake of brevity. Uncertainties are given as 95% confidence intervals throughout this thesis.

4.1 Initial testing

4.1.1 Optical micrographs of as-received alloys

Micrographs of 800H, SS316L, and Hastelloy N alloys as they were received are shown in Figure 4.1. There is notable difference in grain size and the amount of twinning between the alloys. The circular dots in the micrograph of Hastelloy N are massive molybdenum carbides; this is typical for Hastelloy N.

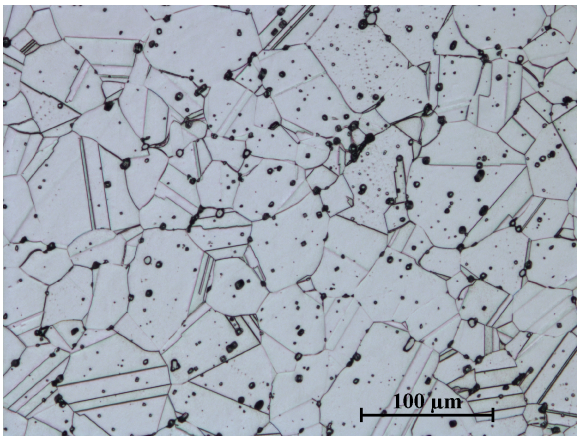

(a) Hastelloy N, 200x.

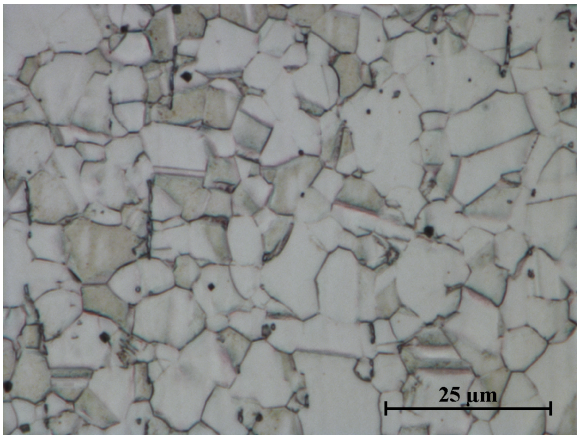

(b) SS316L, 1000x.

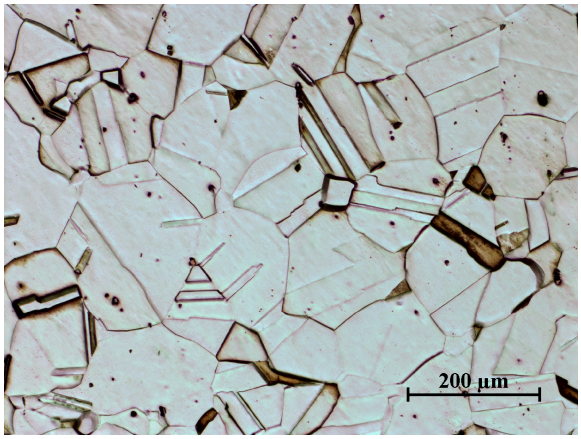

(c) 800H, 100x.

Figure 4.1: Optical micrographs of as-received alloys etched in aqua regia. Note the difference in magnification.

4.1.2 Microhardness profiles of the as-received alloys

Microhardness profiles of the as-received alloys are included later in this thesis along with microhardness profiles of the diffusion bonded and thermally aged composites. The microhardness values vary slightly across the thickness of the as-received alloys even though they were supplied in the annealed condition.

4.1.3 Profilometry of bonding surfaces

Surface profile maps are shown in Figure 4.2 for 800H, SS316L, and Hastelloy N after grinding and polishing (up to 1 µm diamond polish) in preparation for diffusion bonding. Surface roughness increases the tendency for voids to be present at diffusion bonded interfaces; at the same time, some roughness is desired because deformation of surface asperities during diffusion bonding causes surface oxide films to be broken and it causes interfacial mixing.

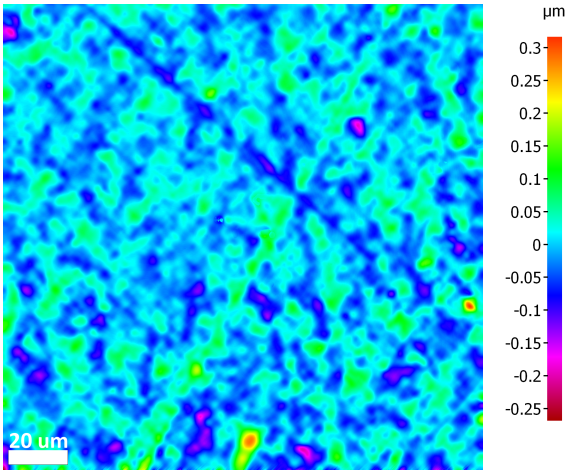

(a) Hastelloy N, average height: 0.032 µm.

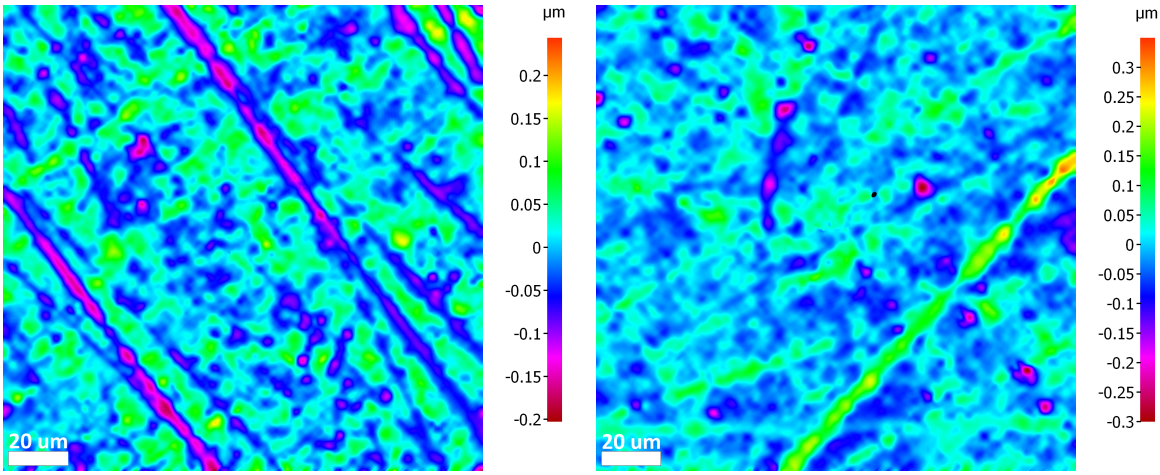

(b) 800H, average height: 0.036 µm.

(c) SS316L, average height: 0.037 µm.

Figure 4.2: Profiles of polished bonding surfaces, 2000x. The average height values were calculated based on the ISO 4287 standard.

4.2 Microstructure in 800H/Hastelloy N and SS316L/Hastelloy N diffusion couples

Optical micrographs of the interfaces of etched 800H/Hastelloy N diffusion couples are included in Figure 4.3, showing that the bonded interfaces are distinct with little grain overlap. This is undesirable as it suggests the possibility of incomplete metallurgical bonding during the diffusion bonding process. Another sign of poor bonding is the porosity shown in Figure 4.4. It's possible that a better quality bond with grain overlap could be obtained by increasing the diffusion bonding temperature above 900 °C, but unfortunately, 900 °C is the upper limit for the diffusion bonding equipment used in this study.

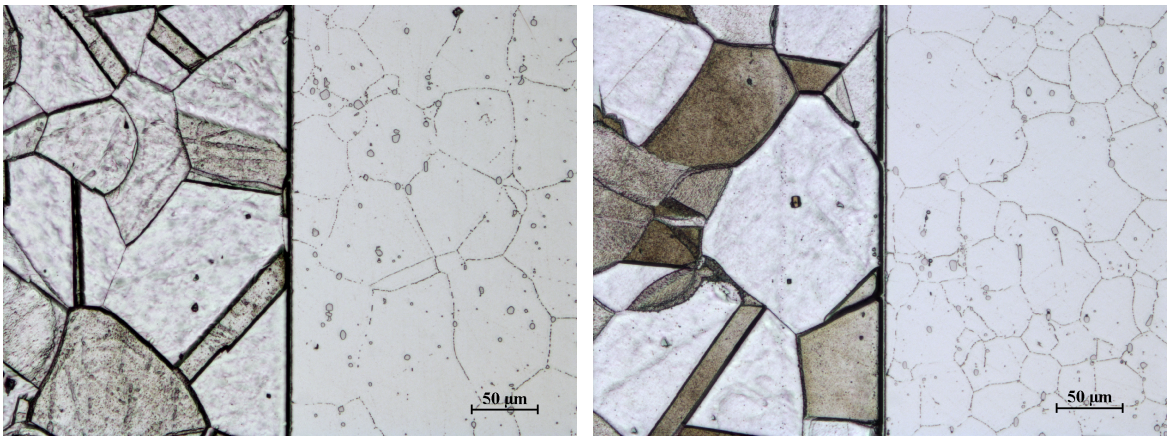

(a) Non-thermally-aged. (b) 1460-hour-aged.

Figure 4.3: Cross-sectional optical micrographs of the interface of 800H/Hastelloy N diffusion couples etched in aqua regia, 200x.

Microhardness profiles of as-received, diffusion bonded, and thermally aged 800H/ Hastelloy N are shown in Figure 4.5. From these microhardness profiles, it is seen that (1) there was very little change in hardness in 800H during diffusion bonding and thermal aging, (2) there was a decrease in the hardness of Hastelloy N during diffusion bonding and no change during thermal aging, and (3) there is no interfacial embrittlement.

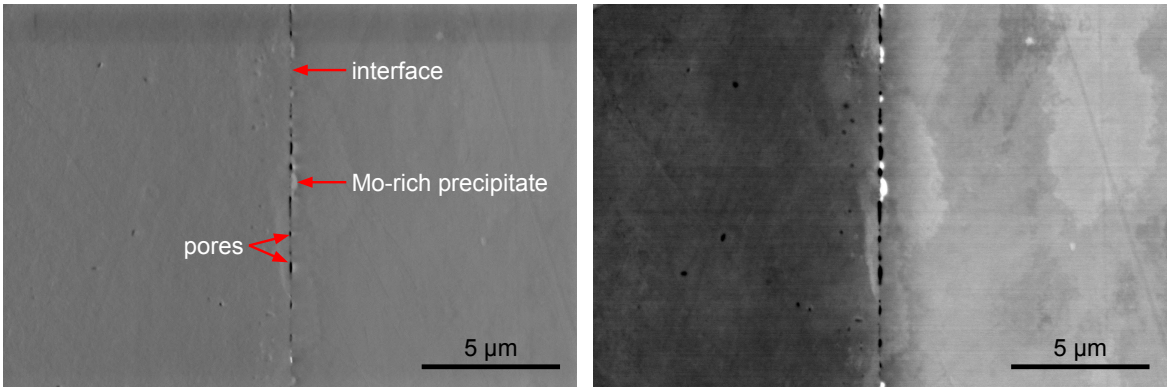

(a) SEM-SE image. (b) SEM-BSE image.

Figure 4.4: Cross-sectional SEM images of the interface of non-thermally-aged 800H/ Hastelloy N, 10 000x.

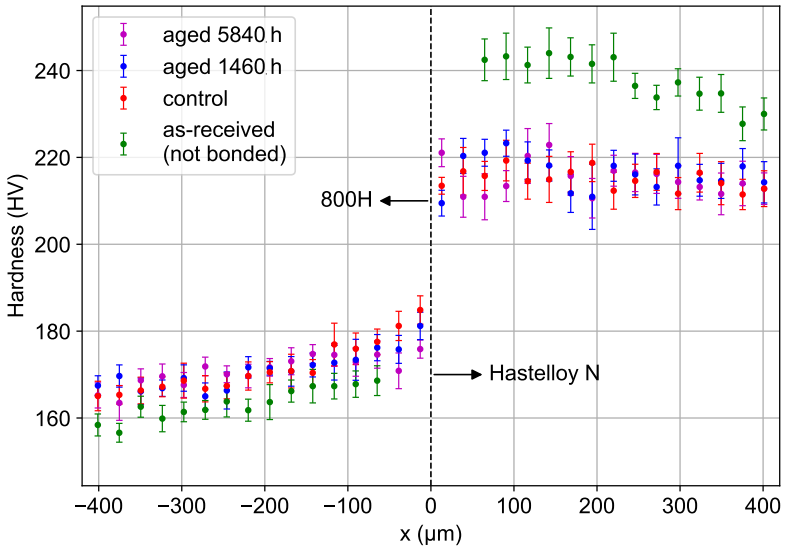

Figure 4.5: Microhardness profiles of as-received alloys and 800H/Hastelloy N diffusion couples, with a dashed line marking the interface.

The grains in Hastelloy N grew during diffusion bonding, causing the measured decrease in hardness. With the planimetric method described in the ASTM E112–13 standard[1], the average grain size of as-received Hastelloy N was measured to be 26 µm and the average grain size of bulk Hastelloy N bonded to 800H was measured to be 34 µm.

EDS maps of the interface of non-thermally-aged and 5840-hour-aged 800H/Hastelloy N are shown in Figures 4.6 and 4.7, respectively. The massive molybdenum carbide and fine intergranular carbides on the right-hand side of the EDS maps in Figure 4.7 are outside of the diffusion zone and serve as reference precipitates normally present in Hastelloy N. The EDS maps for thermally aged 800H/Hastelloy N show molybdenum, silicon, and boron enrichment and slight carbon enrichment[2] at the interface. Relatively little of this is observed for the non-thermally-aged material. These results suggest that a molybdenum-rich phase, possibly molybdenum borocarbide, started forming at interfaces during diffusion bonding and grew during thermal aging. For the concentrations of iron, nickel, molybdenum, and chromium at the interface of 800H/Hastelloy N determined from EDS line scans (shown later), the equilibrium phase was calculated with Thermo-Calc to be a combination of FCC and P phase. P phase is slightly high in chromium relative to the FCC phase, and this is inconsistent with the chromium depletion at the interface in the chromium EDS map in Figure 4.7.

Optical micrographs of the interfaces of etched SS316L/Hastelloy N are included in Figure 4.8, showing that the interfaces are distinct with little grain overlap, just as in 800H/ Hastelloy N. Precipitation of intergranular carbides and intermetallics in SS316L during thermal aging is seen as coarsening of the etched grain boundaries. There was less porosity at the interface of diffusion couples of Hastelloy N with SS316L (Figure 4.9) compared to those with 800H (Figure 4.4). This is consistent with the fact that 800H has more creep resistance

[1]The guidelines in the ASTM E112–13 standard were followed except for their etching procedure recommendations because Hastelloy N isn't included in the recommendations. Aqua regia etchant was used based on examples in the literature.

[2]Boron and carbon Kα peaks overlapped to some extent (X-ray energies are 0.183 kV for boron and 0.277 kV for carbon), possibly affecting the accuracy of the boron and carbon EDS maps.

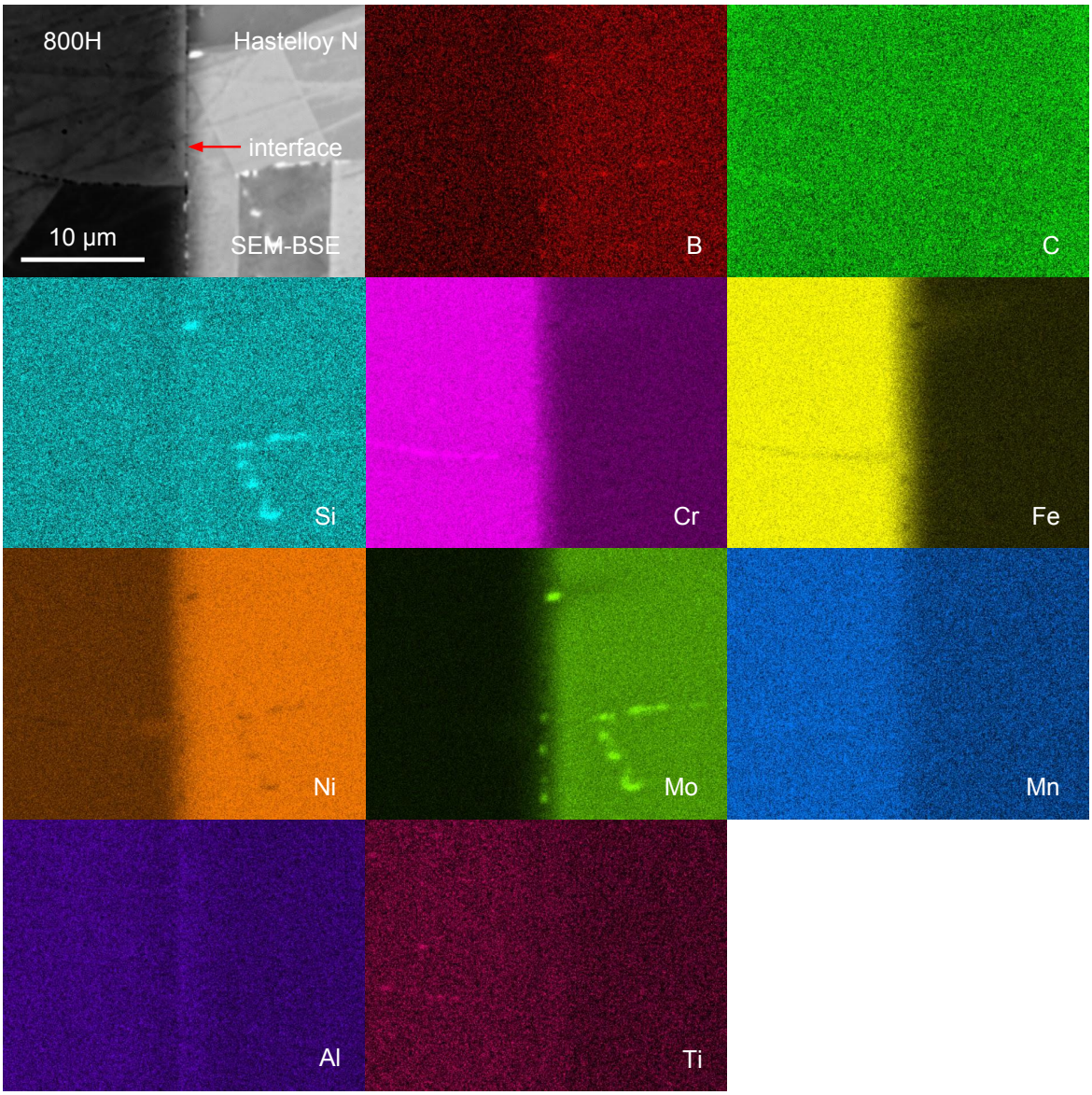

Figure 4.6: Cross-sectional EDS maps of the interface of non-thermally-aged 800H/ Hastelloy N, 4500x.

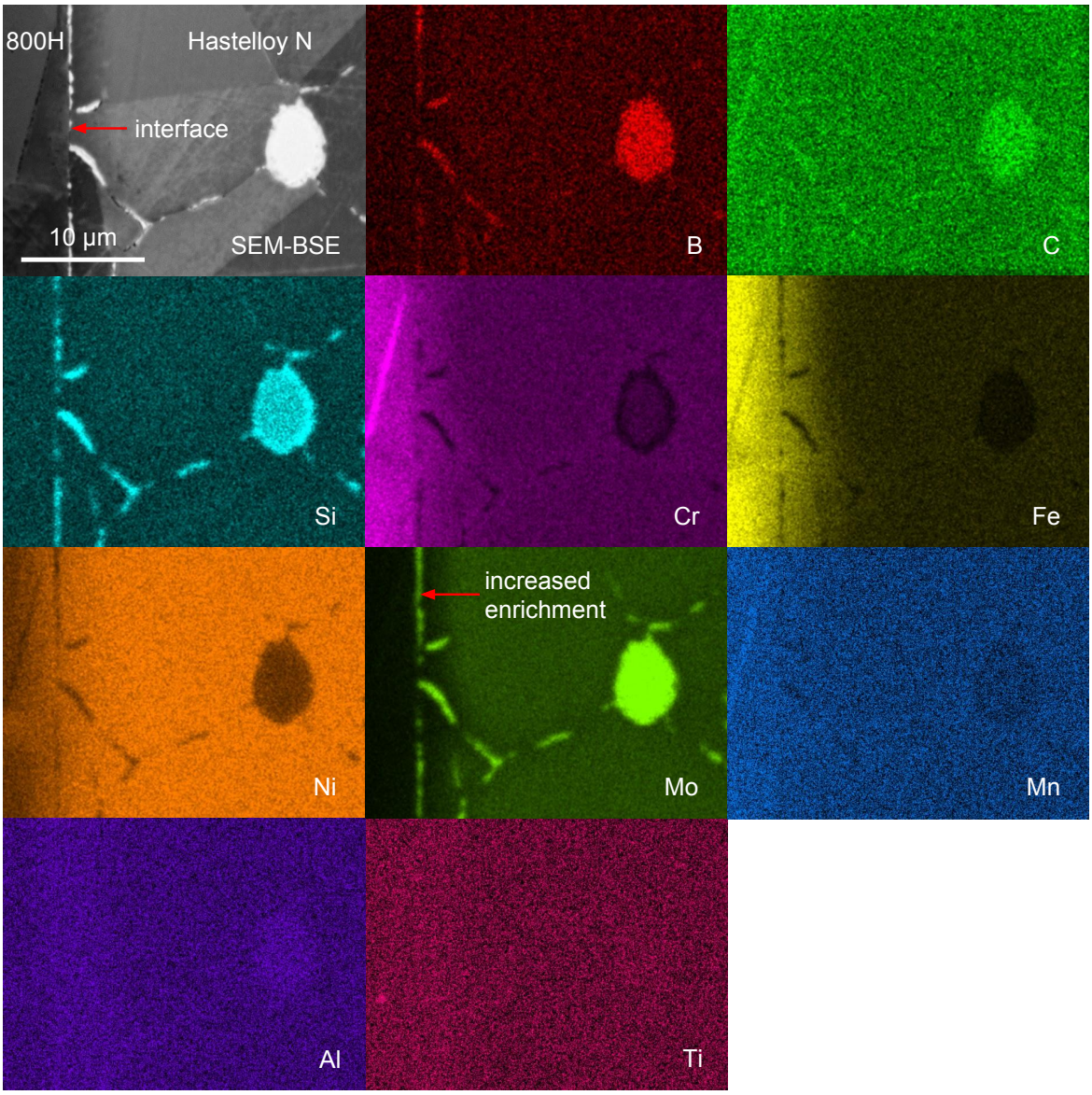

Figure 4.7: Cross-sectional EDS maps of the interface of 5840-hour-aged 800H/Hastelloy N, 4500x.

than SS316L at 700 °C. Furthermore, grain growth occurred throughout the SS316L layer during diffusion bonding. The occurrence of grain growth is made evident by comparing the grain size of bonded SS316L in Figure 4.8 with that of as-received SS316L in Figure 4.1b.

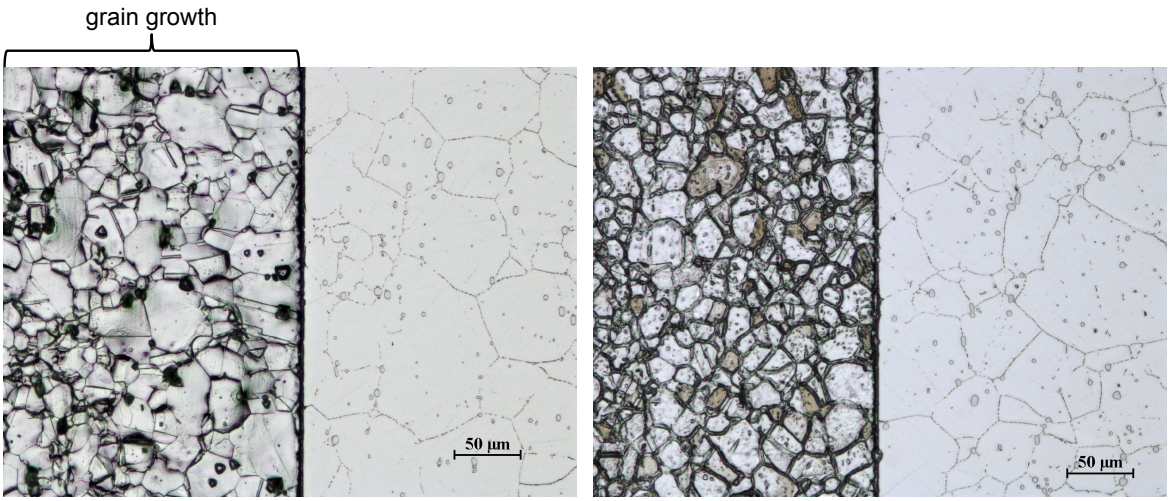

(a) Non-thermally-aged. (b) 1460-hour-aged.

Figure 4.8: Optical micrographs of SS316L/Hastelloy N diffusion couples etched in aqua regia, 200x.

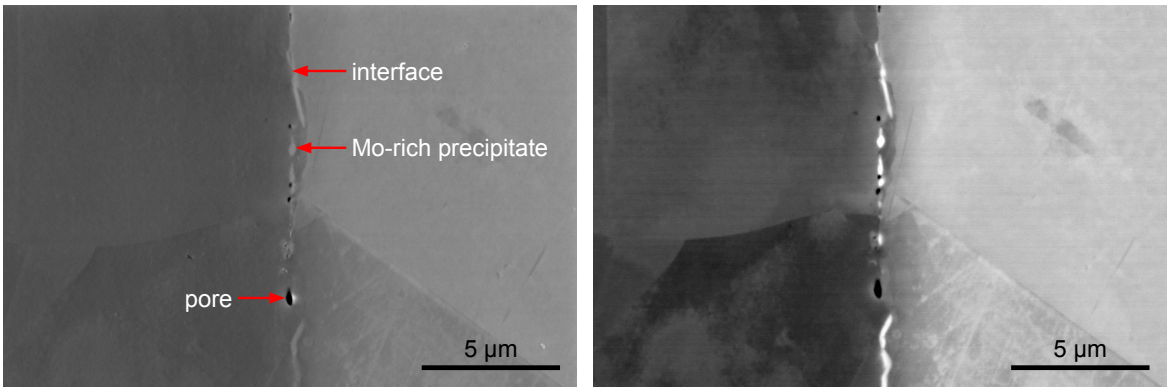

(a) SEM-SE image. (b) SEM-BSE image.

Figure 4.9: Cross-sectional SEM images of the interface of non-thermally-aged SS316L/ Hastelloy N, 10000x.

Microhardness profiles of as-received, diffusion bonded, and thermally aged SS316L/ Hastelloy N are shown in Figure 4.10. From these microhardness profiles, it is seen that (1) the hardness of SS316L decreased during diffusion bonding and gradually increased

during thermal aging, (2) the hardness of Hastelloy N decreased during diffusion bonding and did not change during thermal aging, and (3) there was no interfacial embrittlement. The decrease in hardness of SS316L during diffusion bonding is due to grain growth, and the increase in hardness of SS316L during thermal aging is due to precipitation of carbides and intermetallics primarily at grain boundaries, which is expected for exposure of this alloy to 700 °C based on the TTT diagram in Figure 2.17 and the data in [100, Tab. 1] for thermal aging of SS316 at 649 °C. Furthermore, the measured decrease in hardness in bulk Hastelloy N bonded to 800H was caused by grain growth, just as for Hastelloy N bonded to SS316L.

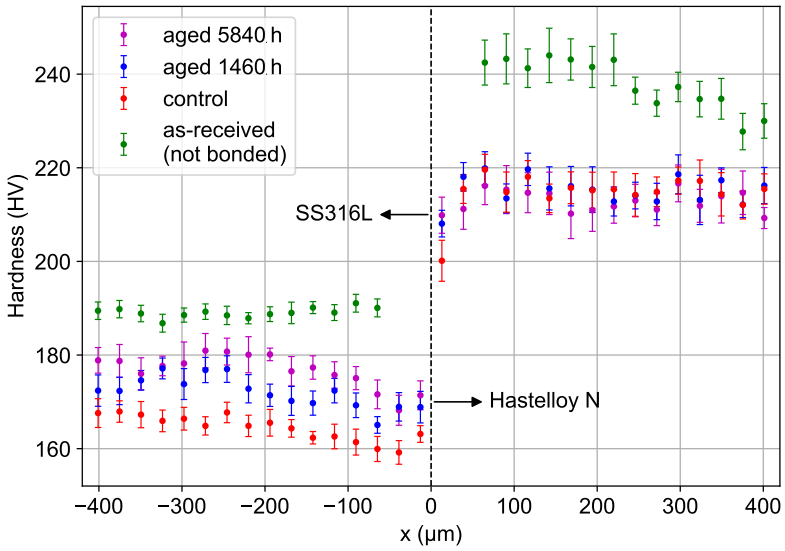

Figure 4.10: Microhardness profiles of as-received alloys and SS316L/Hastelloy N diffusion couples, with a dashed line marking the interface.

EDS maps of the interface of non-thermally-aged and 5840-hour-aged SS316L/Hastelloy N are shown in Figures 4.11 and 4.12, respectively. These EDS maps show molybdenum, silicon, and boron enrichment and slight carbon enrichment at the interface primarily for thermally aged SS316L/Hastelloy N, leading to the same conclusion as for 800H/Hastelloy N that a molybdenum-rich phase precipitated at interfaces primarily during thermal aging. For the concentrations of iron, nickel, molybdenum, manganese, and chromium at the interface

of 800H/Hastelloy N determined from EDS line scans (shown later), the equilibrium phase was calculated with Thermo-Calc to be a combination of FCC, high sigma, and mu phase. Relative to the FCC phase, the high sigma phase is higher in chromium, which is inconsistent with the lack of chromium enrichment at the interface in the chromium EDS map in Figure 4.12. Relative to the FCC phase, the mu phase is slightly lower in iron, which is inconsistent with the iron depletion at the interface in the iron EDS map in Figure 4.12.

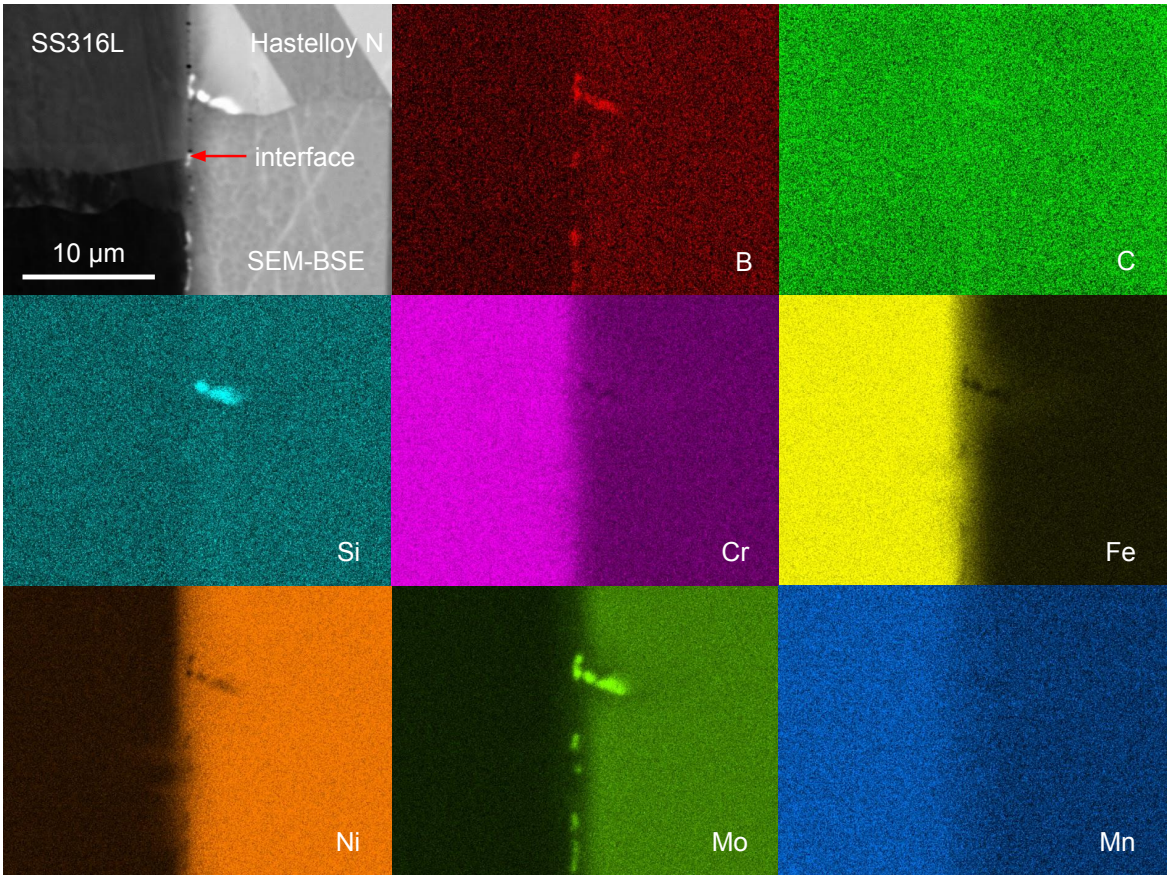

Figure 4.11: Cross-sectional EDS maps of the interface of non-thermally-aged SS316L/ Hastelloy N, 4500x.

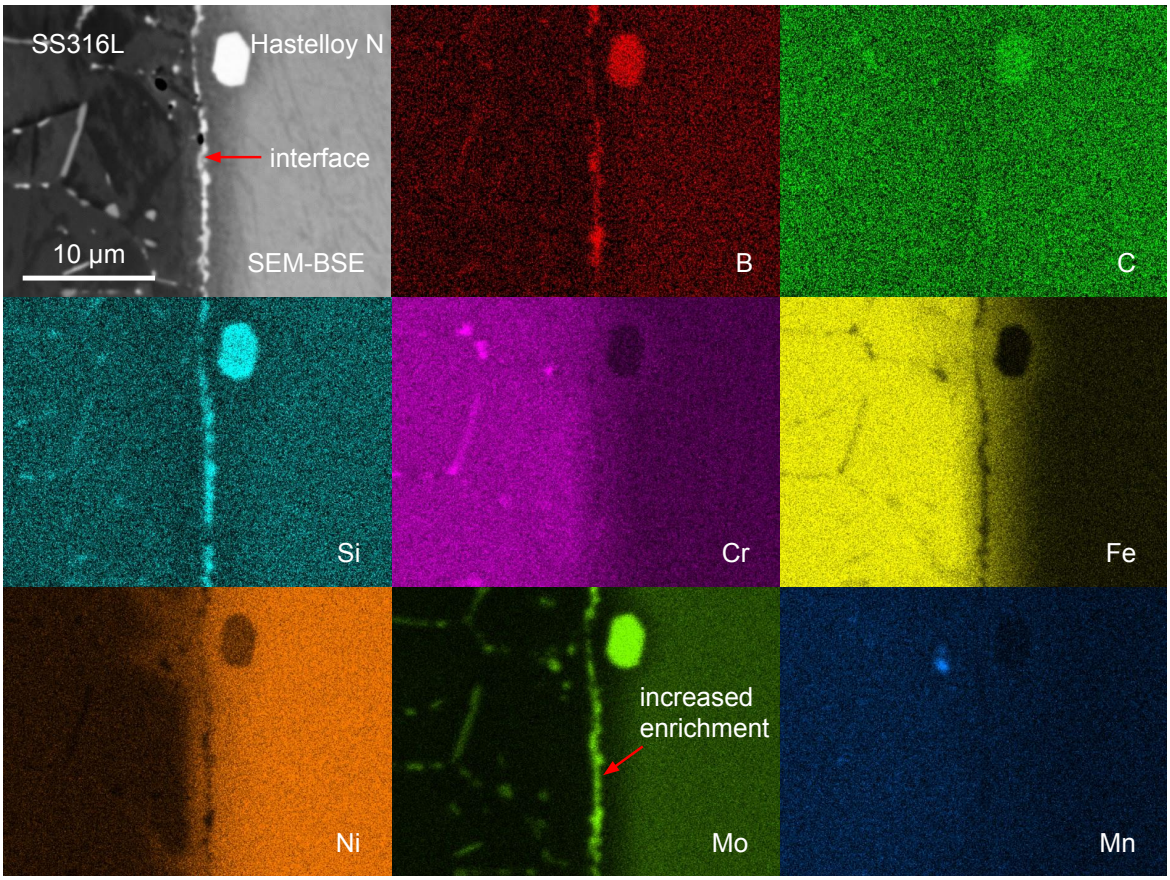

Figure 4.12: Cross-sectional EDS maps of the interface of 5840-hour-aged SS316L/ Hastelloy N, 4500x.

4.3 Diffusion in 800H/Hastelloy N and SS316L/Hastelloy N diffusion couples

This section includes EDS line scan data and curve fit results for non-thermally-aged and 1460-hour-aged diffusion couples. EDS line scan data for 5840-hour-aged diffusion couples are not included because they are qualitatively similar to the data for 1460-hour-aged diffusion couples (evidence for this is provided in Figure A.6). The diffusion resistance of each material combination is summarized at the end of this section by a table of calculated chromium diffusion coefficients. Calculated diffusion coefficients for elements other than chromium are included in Appendix A. The focus here is on chromium because its diffusion is accelerated by

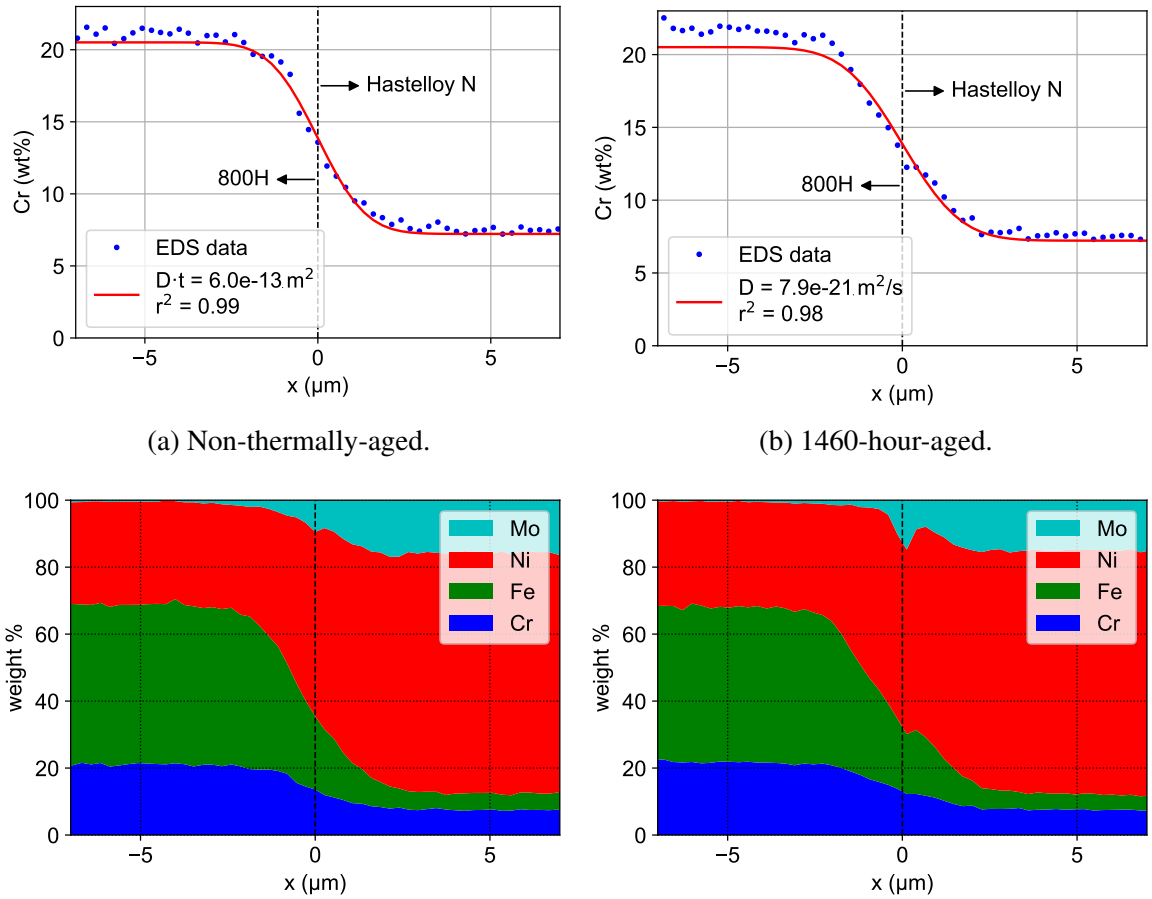

(a) Non-thermally-aged.

(b) 1460-hour-aged.

(c) Non-thermally-aged.

(d) 1460-hour-aged.

Figure 4.13: 800H/Hastelloy N diffusion couples: chromium EDS line scan data and curve fit (top) and stacked area plots for elements present as more than 1 wt% of either alloy (bottom).

leaching into salt (iron can also be selectively attacked but to a lesser extent than chromium). It's entirely possible, however, that the diffusion zone in structural alloys would be determined by other elements than chromium.

Typical EDS line scan results for non-thermally-aged and 1460-hour-aged 800H/Hastelloy N diffusion couples are shown in Figure 4.13. Chromium concentration profiles matched the diffusion models of Equations 3.1 and 3.2 very well. Interfacial molybdenum enrichment is seen in the stacked area plots (Figures 4.13c and 4.13d), and this is consistent with what is reported in Section 4.2. More interfacial molybdenum enrichment was consistently observed for line scans of the thermally aged diffusion couples.

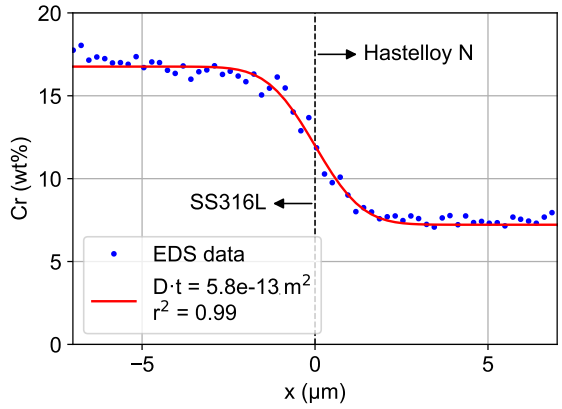

(a) Non-thermally-aged.

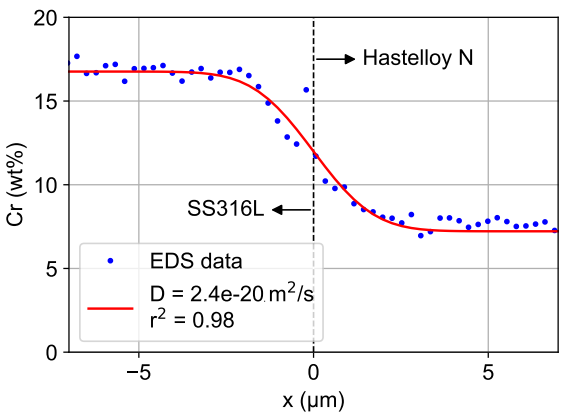

(b) 1460-hour-aged.

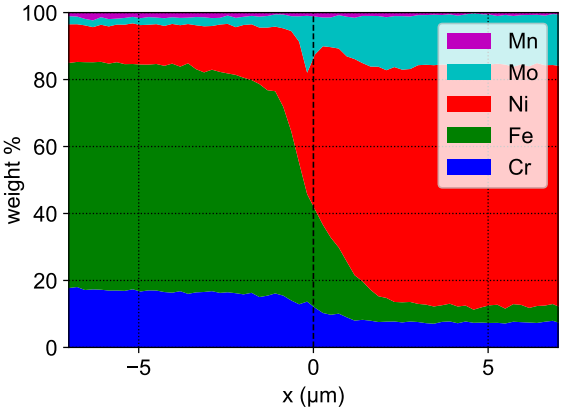

(c) Non-thermally-aged.

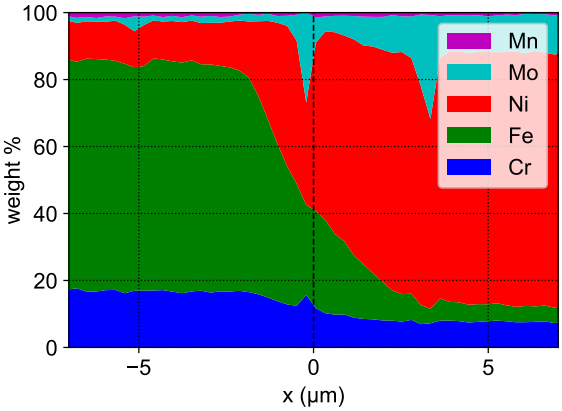

(d) 1460-hour-aged.

Figure 4.14: SS316L/Hastelloy N diffusion couples: chromium EDS line scan data and curve fit (top) and stacked area plots for elements present as more than 1 wt% of either alloy (bottom).

Results of EDS line scan analysis for SS316L/Hastelloy N are shown in Figure 4.14. The qualitative observations for SS316L/Hastelloy N are the same as those for 800H/Hastelloy N: SS316L/Hastelloy N exhibited diffusion behavior that matches the diffusion models of Equations 3.1 and 3.2 very well, and interfacial molybdenum enrichment, with greater amounts in the thermally aged material, is seen in the stacked area plots.

Average calculated chromium diffusion coefficients for the 800H/Hastelloy N and SS316L/Hastelloy N diffusion couples are shown in Table 4.1. The same table is included in Appendix A for each element of iron, nickel, and molybdenum.

Caution is warranted when using the calculated diffusion coefficients in Table 4.1. They were calculated with the assumptions of type A diffusion kinetic regime, phase homogeneity, and concentration-independence. The extent to which these assumptions are valid is discussed in Chapter 5.

Table 4.1: Chromium diffusion coefficients D_{Cr} for diffusion couples thermally aged at 700 °C for 1460 h and 5840 h, and $D_{Cr}t$ term for 2 h bonding at 900 °C, calculated from EDS line scan data. Uncertainties are 95% confidence intervals, and the values in the parentheses are average r-squared values from the curve fits.

Material combination	$D_{Cr}t$ [m^2] (bonding)	D_{Cr} [$m^2\,s^{-1}$] (700 °C)	
		1460 h	5840 h
800H/Hastelloy N	7.9E-13±1.3E-13 (0.99)	1.4E-20±2.8E-20 (0.96)	5.9E-20±1.0E-20 (0.97)
SS316L/Hastelloy N	6.9E-13±1.2E-13 (0.99)	1.9E-20±2.5E-20 (0.97)	4.8E-20±1.3E-20 (0.97)

The 95% confidence intervals mean that there is 95% certainty that the mean of each group of 27 calculated diffusion coefficients is between the lower and upper bounds of the confidence intervals. However, this assumes that calculated diffusion coefficients are randomly distributed. In other words, the 95% confidence intervals say nothing about systematic error. For example, if actual furnace temperature was 750 °C instead of 700 °C, the resulting error would not be reflected in 95% confidence intervals.

4.4 Microstructure in 800H/Ni plating and SS316L/Ni plating

Grain size and shape distributions at the interface of Ni-plated samples are shown in EBSD maps in Figure 4.15. The as-received Ni plating on 800H (Figure 4.15c) has very small grains

and grains that are elongated normal to the interface. Similar grain size and shape is expected for Ni plating on 800H, although this was not empirically confirmed. Sub-micron grain size is typical for Ni plating, and the elongated grains in the as-received Ni plating are consistent with what is shown in the EBSD map in [101, Fig. 4a] for Ni sulfamate plating with no organic additives and similar current density to what was used in this study. For thermally aged 800H/Ni plating (Figure 4.15a) and thermally aged SS316L/Ni plating (Figure 4.15b), the large grains in the bulk Ni plating are a result of significant grain growth.

For thermally aged SS316L/Ni plating, the location of the original interface was identified from presence of small pores and is indicated in Figure 4.15b with a dashed line. However, for thermally aged 800H/Ni plating, the exact location of the original interface could not be identified, so its general location is indicated in Figure 4.15a with two curved lines. The location of original interfaces matters because it determines whether microstructural features formed in the structural alloy or in the Ni plating.

A layer of small grains formed at the interface of thermally aged 800H/Ni plating (Figure 4.15a). The edge of this layer of small grains is straighter on the Ni plating side than on the 800H side, which suggests that these small grains are in the 800H. This would mean that the small grains are a result of recrystallization in the 800H rather than being grains of Ni plating that didn't grow as much as those in bulk Ni plating. In future research, an inert marker (e.g. platinum) could be deposited on 800H before electroplating so that the interface of thermally aged 800H/Ni plating can be located with more certainty. Furthermore, the layer of small grains in 800H/Ni plating resembles the layer of recrystallized grains that was observed at the interface of 800H/Ni 200 diffusion couples (see Section B.2). In contrast with the possible recrystallization of grains in the 800H, the grains near the interface in SS316L are larger than the grains in the bulk SS316L, so the grains near the interface in SS316L are the result of grain growth rather than recrystallization.

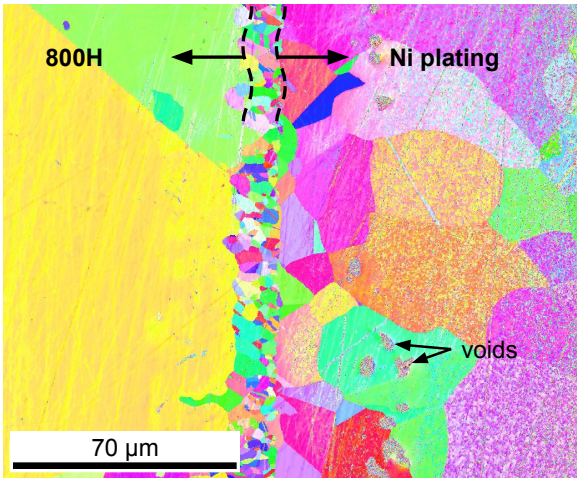

(a) 3855-hour-aged 800H/Ni plating, 1000x.

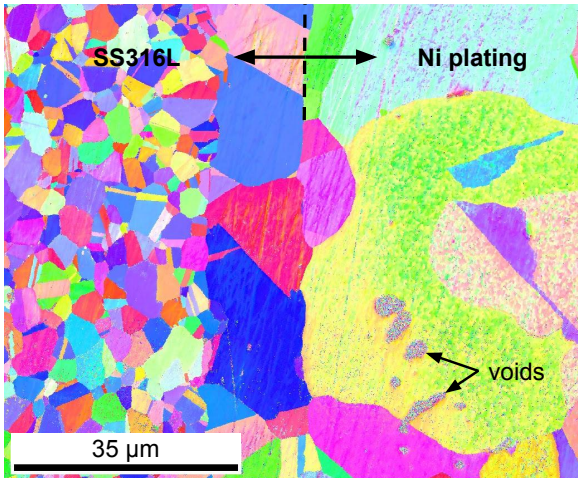

(b) 3855-hour-aged SS316L/Ni plating, 2000x.

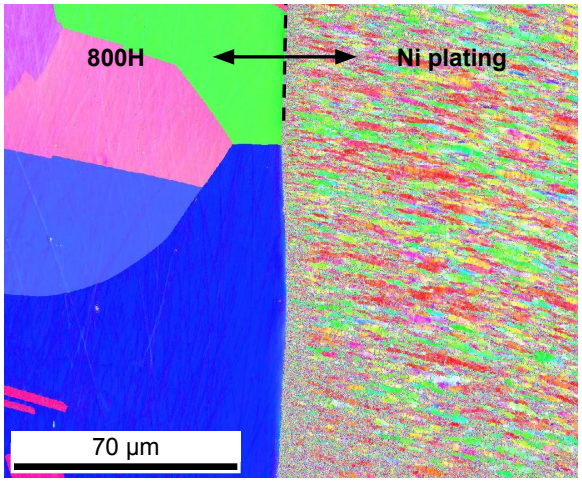

(c) As-received 800H/Ni plating, 1000x.

Figure 4.15: Cross-sectional EBSD maps of the interface of Ni-plated samples. The interfaces are demarcated with dashed lines. There was drift during data collection, causing these maps to be slightly curved (clearly visible from the curved interface in the map of as-received 800H/Ni plating).

Microhardness profiles for 800H/Ni plating and SS316L/Ni plating are shown in Figure 4.16. The most important observation from these results is that there is no interfacial embrittlement from thermal aging in either Ni-plated 800H or Ni-plated SS316L. Two indents were made in as-received Ni plating, but only a single indent was made in thermally aged Ni plating because of the difference in size of the indents and the requirement for indents to be a minimum distance from edges in order for the measured hardness to be accurate. The high hardness of the as-received Ni plating is due to this material's very small grain size and possibly also due to internal stress. The characteristic of small grain size and the distinct interface are lost during thermal aging, as shown in the EBSD maps in Figure 4.15. Typical hardness for Ni sulfamate plating is around 200–350 HV [102], so the measured hardness of the as-received Ni plating is as expected. However, there is a $\sim$50 HV difference in measured hardness of Ni plating with 800H versus SS316L substrates, and the cause of this difference is unknown.

For reducing the risk of mechanical failure, the hardness of claddings should be less than the hardness of structural alloy substrates (i.e. claddings should be ductile), so the high hardness in as-received Ni plating is undesirable. However, Ni-plated components could be heat treated prior to their use in reactors in order to induce grain growth (and interfacial mixing) in a low-stress environment.

The small grains at the interface of thermally aged 800H/Ni plating may have caused the hardness of the interface to be higher than if there were no small grains. This possible effect is apparent by comparing the hardness of the interface relative to the bulk structural alloys for thermally aged 800H/Ni plating and SS316L/Ni plating (Figures 4.16a and 4.16b). However, the measured hardness at the interface of thermally aged 800H/Ni plating is less than the measured hardness of bulk 800H, so the possible embrittling effect of the layer small grains is not a concern.

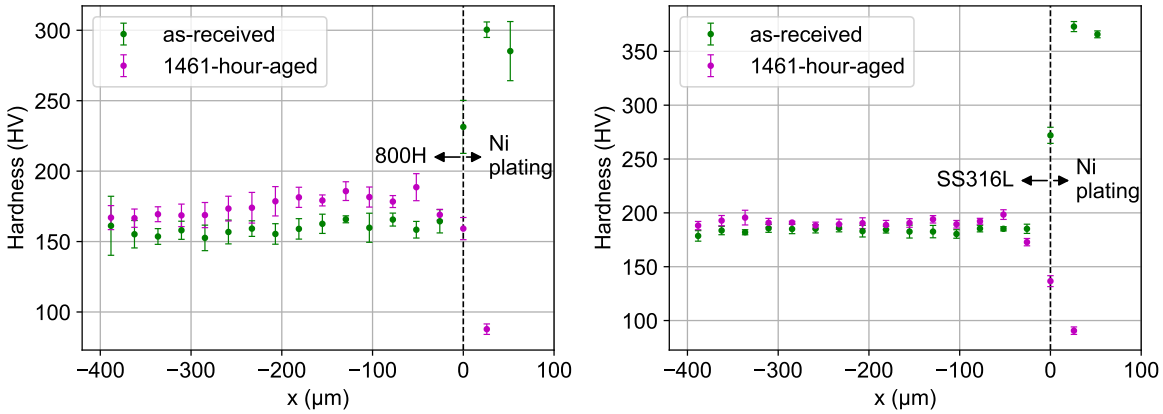

(a) 800H/Ni plating.

(b) SS316L/Ni plating.

Figure 4.16: Microhardness profiles for as-received and 1461-hour-aged Ni-plated samples.

During thermal aging, 5–15 μm voids formed in Ni plating 20–30 μm from interfaces with both 800H and SS316L substrates. The distribution of these voids in 3855-hour-aged SS316L/Ni plating is shown in Figure 4.17a, and a close-up view in SE imaging mode is shown in Figure 4.17b, with the bright edges indicating that the features are voids and not inclusions. These voids are visible in the EBSD maps in Figure 4.15. Voids were also present in 1460-hour-aged Ni-plated samples, and they were not present in the as-received Ni plating. These voids may have had an effect on the measured hardness of thermally aged Ni plating in Figure 4.16. Furthermore, relatively small porosity formed directly at the interface of SS316L/Ni plating (visible in Figure 4.17a), but not at the interface of 800H/Ni plating.

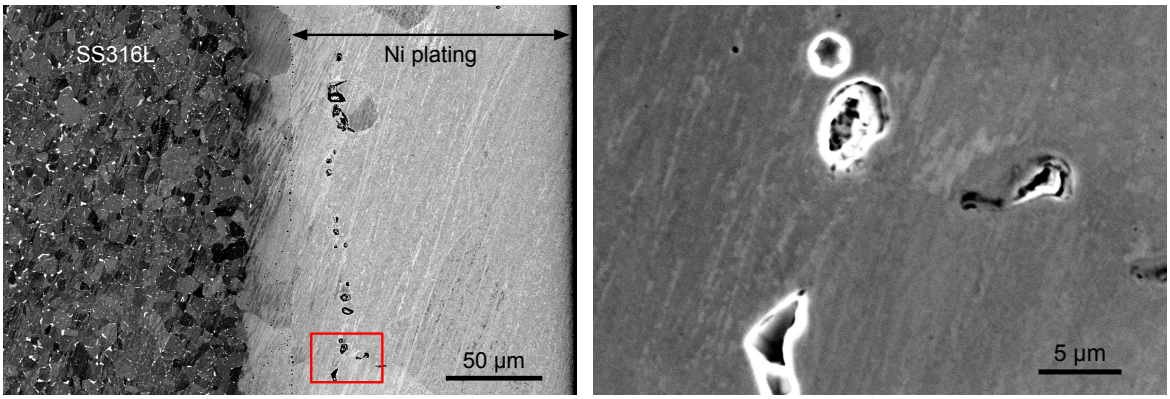

(a) SEM-BSE image, 430x.

(b) SEM-SE image of voids at the location highlighted in (a), 3700x.

Figure 4.17: SEM micrographs of 3855-hour-aged SS316L/Ni plating. Note that the image on the left was taken in BSE mode and the image on the right was taken in SE mode.

4.5 Diffusion in 800H/Ni plating and SS316L/Ni plating

Typical EDS line scan results for 3855-hour-aged 800H/Ni plating and SS316L/Ni plating are shown in Figures 4.18 and 4.19, respectively. For the line scan of 800H/Ni plating, a nickel-rich region formed along a grain boundary in 800H. The slope of concentration profiles decreased for 10–30 µm at the interface of 800H/Ni plating; this is consistent with the observed grain size distribution shown in Figure 4.15a and the fact that diffusion is faster in smaller-grained material. The change in slope caused the curve fits for 800H/Ni plating to be worse than for SS316L/Ni plating.

Average calculated chromium diffusion coefficients for 800H/Ni plating and SS316L/Ni plating are shown in Table 4.2. The same table for each element of iron and nickel is included in Appendix A. By comparing Table 4.2 with Table 4.1, it is seen that diffusion of chromium in the diffusion couples with Hastelloy N is far slower than in the Ni-plated samples, and in both cases, there is relatively little difference between structural alloys.

Table 4.2: Chromium diffusion coefficients D_{Cr} for Ni-plated samples aged at 700 °C for 3855 h, calculated from EDS line scan data. Uncertainties are 95% confidence intervals, and the values in the parentheses are average r-squared values from the curve fits.

Material combination	D_{Cr} [$m^2 s^{-1}$] (700 °C)	
	1461 h	3855 h
800H/Ni plating	4.2E-17±9.5E-18 (0.94)	1.6E-17±3.4E-18 (0.95)
SS316L/Ni plating	2.3E-17±3.2E-18 (0.97)	1.5E-17±2.5E-18 (0.96)

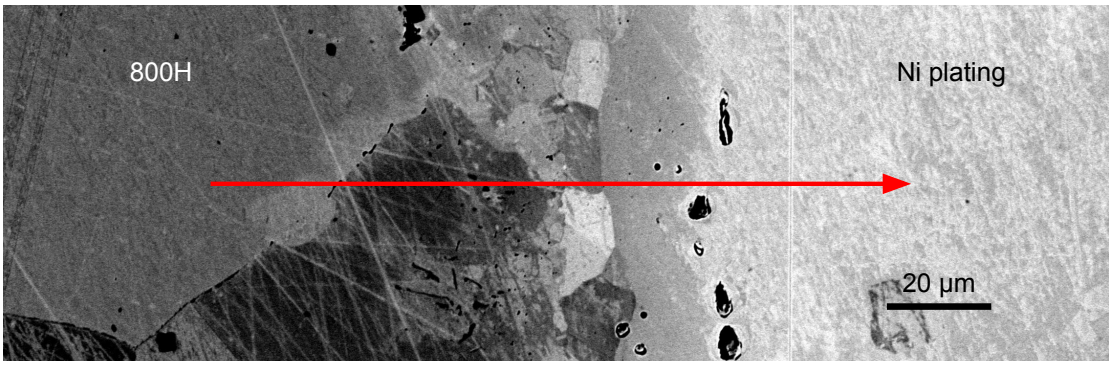

(a) SEM-BSE image of EDS line scan path.

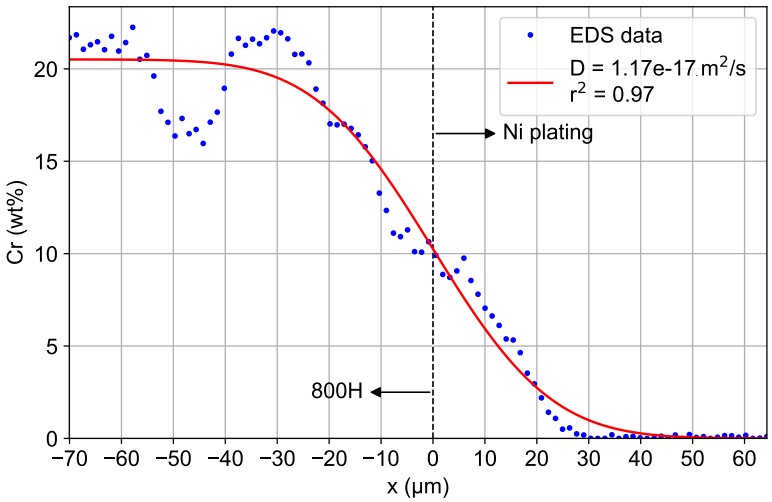

(b) Curve fit of chromium EDS data.

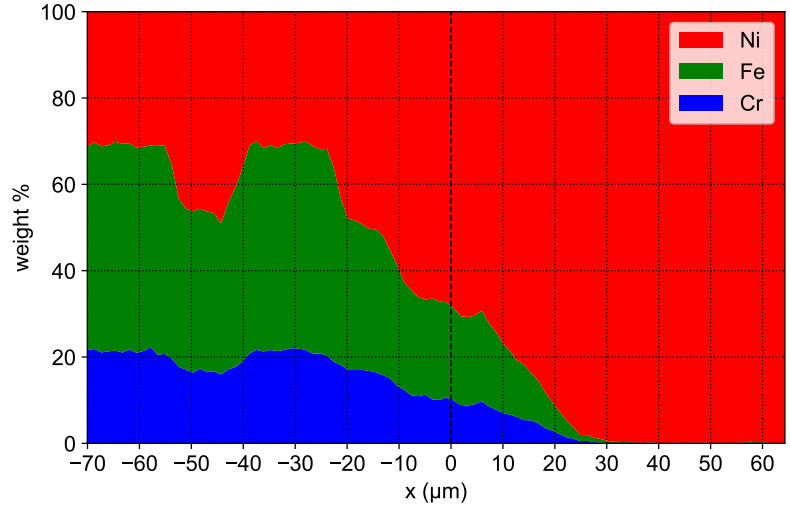

(c) Stacked area plot of major elements (>1wt%).

Figure 4.18: EDS line scan data and curve fit for 3855-hour-aged 800H/Ni plating.

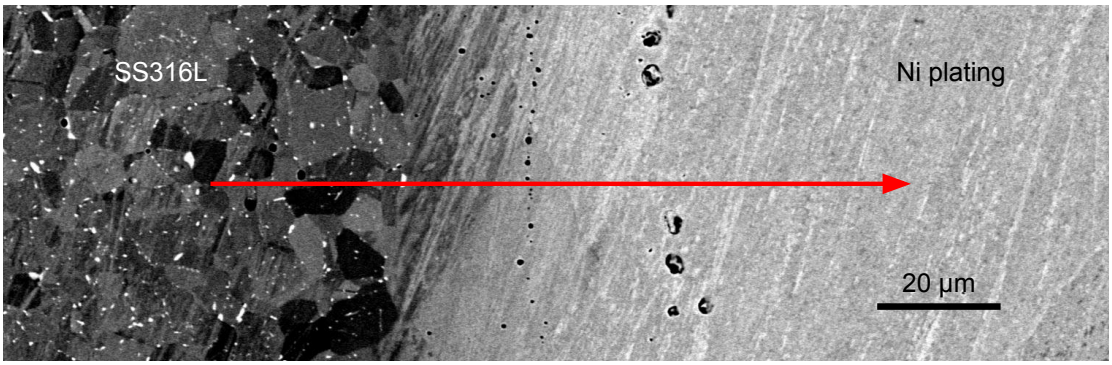

(a) SEM-BSE image of EDS line scan path.

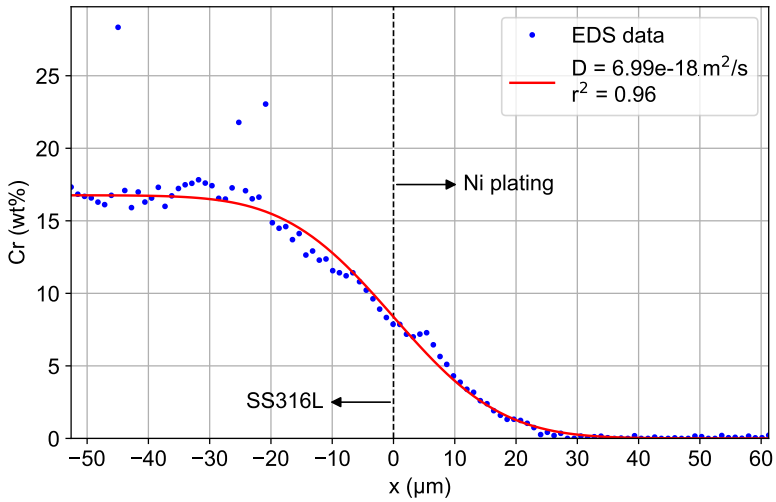

(b) Curve fit of chromium EDS data.

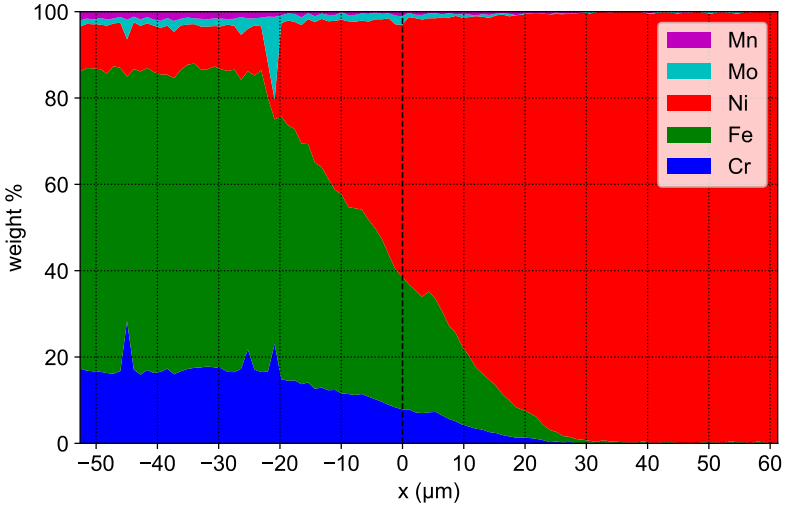

(c) Stacked area plot of major elements (>1wt%).

Figure 4.19: EDS line scan data and curve fit from 3855-hour-aged SS316L/Ni plating.

Chapter 5

Discussion

This chapter is divided into three main sections. Section 5.1 is a discussion of the microstructural features in the composites, Section 5.2 is a discussion of the reliability of calculated diffusion coefficients, and Section 5.3 presents the results of extrapolating experimental diffusion results to an end of reactor lifetime using both diffusion simulations and a diffusion model with calculated diffusion coefficients.

5.1 Microstructure of the composites

Diffusion bonding would not be used for fabricating claddings in MSRs[1]. Therefore, a central question with regard to the microstructure in diffusion couples is whether it is likely to form in composites fabricated with techniques which could be used for fabricating claddings in MSRs, such as electroplating, thermal spraying, coextrusion, and weld overlay.

In diffusion couples with Hastelloy N, interfaces were distinct with no grain overlap, and they contained porosity and Mo-rich precipitates. The amount of interfacial mixing for claddings fabricated by thermal spray most likely depends on the thermal spray technique

[1] A possible exception is the use of diffusion bonding for fabricating claddings in printed circuit heat exchangers (PCHE), which are already fabricated by diffusion bonding, but the technology readiness level for PCHEs is low, and for clad PCHEs, it is even lower.

and parameters. There would be significant interfacial mixing at the interface of claddings fabricated by weld overlay as part of billet fabrication for coextrusion. Contrarily, the micrograph from [48, p. 622] shown in Figure 5.1 reveals that there was a certain lack of interfacial mixing in SS316/Hastelloy N fabricated by sleeve coextrusion. The weld overlay and sleeve coextrusion methods are described in Section 2.7.2; the advantage of weld overlaying one of the extrusion billet layers instead of extruding two billets together (as sleeves) is that the weld overlaying creates a bond with more mixing and grain overlap [55]. There would probably be less interfacial porosity in Hastelloy N claddings fabricated by coextrusion or thermal spray than in the diffusion couples in this work. Whether a similar Mo-rich phase or other phases would precipitate at interfaces of Hastelloy N claddings fabricated by coextrusion or thermal spray depends on thermal exposure, which varies significantly between cladding techniques. Coextrusion temperatures are expected to be around 1200–1300 °C—significantly higher than the 900 °C used for diffusion bonding in this work. With regard to the coextruded SS316 and Hastelloy N shown in Figure 5.1, it was reported that "as expected, a new phase appeared at the interface between [Hastelloy N] and the stainless steel which increased in depth along the grain boundaries with increases in the temperature" [48, p. 620] (no other information is provided in [48] about this phase). To summarize, of the interfacial microstructure in the diffusion couples with Hastelloy N, a lack of grain overlap could be present in claddings fabricated by certain techniques, porosity would not be present in claddings, and it is uncertain if precipitates of the same phase would be present in claddings.

At the interface of the diffusion couples with Hastelloy N, the lack of grain overlap (i.e. presence of a grain boundary), the porosity, and the precipitates probably acted as diffusion barriers. However, this is not apparent in measured concentration profiles, which have a fairly continuous slope across the interfaces (see Figures 4.13 and 4.14). The slowing of diffusion at an interface would be expected to cause a steep concentration gradient at

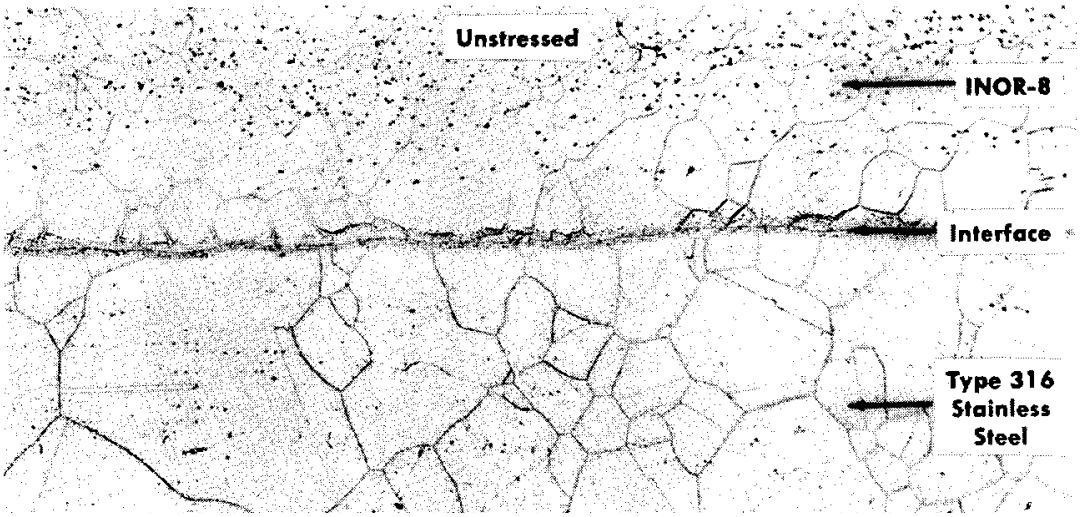

Figure 5.1: Cross-sectional optical micrograph of the interface of coextruded SS316/ Hastelloy N after 500 h at 704 °C, etched with electrolytic H_2SO_4 (2% solution), 100x. INOR-8 is the original name for Hastelloy N. [48, p. 622]

the interface relative to the concentration gradients in the metal adjacent to the interface. Additionally, there is only a small difference in calculated diffusion coefficients between 800H/Hastelloy N and SS316L/Hastelloy N even though there was significantly less interfacial porosity in SS316L/Hastelloy N. This suggests that the porosity had a small effect on overall diffusion. On the other hand, distinct interfaces with Mo-rich precipitates were observed for both material combinations, so it remains possible that these two microstructural features had a significant effect on overall diffusion.

It's likely that increasing the temperature of diffusion bonding (e.g. to around 1000 °C) would cause grain overlap at the interface of diffusion couples with Hastelloy N. Unfortunately, 900 °C is the upper temperature limit for the diffusion bonding equipment used in this work, so this possibility could not be explored. It would be worthwhile for higher temperature diffusion bonding to be tested in future work not just for improving microstructure, but also for producing temperature exposure conditions that are more representative of cladding techniques such as coextrusion and weld overlay. If diffusion bonding temperature

is increased, diffusion bonding time should be decreased to less than 2 h (e.g. 20 min) so as to minimize diffusion from the bonding process while still obtaining a metallurgical bond.

A flaw in this experiment is that SS316L was used instead of SS316H. SS316H is what would be used in MSRs, but this alloy wasn't used in this study because of difficulties with sourcing it. SS316H has more carbon content than SS316L, so there would be more carbides in SS316H, and a result, slower diffusion. Therefore, the calculated diffusion coefficients from this work for composites with SS316L are most likely an overestimation of diffusion coefficients for the same composites but with SS316H.

A layer of small grains formed at the interface of 800H/Ni plating during thermal aging. It would be undesirable for these grains to be an intermetallic phase because this would cause interfacial embrittlement (although none was measured). The expected phase for the measured composition at the interface of 800H/Ni plating is verified with the ternary Cr–Fe–Ni phase diagram in Figure 5.2, which is for 650 °C (no such phase diagram could be found for 700 °C, which is the temperature that the 800H/Ni plating was exposed to). The approximate composition of the small grains at the interface of 800H/Ni plating is marked with a red x, indicating that their phase should be fully austenitic at equilibrium for 650 °C. A 700 °C phase diagram was calculated with Thermo-Calc, which confirmed that the equilibrium position lies in the austenitic region, but it's worth noting that a 650 °C phase diagram calculated with Thermo-Calc didn't exactly match the 650 °C phase diagram in Figure 5.2 (the latter of which was determined experimentally, making it more reliable). These two 650 °C phase diagrams are compared in Figure C.1. Despite this discrepancy, it can be said with confidence that, assuming the effect from low-concentration alloying elements is insignificant, the interfacial material is austenitic at equilibrium.

During thermal aging, voids formed in Ni plating 20–30 µm from interfaces with both 800H and SS316L substrates. Olson [104] observed similar voids in 800H/Ni plating exposed to 700 °C for 500 h (compare Figures 4.18a and 5.3), except that these voids were at or near

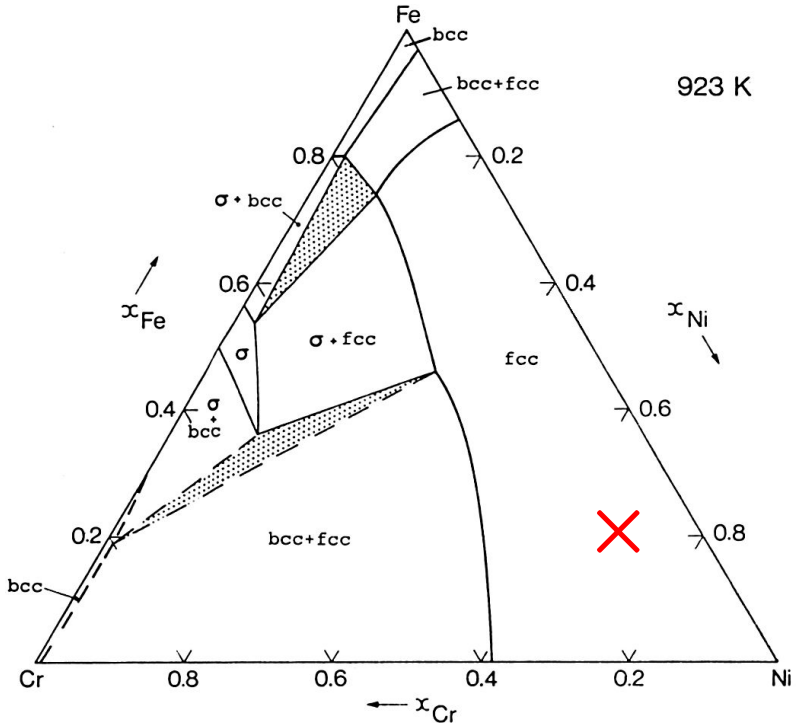

Figure 5.2: Experimental isothermal phase diagram for the Cr–Fe–Ni system at 650 °C, modified with a red x at the approximate composition (10Cr–20Fe–70Ni wt%) of the small grains at the interface of 800H/Ni plating. The unit of the axes is mol fraction. [103]

the interface, whereas in this work, voids formed 20–30 µm into the Ni plating. The only possible difference between the two experiments to explain the difference in location of the voids is the use of a Wood's Ni strike[2] as part of the electroplating fabrication process in this work, whereas it is unsure if a Ni strike was used in the work by Olson [104]. One hypothesis is that voids formed at the boundary between nickel deposited for the strike and nickel deposited for sulfamate plating. However, according to the plating shop, the Ni strike in this work was done with a current density of 108 $\mathrm{A\,m^{-2}}$ for 5 min; this amounts to a thickness of deposited nickel of 1.1 µm, which does not match with the 20–30 µm between the voids and the interfaces with the structural alloys.

One possible cause for the formation of the voids in Ni plating during thermal aging is the Kirkendall effect. Diffusion of metallic alloying elements occurs by vacancy diffusion,

[2]The Wood's Ni strike produces a thin Ni coating on stainless steel substrates and is used for improving adhesion of subsequent sulfamate Ni plating.

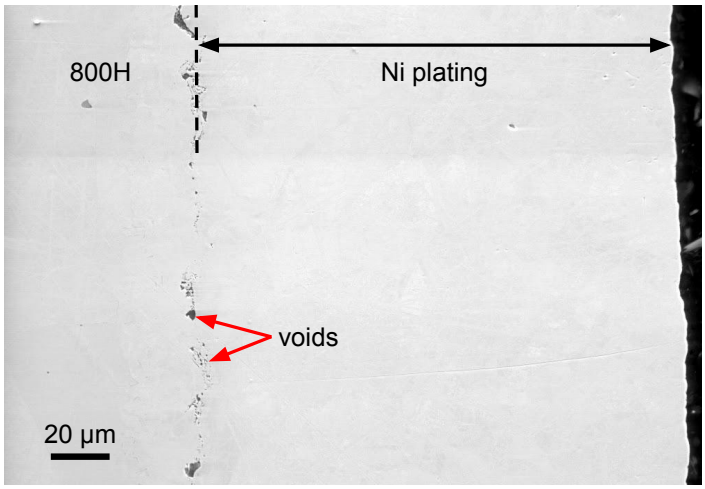

Figure 5.3: Cross-sectional SEM-SE image of 800H/Ni plating exposed to 700 °C for 500 h. A discontinuous layer of voids formed parallel to the interface, similarly to what is observed in this work, except that they are at or near the interface, whereas the voids in this work formed in the Ni plating 20–30 µm from interfaces. [104]

whereby metal atoms move into vacancies, effectively exchanging their position with the vacancies. If two materials—say, A and B—are allowed to diffuse into one another, and the diffusion of A into B is faster than the diffusion of B into A, the difference must be compensated by a net flux of vacancies into A [36, p. 45]. These vacancies can then coalesce into what are called Kirkendall voids, as shown in Figure 5.4. Kirkendall voids are commonly observed at the interface of bonded, dissimilar metals.

Diffusion of iron and chromium in nickel is faster than diffusion of nickel in γ-iron, and in the Ni-plated samples, this is compounded by the initially small grain size in the Ni plating (because diffusion is faster in smaller-grained material). This difference in diffusion rates necessitates a net diffusion of vacancies into the structural alloys, and Kirkendall voids, should they form, would be in the structural alloys. However, this is contrary to what was observed in this work: voids formed on the Ni plating side of the interfaces (although they formed at or very near to interfaces in the work by Olson [104]). This suggests that the voids are not a result of the Kirkendall effect. However, the relatively small porosity observed at the interface of SS316L/Ni plating (visible in Figure 4.19a) could be a result of

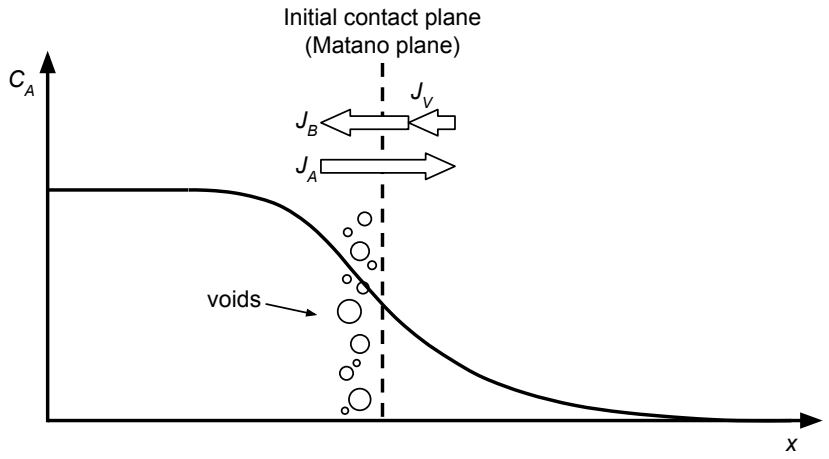

Figure 5.4: Schematic illustration of the Kirkendall effect in a binary diffusion couple showing the relative flux of species A, species B, and vacancies (J_A, J_B, and J_V), and the formation of voids. (Based on [105, Fig. 2.2].)

the Kirkendall effect. Other possible causes for the formation of the large voids in Ni plating should be investigated, and these may be related to the electroplating process. For example, the as-received Ni plating could have contained a supersaturation of point defects, including vacancies, that coalesced into voids during thermal aging at 700 °C.

The voids that formed in the Ni plating probably negatively affect its mechanical integrity and thermal conductivity. Therefore, potential ways of preventing the formation of these voids should be investigated. If their formation is linked to the small initial grain size and rapid initial diffusion in the Ni plating, a potential solution is post-fabrication heat treatment at a temperature below which the voids forms (i.e. below 700 °C), to induce microstructure equilibration without void formation. For example, Kirkendall void formation can be avoided by reducing exposure temperatures [106]. Along these lines, voids might not form in Ni claddings fabricated with other techniques, such as co-extrusion and weld overlay, because these don't have the small grains and possibly high defect concentration of Ni plating.

5.2 Reliability of calculated diffusion coefficients

Several factors affect the reliability of the calculated diffusion coefficients presented in Tables 4.1 and 4.2 and in Section A.1. The most obvious factor is the quality of curve fits. For both Ni-plated samples and diffusion couples with Hastelloy N, curve fits were excellent, both qualitatively and quantitatively, as seen from the curve fits and r-squared values, respectively.

The next factor to consider is whether the diffusion kinetic regime is type A according to Harrison's classification of diffusion kinetics (described in Section 2.2.2), since the diffusion model used for calculating diffusion coefficients assumes that it is type A. Equation 2.16 is the criterion for type A diffusion; it can be rearranged to determine the amount of time required for diffusion to be type A if average grain size and lattice diffusion coefficients are known. Grain size varied with time for Ni plating, so a conservative approximation was made by using the largest grain sizes (that is, grain sizes after thermal aging). Also, the diffusion coefficients that were experimentally determined in this work are effective diffusion coefficients, so these effective diffusion coefficients had to be approximated as lattice diffusion coefficients to be used in Equation 2.16. With these approximations, the results of verifying if the criterion is satisfied for the thermal aging times and calculated chromium diffusion coefficients are as follows. For diffusion couples with Hastelloy N aged for 5840 h, the diffusion kinetic regime was calculated to be type B with a minimum thermal aging time for type A diffusion of several hundred years. For SS316L/Ni plating aged for 3855 h, the diffusion kinetic regime was calculated to be type A. For 800H/Ni plating aged for 3855 h, the diffusion kinetic regime was calculated to be type A in the Ni plating, but type B in the 800H with a minimum thermal aging time for type A diffusion of roughly 23 years.

Lattice diffusion coefficients are smaller than effective diffusion coefficients (because effective diffusion coefficients include the diffusion-accelerating effect of grain boundaries),

so if actual lattice diffusion coefficients were used, this would increase calculated minimum thermal aging times for type A diffusion. However, this source of error is countered by the intergranular precipitates in Hastelloy N and the structural alloys, which probably slow grain boundary diffusion and reduce minimum thermal aging times for type A diffusion. Despite these considerations, type B diffusion remains likely for structural alloys with Hastelloy N claddings exposed to 700 °C for reactor lifetimes. For Ni-plated structural alloys, the assumption of type A diffusion is reasonably accurate.

The consequence of the diffusion kinetic regime being type B for 800H/Hastelloy N and SS316L/Hastelloy N is that the calculated diffusion coefficients for these composites have poor reliability for quantitative predictions of long-term diffusion. By not fully including the effect of grain boundary diffusion, the calculated diffusion coefficients forecast inaccurately slow diffusion. For type B kinetics, diffusion models such as those in [27, pp. 341–342] must be used. These diffusion models don't group D_{gb} and D_l into an effective diffusion coefficient, and they require measurement of average layered concentration with a method such as radiotracer serial sectioning [27]. Average layered concentration cannot be measured with EDS line scans, the method used in this work.

There is another factor that affects the reliability of calculated diffusion coefficients, and it is specific to the diffusion couples: In order to compensate for the diffusion that occurs during diffusion bonding, the combined term $(Dt)_{900\,^\circ\mathrm{C},bonding}$ was calculated from EDS line scans of non-thermally-aged diffusion couples with Equation 3.1, and this also involves an assumption of type A diffusion. Unfortunately, due to the unknown amount of time during which bonds were formed in the diffusion bonding process, it is not possible to determine $D_{900\,^\circ\mathrm{C},bonding}$ alone, which could have enabled verification of whether diffusion was type A. Despite this, it is possible to determine the potential magnitude of propagated error if diffusion were to be type B during diffusion bonding; this is done by equating the expression in the square root of Equation 3.2 to $D_{700\,^\circ\mathrm{C}}\,t_{700\,^\circ\mathrm{C},eff}$, where $t_{700\,^\circ\mathrm{C},eff}$ is the

effective 700 °C thermal aging time for diffusion bonding and thermal aging, combined:

$$D_{700^\circ\mathrm{C}}\, t_{700^\circ\mathrm{C},eff} = (Dt)_{700^\circ\mathrm{C}} + (Dt)_{900^\circ\mathrm{C},bonding} \tag{5.1}$$

And then, solving for $t_{700^\circ\mathrm{C},eff}$:

$$t_{700^\circ\mathrm{C},eff} = t_{700^\circ\mathrm{C}} + \frac{(Dt)_{900^\circ\mathrm{C},bonding}}{D_{700^\circ\mathrm{C}}} \tag{5.2}$$

With $t_{700^\circ\mathrm{C},eff}$ for thermally aged diffusion couples, the fraction of total diffusion that was from diffusion bonding can be determined. The results of this calculation for diffusion couples with Hastelloy N are shown in Table 5.1. A large fraction of total diffusion occurred during the diffusion bonding process (∼90% for the 1460-hour-aged diffusion couples and ∼40% for the 5840-hour-aged diffusion couples). This gives appreciation of the potential error from assuming that diffusion is type A during diffusion bonding, and it gives appreciation of the importance of long thermal aging times for reducing this potential error. However, it is very possible that diffusion was type A during diffusion bonding because diffusion coefficients increase exponentially with temperature (see Equation 2.15), so the minimum thermal aging time required for type A diffusion decreases exponentially with temperature.

Table 5.1: Effective 700 °C thermal aging times and percentages of total diffusion that are from diffusion bonding for diffusion couples with Hastelloy N.

	800H	SS316L
1460 h of thermal aging	16 800 h	11 500 h
% diffusion from diffusion bonding	91%	87%
5840 h of thermal aging	9530 h	9880 h
% diffusion from diffusion bonding	39%	41%

For cladding techniques that are applicable to components in MSRs and that involve significant interfacial mixing during fabrication (e.g. coextrusion), extrapolations of diffusion

results from thermal aging experiments—such as with calculated diffusion coefficients and a diffusion model—also require the method of compensating for initial diffusion. (An example of this is in [55].) On the other hand, cladding techniques such as electroplating and CVD do not require the method of compensating for initial diffusion because they create sharp interfaces. The experimental advantage of sharp interfaces is countered by the disadvantage of greater interfacial stress concentration, although post-fabrication heat treatment is a viable solution for reducing interfacial stress concentration by causing interfacial recrystallization and mixing. However, if such post-fabrication heat treatments are to be used, composites that are thermally aged in experiments should undergo the same heat treatment prior to thermal aging in order to have the same microstructure as in actual components, and this brings us back to square zero of requiring the method of compensating for initial diffusion.

Although the reliability of calculated diffusion coefficients for diffusion couples with Hastelloy N is less than ideal, an important conclusion can be made: Unless the ratio of D_{gb} to D_l is far greater for Hastelloy N than nickel, Hastelloy N has significantly more diffusion resistance. This statement is substantiated by the diffusion coefficients from the literature which are discussed in Section 2.5.5, by the fact that chromium diffusion is significantly slower in molybdenum than in nickel [59], and that Hastelloy N—unlike nickel—forms intergranular carbides that probably slow diffusion. An additional conclusion worth noting is that the diffusion resistance of the composites with SS316L and 800H was similar; the choice of Hastelloy N versus nickel as cladding materials has far more impact on diffusion resistance.

5.3 Extrapolations of diffusion results to an end of reactor lifetime

This section includes results of extrapolating experimental diffusion results to an end of reactor lifetime of seven years, which is the expected lifetime of the primary reactor components in Terrestrial Energy's IMSR® [107]. For comparison, the expected lifetime of the primary reactor components of China's liquid-fueled thorium molten salt reactor (TMSR-LF) is five years [1, p. 534]. Two methods were used for extrapolating diffusion results to seven years:

1. Simulations with Thermo-Calc DICTRA
2. Inputting calculated diffusion coefficients into the diffusion model of Equation 2.13 with $t = 7\,\text{years}$

5.3.1 Extrapolations with Thermo-Calc DICTRA simulations

Diffusion simulations are a useful tool for extrapolating diffusion results because they fully account for the concentration-dependence of diffusion and they can include boundary conditions of fluoride salt corrosion (i.e. leaching of certain elements). The first step to extrapolating diffusion results with simulations was curve fitting concentration profiles from diffusion simulations with concentration profiles that were experimentally measured. The activation energy ratios determined from these curve fits were then used to extrapolate diffusion to an end of reactor lifetime with a boundary condition of near-zero chromium concentration at the outer surface of claddings.

Curve fitting simulation results with experimental data

Averaged chromium concentration data from EDS line scans of Ni-plated samples along with curve fitted simulation results are shown in Figure 5.5. For 800H/Ni plating, the concentration gradient decreases for approximately 15 µm at the interface, but there is no

decrease in concentration gradient in the simulation result. This discrepancy is due to the assumption of uniform grain size in the simulation, whereas in the actual material, small grains formed at the interface and these small grains caused locally accelerated diffusion. For SS316L/Ni plating, there is good match between the shapes of the simulated and experimental concentration profiles. Compared to 800H/Ni plating, there is less variation in grain size across SS316L/Ni plating, so the assumption of uniform grain size was less erroneous.

In Thermo-Calc DICTRA, there is no way to include a position- and time-dependent grain size contribution to diffusivity. Grain size was fixed to 20 µm and activation energy ratio was the curve fit variable. The calculated activation energy ratios shown in Figure 5.5 cannot be used with other grain sizes or for other materials or diffusion temperatures. If it was possible to include position- and time-dependent grain size contribution to diffusivity, grain size could be experimentally determined as a function of time and position and inputted into simulations. Then, simulation results would most likely match experimental concentration profiles more closely. However, it would remain impossible to reliably use calculated activation energy ratios for simulating diffusion at other temperatures than 700 °C unless the grain size evolution at those other temperatures is known.

Unfortunately, issues were encountered with simulations of diffusion in 800H/Hastelloy N and SS316L/Hastelloy N. For 800H/Hastelloy N, an adequate curve fit could not be obtained for any activation energy ratio. Figure 5.6a shows the closest curve fit that could be obtained, which is for an activation energy ratio of 1. An activation energy ratio of 1 means that lattice and grain boundary diffusivities are the same, making D_{eff} equal to D_l (see Equation 2.17). In reality, D_{eff} should be greater than D_l because of the accelerating effect of grain boundary diffusion. The simulations don't take into account the presence of diffusion-slowing precipitates in the alloys, so this may explain why an adequate curve fit could not be obtained. It is possible to include precipitates as a DICTRA simulation input, but this option wasn't explored in this work due to uncertainty about the composition, volume fraction, and

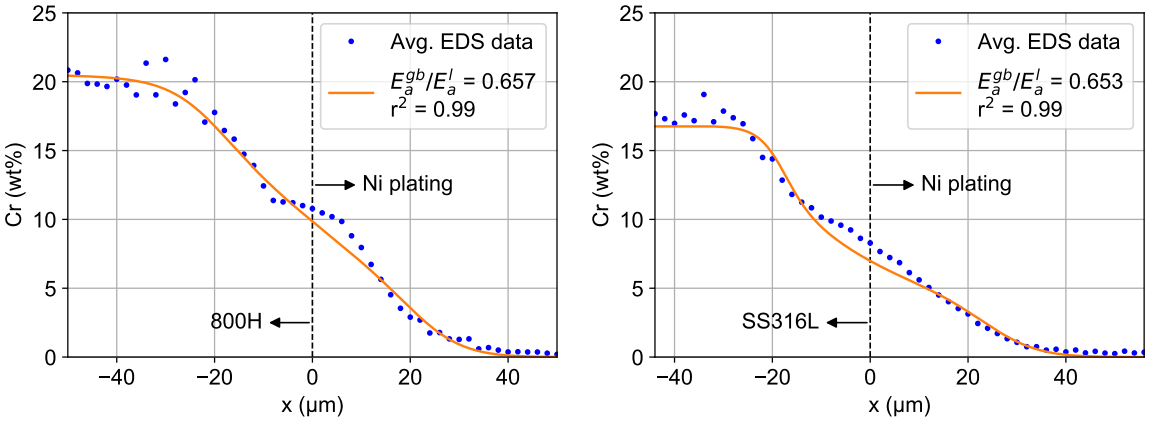

(a) 800H/Ni plating.

(b) SS316L/Ni plating.

Figure 5.5: Curve fits of simulation results with averaged EDS data for chromium in Ni-plated samples. From these curve fits, activation energy ratios were determined with grain size fixed to 20 µm. The EDS data is from 9 line scans averaged into 2 µm bins. The activation energy ratios shown in these plots cannot be used with other grain sizes or for other materials or diffusion temperatures.

distribution of the precipitates in the diffusion couples. For SS316L/Hastelloy N, DICTRA simulations predicted uphill diffusion that did not match experimental data at all, as shown in Figure 5.6b. During these simulations, uphill diffusion started out steep at the interface and then leveled out to some extent. These simulations were attempted with several other thermodynamic and mobility databases and the result remained the same. This issue was discussed with technical staff from Thermo-Calc, but no solution was found. As a next step, a useful test would be to run the same simulations with Hastelloy N in another diffusion simulation software to see if the issues are specific to DICTRA.

Simulations with a corrosion boundary condition

Unless loss of mechanical integrity of claddings or formation of void networks in underlying structural alloys are the durability bottlenecks, the designer's goal when selecting cladding thickness is to minimize the combined thickness of the cladding and the diffusion zone in the structural alloy. The optimal cladding thickness most likely involves significant amounts of diffusing species reaching salt–cladding interfaces (i.e. the diffusing species will not

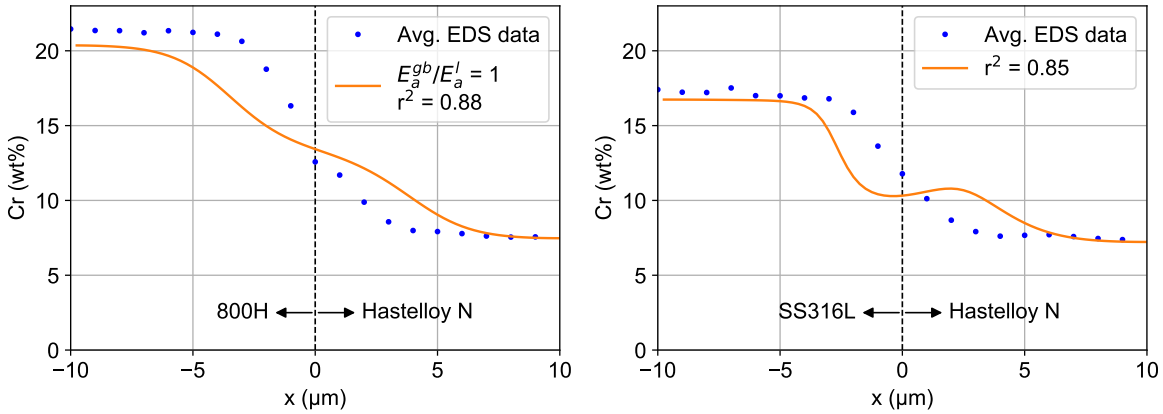

(a) 800H/Hastelloy N, closest possible curve fit. (b) SS316L/Hastelloy N, note the uphill diffusion.

Figure 5.6: Curve fits of simulation results with averaged EDS data for chromium in diffusion couples with Hastelloy N. For 800H/Hastelloy N, an adequate curve fit could not be obtained for any activation energy ratio, and for SS316L/Hastelloy N, the shape of the concentration profile from simulation did not match experimental data. The EDS data is from 27 line scans averaged into 1 µm bins.

perceive semi-infinite cladding thickness). Therefore, diffusion extrapolations should take into account the accumulation of corrosion-resistant elements (such as nickel) and leaching of corrosion-prone elements (such as chromium) at salt–cladding interfaces. Complementary error function diffusion models cannot be used towards this objective because they assume semi-infinite cladding thickness. On the other hand, finite element diffusion simulation software such as Thermo-Calc DICTRA can take fixed flux or fixed concentration boundary conditions as simulation inputs.

With Thermo-Calc DICTRA, experimental diffusion results for Ni-plated samples were extrapolated to seven years with a corrosion boundary condition of near-zero chromium concentration and zero flux for all other elements. 20 µm grain size and the activation energy ratios from the curve fits shown earlier were inputted into the simulations. The simulation results of chromium concentration profiles are shown in Figure 5.7 for varying cladding thickness. Section A.2 includes the same results but for other elements than chromium. What is remarkable about these results is that for decreasing cladding thickness, the depth of

diffusion zones in the structural alloys does not increase. This puts forward the possibility that Ni plating would not provide a performance advantage.

Molten fluoride salt corrosion of 800H and SS316L alloys is known to cause formation of intergranular void networks, which accelerate corrosion due to penetration of salt. The formation of voids depends on presence of chromium and on its rapid diffusion out of the salt-exposed metals. As seen in Figure 5.7, concentration gradients in Ni plating increase as its thickness is decreased. It follows that for thin claddings, voids are more likely to form in the claddings and underlying structural alloy, and the depth of jeopardized material would most likely be farther into the structural alloys than what is predicted by the simulation results in Figure 5.7.

For simulations of 800H and SS316L with 100 μm of Ni plating and a corrosion boundary condition, diffusion zone thicknesses in the structural alloys were calculated from concentration profiles and are plotted as a function of time in Figure 5.8c. The threshold condition that was used for determining diffusion zone thickness was arbitrarily chosen to be a 10% decrease in chromium mass content in the structural alloys. For example, for the 20.5 wt% chromium in the 800H used in this study, a 10% decrease in chromium mass content corresponds to a 2.05 wt% decrease in chromium concentration. As discussed in Section 2.2.1, the actual thresholds for structural alloys would probably be determined by designers based on the effect of composition changes on mechanical properties. As seen in Figure 5.8c, the thickness of the diffusion zone increased more quickly in Ni-plated 800H than in Ni-plated SS316L, but the difference is not very large (118 μm versus 93 μm at seven years). It should be noted, however, that these results do not account for random error or systematic error, such as from the curve fitting step.

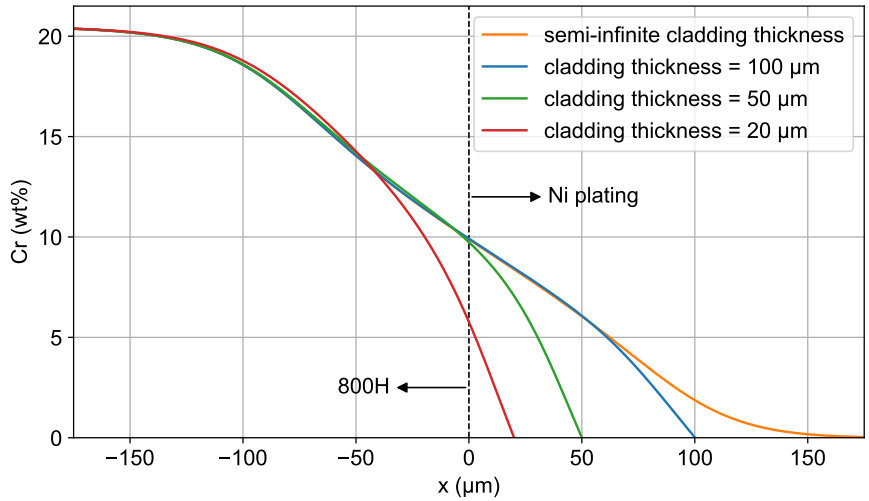

(a) 800H/Ni plating.

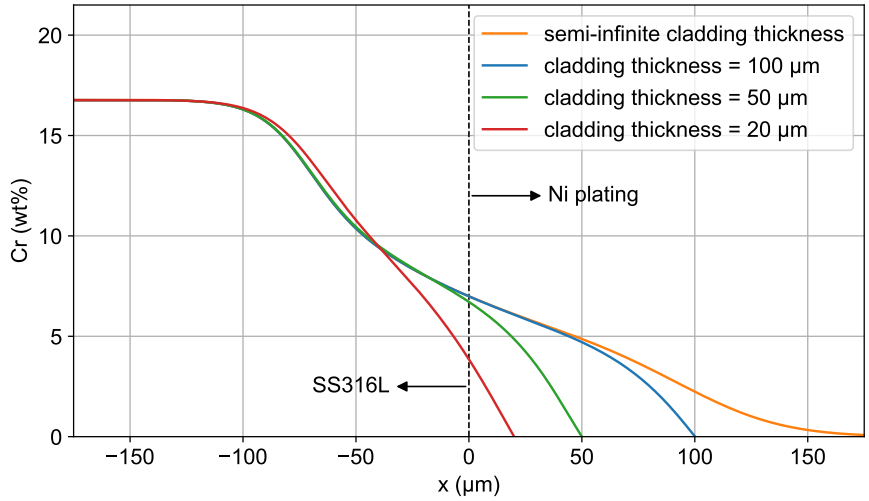

(b) SS316L/Ni plating.

Figure 5.7: Extrapolation of chromium diffusion to seven years for varied cladding thickness, comparing the depth of diffusion in the structural alloys. A salt–cladding interface boundary condition of near-zero chromium concentration is conservatively assumed.

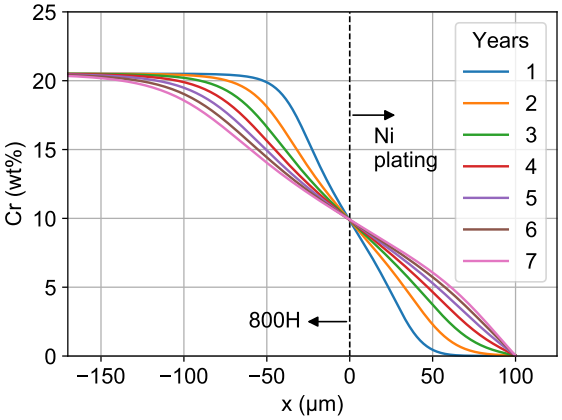

(a) 800H/Ni plating: Cr diffusion.

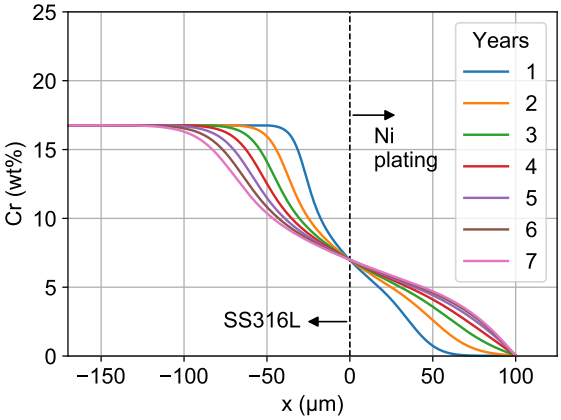

(b) SS316L/Ni plating: Cr diffusion.

(c) Effect of thermal aging time on the thickness of diffusion zones in structural alloys. Diffusion zone thickness values were calculated from results of diffusion simulations partially shown in (a) and (b), with a threshold condition of 10% decrease in chromium mass content in the structural alloys.

Figure 5.8: Predicted growth of the diffusion zone in structural alloys with 100 µm of Ni plating exposed to 700 °C with maximal chromium leaching at the surface of the Ni plating (i.e. fully diffusion-limited corrosion).

5.3.2 Extrapolations with calculated diffusion coefficients

In Figure 5.9, results are shown for extrapolations of experimental diffusion results to seven years with the diffusion model of Equation 2.13 and the calculated diffusion coefficients from Tables 4.1 and 4.2 for the longer thermal aging times (5840 h and 3855 h, respectively). Actual diffusion would be greater than what is predicted in Figure 5.9a for 800H/Hastelloy N and SS316L/Hastelloy N because of the limitations with diffusion coefficient reliability discussed in Section 5.2. However, any error is probably much smaller than the difference in diffusion rates between composites with Hastelloy N versus composites with nickel (compare Figure 5.9a versus 5.9b).

Even if actual diffusion in composites with Hastelloy N is three times what is predicted in Figure 5.9a, no more than around 50 µm of Hastelloy N cladding thickness would be needed. However, the optimal Hastelloy N cladding thickness may be greater than this because, up to a certain extent, increasing the thickness of claddings reduces the risk of local imperfections (e.g. voids) or variation in thickness that could cause a cladding to fail as a corrosion barrier. Increasing the thickness of Hastelloy N claddings beyond what is beneficial with regard to diffusion would diminish the diffusion-resistance advantage of Hastelloy N over nickel. However, even if the same thickness of nickel and Hastelloy N claddings would be used, Hastelloy N presents an advantage in that its use would be accompanied by less required sacrificial structural alloy thickness (for example, 50 µm if we stick to the assumption of tripled diffusion, whereas the use of Ni plating would require $\sim$200 µm of sacrificial structural alloy thickness).

Figure 5.9b includes an extrapolated concentration profile based on a diffusion coefficient from Olson [104] for 800H/Ni plating thermally aged at 700 °C for 500 h. They used the same method of curve fitting a complementary error function model to EDS line scan data as in this work. The chromium diffusion coefficient for 800H/Ni plating from this work is $1.6 \times 10^{-17} \pm 3.4 \times 10^{-18}$ m^2 s^{-1}, which is smaller than the chromium diffusion coefficient

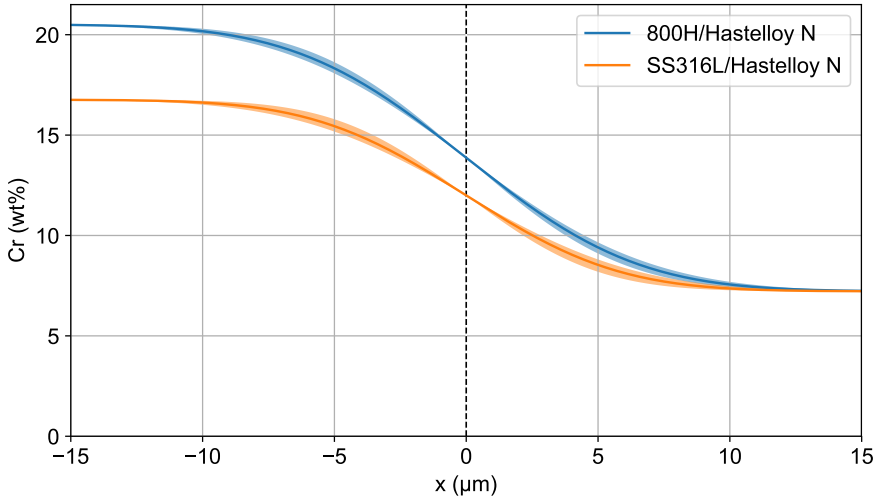

(a) Extrapolation of chromium diffusion based on calculated coefficients for 800H/Hastelloy N and SS316L/Hastelloy N diffusion couples thermally aged for 5840 h.

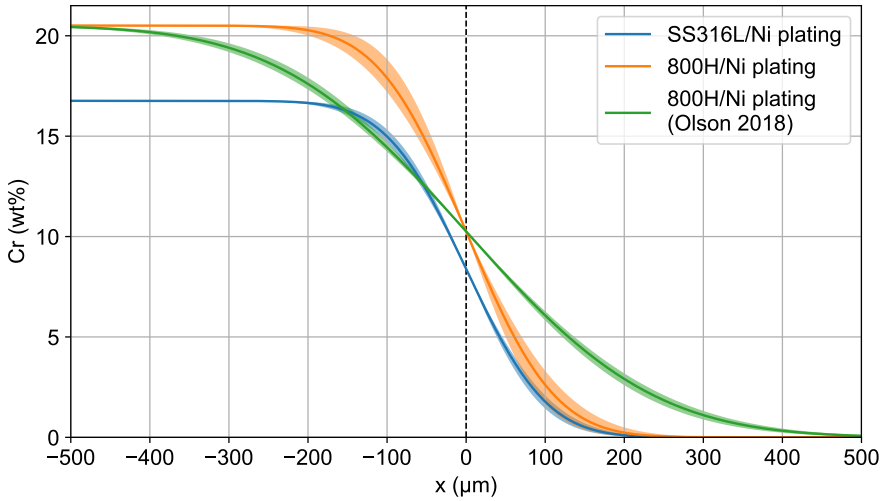

(b) Extrapolations of chromium diffusion based on calculated diffusion coefficients for SS316L/Ni plating and 800H/Ni plating from this work (3855 h of thermal aging), and 800H/Ni plating from Olson [104] (500 h of thermal aging).

Figure 5.9: Extrapolated chromium concentration profiles for 7 years of aging at 700 °C. The dark lines in the middle of the bands were calculated with average diffusion coefficients, and the upper and lower bounds of the pale bands were calculated with the 95% confidence intervals of the average diffusion coefficients.

of $7.9 \times 10^{-17} \pm 9.1 \times 10^{-18}$ $m^2 s^{-1}$ from Olson [104]. An important difference between the two experiments is duration of thermal aging, which was 3855 h in this study versus 500 h in Olson's experiment. In theory, shorter thermal aging time would cause diffusion to be closer to or further into the type B regime. In other words, the effect of grain boundary diffusion would be less captured in EDS line scans, causing calculated diffusion coefficient to be smaller. The opposite difference in diffusion coefficients was observed, so the effect of thermal aging time on diffusion kinetic regimes does not explain the discrepancy. Another possible explanation is differences in grain size. According to mill certificates, the average grain size of the 800H alloy that Olson [104] used is ASTM no. 3.5 (107 μm) whereas the average grain size of the 800H in this study is ASTM no. 3.0 (127 μm). Exposure to 700 °C did not appear to affect the grain size of the 800H. The average grain size of thermally aged Ni plating is also slightly larger in this study. However, a more important consideration is the very large increase in the grain size of Ni plating during thermal aging at 700 °C. For the shorter thermal aging time used by Olson [104], there is a greater fraction of thermal aging time during which small grains are present in Ni plating, as illustrated in Figure 5.10. Therefore, for the shorter thermal aging time, the diffusion-accelerating effect of small initial grain size has a larger increasing effect on calculated diffusion coefficients. This hypothesis is supported by the result in this study of the calculated diffusion coefficients for 1461 h of aging being greater than those for 3855 h of aging (see Table 4.2).

5.3.3 Comparison of extrapolation techniques

Comparisons of simulation and diffusion model extrapolations of diffusion to a seven-year reactor lifetime are shown in Figure 5.11. The same extrapolation results are shown apart in the previous two sections (Sections 5.3.1 and 5.3.2). The simulation results in Figure 5.11 are for semi-infinite cladding thickness. For 800H/Ni plating, the results of the two extrapolation techniques match quite well. For SS316L/Ni plating, the results match well in the Ni plating

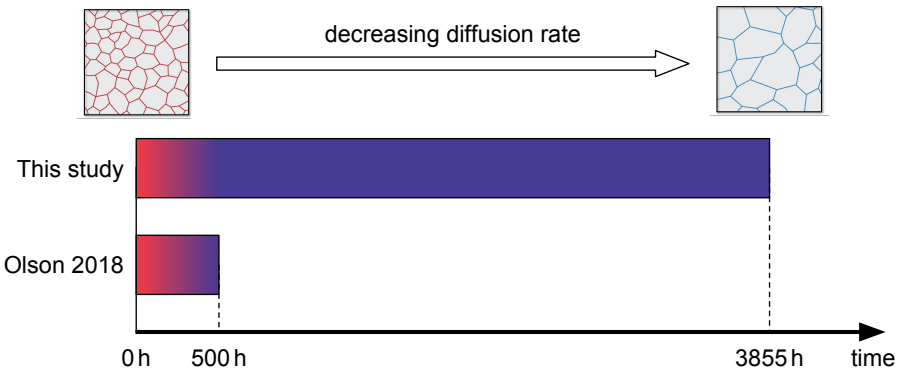

Figure 5.10: Schematic illustration of the fraction of thermal aging time during which initially small grains are present in Ni plating.

region but not in the SS316L region. The poor match in the SS316L region exemplifies the importance of the concentration-dependence of diffusion, which is taken into account in simulations with Thermo-Calc DICTRA but not in the diffusion model of Equation 2.13.

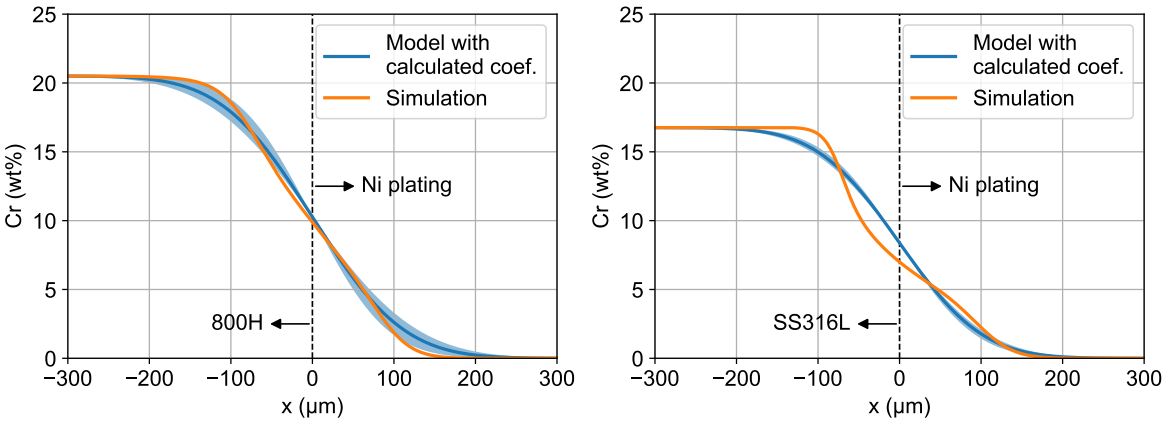

(a) 800H/Ni plating.

(b) SS316L/Ni plating.

Figure 5.11: Comparisons of simulation and diffusion model extrapolations of diffusion at 700 °C to a seven-year reactor lifetime.

Chapter 6

Conclusions and future work

This thesis demonstrates that Hastelloy N is a promising cladding material due to its excellent diffusion resistance. In addition, it's possible for there to be little to no benefit to Ni plating as a corrosion barrier. These conclusions are expanded upon below.

6.1 Overall conclusions

The overall conclusions of this thesis are:

1. **Hastelloy N is highly diffusion resistant:** As a cladding material, Hastelloy N is highly likely to have significantly more diffusion resistance than nickel. The combined thickness of Hastelloy N claddings and diffusion zones in 800H or SS316H structural alloys could be less than 100 μm after 7 years at 700 °C. The difference in diffusion resistance between 800H and SS316L structural alloys was relatively small.
2. **Nickel cladding might be detrimental:** The results of diffusion simulations with a corrosion boundary condition of near-zero chromium concentration suggest that, in terms of minimizing the combined thickness of claddings and diffusion zones in structural alloys, performance might be worsened by increasing the thickness of

Ni cladding. However, this conclusion is uncertain because the simulations involve several simplifications and assumptions.

3. **Voids formed in Ni plating:** During thermal aging at 700 °C, voids 5–15 µm in size formed in Ni plating near its interface with both 800H and SS316L substrates. Similar voids were observed by Olson [104] in 800H/Ni plating exposed to 700 °C for 500 h. These voids may affect the mechanical integrity of Ni plating.

6.2 Future work

The future work recommended for continued performance evaluation of claddings is:

1. **Thermal aging studies with Hastelloy N claddings fabricated with techniques that are applicable to components in MSRs:** Despite the convenience and flexibility of diffusion bonding, future research on claddings should prioritize cladding techniques, such as thermal spray and coextrusion, that are applicable to components in MSRs. This would improve the relevance of microstructure results, and since microstructure affects diffusion rates, it would also improve the reliability of diffusion results. The diffusion results of this study combined with the extensive experience base from the use of Hastelloy N in the MSRE strongly support the case for furthering its development as a cladding material.

2. **Concentration profile measurements of low-concentration alloying elements and with average layered methods:** As discussed in Section 2.2.1, the thickness of the diffusion zone in structural alloys is probably defined by loss of mechanical properties from compositional change. Therefore, since low-concentration (in this context, <1 wt%) alloying elements can have a major effect on mechanical properties, their diffusion should be measured and extrapolated, and this implies the use of other measurement techniques than EDS. Also, if the type B kinetic regime is unavoidable, as is

most likely the case for composites with Hastelloy N, methods of measuring average layered concentration should be used for obtaining concentration profiles.

3. **Corrosion and irradiation studies:** Before claddings are implemented in MSRs, research will have to be conducted on their durability when exposed to the worst foreseeable conditions of irradiation and corrosion in molten fluoride salts. Molten salt corrosion tests are required to study the effects of alloying element leaching and void formation on the durability of claddings, and also for enabling the use of accurate corrosion boundary conditions in diffusion simulations. Additionally, for high-dose applications, future work must include investigations of the properties of composites under irradiation.

4. **Developing methods of avoiding void formation in Ni plating**: In future research of Ni plating as a corrosion barrier in molten fluoride salts, it should be determined whether void formation can be avoided—for example, by heat treatment prior to high-temperature exposure. If void formation cannot be avoided and mechanical testing confirms that voids increase the likelihood of cladding failure, Ni plating will have to be ruled out as an option.

5. **Improved diffusion simulations**: As demonstrated in this thesis, diffusion simulations are a useful tool for extrapolating the results of thermal aging and corrosion experiments to end of reactor lifetimes. Two potential improvements to the diffusion simulations in this study are (1) including the effect of precipitates, such as intergranular carbides, on diffusion and (2) boundary conditions that depend on the chemical condition of molten salts (redox potential, impurities, etc.).

References

[1] T. J. Dolan, *Molten Salt Reactors and Thorium Energy*. Woodhead Publishing, 2017.

[2] Sandvik, "Composite tube for boilers." [Online]. Available: https://www.materials.sandvik/globalassets/global/downloads/products_downloads/tubular-products/s-1219-ps-eng_3r12_oct_2016.pdf (Accessed 2017-10-13).

[3] S. R. Greene, D. E. Holcomb, J. C. Gehin, J. J. Carbajo, A. T. Cisneros, W. R. Corwin, D. Ilas, D. F. Wilson, V. K. Varma, E. C. Bradley, and G. L. Yoder, "SmAHTR – A Concept for a Small, Modular Advanced High Temperature Reactor," in *5th High Temperature Reactor Technology conference*, 2010.

[4] X. Shi, K. Yu, L. Jiang, C. Li, Z. Li, and X. Zhou, "Microstructural characterization of Ni-201 weld cladding onto 304 stainless steel," *Surface and Coatings Technology*, vol. 334, pp. 19–28, 2018.

[5] P. Sabharwall, H. Schmutz, C. Stoots, and G. Griffith, "Tritium production and permeation in high-temperature reactor systems," in *Proceedings of the ASME 2013 Heat Transfer Summer Conference*, 2013.

[6] M. Rosenthal, R. Briggs, and P. Haubenreich, "Molten-salt reactor program semiannual progress report for period ending February 28, 1971, ORNL-4676," Oak Ridge National Laboratory, Tech. Rep., 1971.

[7] H. E. McCoy and J. R. Weir, "Development of a Titanium-Modified Hastelloy With Improved Resistance To Radiation Damage," in *Irradiation Effects in Structural Alloys for Thermal and Fast Reactors*. ASTM, 1968, pp. 290–311.

[8] C. W. Forsberg, P. F. Peterson, and H. Zhao, "High-Temperature Liquid-Fluoride-Salt Closed-Brayton-Cycle Solar Power Towers," *Journal of Solar Energy Engineering*, vol. 129, no. 2, pp. 141–146, 2007.

[9] A. Sagara, H. Yamanishi, S. Imagawa, T. Muroga, T. Uda, T. Noda, S. Takahashi, K. Fukumoto, T. Yamamoto, H. Matsui, A. Kohyama, H. Hasizume, S. Toda, A. Shimizu, A. Suzuki, Y. Hosoya, S. Tanaka, T. Terai, D. K. Sze, and O. Motojima, "Design and development of the Flibe blanket for helical-type fusion reactor FFHR," *Fusion Engineering and Design*, vol. 49-50, pp. 661–666, 2000.

[10] K. Sridharan and T. Allen, "Corrosion in Molten Salts," in *Molten salt chemistry, from lab to applications*, F. Lantelme and H. Groult, Eds. Elsevier Inc., 2013, pp. 241–267.

[11] M. S. Sohal, M. A. Ebner, S. Piyush, and P. Sharpe, "Engineering Database of Liquid Salt Thermophysical and Thermochemical Properties, INL/EXT-10-18297 Rev. 1," Idaho National Laboratory, Tech. Rep., 2013.

[12] D. Olander, "Redox condition in molten fluoride salts: Definition and control," *Journal of Nuclear Materials*, vol. 300, no. 2-3, pp. 270–272, 2002.

[13] V. Ignatiev and A. Surenkov, "Corrosion phenomena induced by molten salts in Generation IV nuclear reactors," in *Structural Materials for Generation IV Nuclear Reactors*. Woodhead Publishing, 2016, ch. 5, pp. 153–189.

[14] W. R. Grimes, "Molten-salt reactor chemistry," *Nuclear Applications and Technology*, vol. 8, no. 2, pp. 137–155, 1970.

[15] D. F. Williams, "Assessment of Candidate Molten Salt Coolants for the Advanced High-Temperature Reactor (AHTR), ORNL/TM-2006/12," Oak Ridge National Laboratory, Tech. Rep., 2006.

[16] L. C. Olson, "Materials Corrosion in Molten LiF–NaF–KF Eutectic Salt," PhD Thesis, University of Wisconsin–Madison, 2009.

[17] J. Koger, "Alloy Compatibility with LiF–BeF_2 Salts Containing ThF_4 and UF_4, ORNL/TM-4286," Oak Ridge National Laboratory, Tech. Rep., 1972.

[18] P. Calderoni and C. Cabet, "Corrosion issues in molten salt reactor (MSR) systems," in *Nuclear Corrosion Science and Engineering*, D. Féron, Ed. Woodhead Publishing, 2012, ch. 23, pp. 842–865.

[19] H. Ai, J. Hou, X. X. Ye, C. L. Zeng, H. Sun, X. Li, G. Yu, X. Zhou, and J. Q. Wang, "Influence of graphite-alloy interactions on corrosion of Ni–Mo–Cr alloy in molten fluorides," *Journal of Nuclear Materials*, vol. 503, pp. 116–123, 2018.

[20] L. M. Toth, G. D. Del Cul, S. Dai, and D. H. Metcalf, "Molten fluoride fuel salt chemistry," in *AIP Conference Proceedings*, vol. 346, 1995, pp. 617–626.

[21] P. N. Haubenreich and J. R. Engel, "Experience with the Molten-Salt Reactor Experiment," *Nuclear Applications and Technology*, vol. 8, no. 2, pp. 118–136, 1970.

[22] H. E. McCoy and R. E. Gehlbach, "Influence of Irradiation Temperature on Creep-Rupture Properties of Hastelloy-N," *Nuclear Technology*, vol. 11, no. 1, pp. 45–60, 1971.

[23] M. Rosenthal, R. Briggs, and P. Kasten, "Molten-salt reactor program semiannual progress report for period ending August 31, 1967, ORNL-4191," Oak Ridge National Laboratory, Tech. Rep., 1967.

[24] H. Zhu, R. Holmes, T. Hanley, J. Davis, K. Short, and L. Edwards, "High-temperature corrosion of helium ion-irradiated Ni-based alloy in fluoride molten salt," *Corrosion Science*, vol. 91, pp. 1–6, 2015.

[25] G. Zheng, D. Carpenter, L.-w. Hu, and K. Sridharan, "High Temperature Corrosion of Structural Alloys in Molten Li_2BeF_4 (FLiBe) Salt," *Advances in Materials Science for Environmental and Energy Technologies V: Ceramic Transactions*, vol. 260, pp. 93–101, 2016.

[26] ASME, "Power Piping Code - B31.1," 2014.

[27] P. Heitjans and J. Karger, *Diffusion in Condensed Matter – Methods, Materials, Models*. Springer, 2005.

[28] J. Kirkaldy and D. Young, *Diffusion in the Condensed State*. Institute of metals, 1987.

[29] J. Crank, *The mathematics of diffusion*, 2nd ed. Oxford University Press, 1975.

[30] S. K. Kailasam, J. C. Lacombe, and M. E. Glicksman, "Evaluation of the methods for calculating the concentration-dependent diffusivity in binary systems," *Metallurgical and Materials Transactions A*, vol. 30, no. 10, pp. 2605–2610, 1999.

[31] W. D. Callister and D. G. Rethwisch, *Materials science and engineering – An introduction*, 8th ed. Wiley, 2010.

[32] V. Rothova, "Evaluation of diffusion data in the type AB transition regime," *Journal of Physics and Chemistry of Solids*, vol. 68, no. 5-6, pp. 791–794, 2007.

[33] D. Porter, K. Easterling, and M. Sherif, *Phase Transformations in metals and alloys*. CRC Press, 2009.

[34] L. Olson, K. Sridharan, M. Anderson, and T. Allen, "Nickel-plating for active metal dissolution resistance in molten fluoride salts," *Journal of Nuclear Materials*, vol. 411, no. 1-3, pp. 51–59, 2011.

[35] G. Was, *Fundaments of Radiation Materials Science: Metals and Alloys*. Springer, 2007.

[36] R. W. Balluffi, S. M. Allen, and W. C. Carter, *Kinetics of materials*. Wiley, 2005.

[37] G. Zheng, "Corrosion Behavior of Alloys in Molten Fluoride Salts," Ph.D. dissertation, University of Wisconsin–Madison, 2015.

[38] T. Sourmail and H. K. D. H. Bhadeshia, "Stainless Steels." [Online]. Available: http://www.phase-trans.msm.cam.ac.uk/2005/Stainless_steels/stainless.html (Accessed 2017-11-11).

[39] T.-F. Chen, G. P. Tiwari, Y. Iijima, and K. Yamauchi, "Volume and grain boundary diffusion of chromium in Ni-base Ni–Cr–Fe alloys," *Materials Transactions*, vol. 44, no. 1, pp. 40–46, 2003.

[40] M. Mizouchi, Y. Yamazaki, Y. Iijima, and K. Arioka, "Low Temperature Grain Boundary Diffusion of Chromium in SUS316 and 316L Stainless Steels," *Materials Transactions*, vol. 45, no. 10, pp. 2945–2950, 2004.

[41] J. Keiser, "Compatibility studies of potential molten-salt breeder reactor materials in molten fluoride salts, ORNL/TM-5783," Oak Ridge National Laboratory, Tech. Rep., 1977.

[42] L. C. Olson, R. E. Fuentes, M. J. Martinez-Rodriguez, J. W. Ambrosek, K. Sridharan, M. H. Anderson, B. L. Garcia-Diaz, J. Gray, and T. R. Allen, "Impact of Corrosion Test Container Material in Molten Fluorides," *Journal of Solar Energy Engineering*, vol. 137, no. 6, pp. 061007(1–8), 2015.

[43] U.S. Atomic Energy Commission, "An evaluation of the molten salt breeder reactor," WASH-1222, Tech. Rep., 1972.

[44] J. Keiser, "Status of Tellurium-Hastelloy N Studies in Molten Fluoride Salts, ORNL/TM-6002," Oak Ridge National Laboratory, Tech. Rep., 1977.

[45] L. Walters and M. Edwards, "State of the Art in Cladding and Fuel Channel Material Selection for Canadian SCWR Concept," 2016.

[46] A. Aitkaliyeva, L. He, H. Wen, B. Miller, X. Bai, and T. Allen, "Irradiation effects in Generation IV nuclear reactor materials," in *Structural Materials for Generation IV Nuclear Reactors*. Woodhead Publishing, 2016, ch. 7, pp. 253–283.

[47] G. Muralidharan, D. F. Wilson, L. R. Walker, M. L. Santella, and D. E. Holcomb, "Cladding Alloys for Fluoride Salt Compatibility, ORNL/TM-2010/319," Oak Ridge National Laboratory, Tech. Rep., 2011.

[48] J. A. Lane, H. G. MacPherson, and F. Maslan, "Construction materials for molten-salt reactors," in *Fluid Fuel Reactors*. Addison-Wesley, 1958, ch. 13, pp. 595–625.

[49] M. C. Brupbacher, D. Zhang, W. M. Buchta, M. L. Graybeal, Y. R. Rhim, D. C. Nagle, and J. B. Spicer, "Synthesis and characterization of binder-free Cr_3C_2 coatings on nickel-based alloys for molten fluoride salt corrosion resistance," *Journal of Nuclear Materials*, vol. 461, pp. 215–220, 2015.

[50] M. Rosenthal, R. Briggs, and P. Haubenreich, "Molten-salt reactor program semiannual progress report for period ending August 31, 1971, ORNL-4728," Oak Ridge National Laboratory, Tech. Rep., 1972.

[51] A. C. S. Sabioni, A. M. Huntz, F. Silva, and F. Jomard, "Diffusion of iron in Cr_2O_3: Polycrystals and thin films," *Materials Science and Engineering A*, vol. 392, no. 1-2, pp. 254–261, 2005.

[52] Y. X. Xu, X. T. Luo, C. X. Li, G. J. Yang, and C. J. Li, "Formation of Cr_2O_3 Diffusion Barrier Between Cr-Contained Stainless Steel and Cold-Sprayed Ni Coatings at High Temperature," *Journal of Thermal Spray Technology*, vol. 25, no. 3, pp. 526–534, 2016.

[53] Y. X. Xu, M. Chirol, C. J. Li, and A. Vardelle, "Formation of Al_2O_3 diffusion barrier in cold-sprayed NiCoCrAlY/Ni multi-layered coatings on 304SS substrate," *Surface and Coatings Technology*, vol. 307, pp. 603–609, 2016.

[54] D. Wilson, "Assessment of Nickel Clad Alloy 214 As the Outer Containment Material of a Fission Chamber, ORNL/TM-2014/62," Oak Ridge National Laboratory, Tech. Rep., 2014.

[55] M. P. Short, "The Design of a Functionally Graded Composite for Service in High Temperature Lead and Lead-Bismuth Cooled Nuclear Reactors," PhD Thesis, Massachusetts Institute of Technology, 2010.

[56] M. Martinez-Rodriguez, B. Garcia-Diaz, L. Olson, R. Fuentes, and R. Sindelar, "MAX Phase Materials and Coatings for High Temperature Heat Transfer Applications," Savannah River National Laboratory, Tech. Rep., 2015.

[57] P. Eklund, M. Beckers, U. Jansson, H. Högberg, and L. Hultman, "The $M_{n+1}AX_n$ phases: Materials science and thin film processing," *Thin Solid Films*, vol. 518, no. 8, pp. 1851–1878, 2010.

[58] W.-J. Cheng, R. S. Sellers, M. H. Anderson, K. Sridharan, C.-J. Wang, and T. R. Allen, "Zirconium Effect on the Corrosion Behavior of 316L Stainless Steel Alloy and Hastelloy-N Superalloy in Molten Fluoride Salt," *Nuclear Technology*, vol. 183, no. 2, pp. 248–259, 2013.

[59] W. Gale and T. Totemeir, *Smithells Metal Reference Book*, 8th ed. Elsevier, 2004.

[60] ASME, "Boiler and Pressure Vessel Code - Section II, Part A," 2015.

[61] Aircraft Materials, "Nickel Alloy 201: Technical Data Sheet." [Online]. Available: https://www.aircraftmaterials.com/data/nickel/nickel201.html (Accessed 2017-10-18).

[62] F. Y. Ouyang, C. H. Chang, and J. J. Kai, "Long-term corrosion behaviors of Hastelloy-N and Hastelloy-B3 in moisture-containing molten FLiNaK salt environments," *Journal of Nuclear Materials*, vol. 446, no. 1-3, pp. 81–89, 2014.

[63] Haynes International, "Haynes® 242® Alloy." [Online]. Available: http://www.haynes.ch/doc/haynes/242_h3079.pdf (Accessed 2017-10-18).

[64] J. Engel, H. Bauman, J. Dearing, W. Grimes, E. McCoy, and W. Rhoades, "Conceptual Design Characteristics of a Denatured Molten-Salt Reactor with Once-Through Fuelling, ORNL/TM-7207," Oak Ridge National Laboratory, Tech. Rep., 1980.

[65] National Physical Laboratory, "Calculated Mo–Ni phase diagram," 2010. [Online]. Available: http://resource.npl.co.uk/mtdata/phdiagrams/moni.htm (Accessed 2017-10-18).

[66] J. Halim, R. Abdel-Karim, S. El-Raghy, M. Nabil, and A. Waheed, "Electrodeposition and characterization of nanocrystalline Ni–Mo catalysts for hydrogen production," *Journal of Nanomaterials*, vol. 2012, pp. 845673(1–9), 2012.

[67] E. Chassaing, N. Portail, A.-f. Levy, and G. Wang, "Characterisation of electrodeposited nanocrystalline Ni–Mo alloys," *Journal of Applied Electrochemistry*, vol. 34, pp. 1085–1091, 2004.

[68] C. C. Nee, W. Kim, and R. Weil, "Pulsed Electrodeposition of Ni–Mo Alloys," *Journal of The Electrochemical Society*, vol. 135, no. 5, pp. 1100–1103, 1988.

[69] R. Mousavi, M. E. Bahrololoom, F. Deflorian, and L. Ecco, "Improvement of corrosion resistance of Ni–Mo alloy coatings: Effect of heat treatment," *Applied Surface Science*, vol. 364, pp. 9–14, 2016.

[70] P. De Lima-Neto, A. N. Correia, G. L. Vaz, and P. N. Casciano, "Morphological, structural, microhardness and corrosion characterisations of electrodeposited Ni–Mo and Cr coatings," *Journal of the Brazilian Chemical Society*, vol. 21, no. 10, pp. 1968–1976, 2010.

[71] M. V. Glazoff, I. Charit, and P. Sabharwall, "Computational Thermodynamic Modeling of Hot Corrosion of Alloys Haynes 242 and Hastelloy N for Molten Salt Service in Advanced High Temperature Reactors," *J Nucl Ene Sci Power Generat Technol*, vol. 3:3, 2014.

[72] J. Qiu, Y. Zou, Z. Li, and H. Xu, "Corrosion behaviors of nickel-based high temperature alloys in molten FLiNaK salt," *Nuclear Techniques*, vol. 38, no. 7, pp. 070601(1–6), 2015.

[73] F. Y. Ouyang, C. H. Chang, B. C. You, T. K. Yeh, and J. J. Kai, "Effect of moisture on corrosion of Ni-based alloys in molten alkali fluoride FLiNaK salt environments," *Journal of Nuclear Materials*, vol. 437, no. 1-3, pp. 201–207, 2013.

[74] D. E. Holcomb, G. F. Flanagan, B. W. Patton, J. C. Gehin, R. L. Howard, and T. J. Harrison, "Fast Spectrum Molten Salt Reactor Options, ORNL/TM-2011/105," Oak Ridge National Laboratory, Tech. Rep., 2011.

[75] Haynes International, "Hastelloy® N alloy." [Online]. Available: http://haynesintl.com/docs/default-source/pdfs/new-alloy-brochures/corrosion-resistant-alloys/brochures/n-brochure.pdf?sfvrsn=10 (Accessed 2017-10-18).

[76] V. Ignatiev, "Molten Salts for Safe, Low Waste and Proliferation Resistant Treatment of Radwaste in Accelerator Driven and Critical System," in *Molten Salts: From Fundamentals to Applications*, M. Gaune-Escard, Ed. Springer, 2002, pp. 263–282.

[77] D. E. Clark, R. E. Mizia, M. V. Glazoff, P. Sabharwall, and M. G. McKellar, "Diffusion Welding of Alloys for Molten Salt Service – Status Report, INL/EXT-12-24589," Idaho National Laboratory, Tech. Rep., 2012.

[78] Wikipedia, "File:MoltenSaltReactor.jpg." [Online]. Available: https://upload.wikimedia.org/wikipedia/commons/f/fc/MoltenSaltReactor.jpg (Accessed 2017-11-05).

[79] M. Rosenthal, R. Briggs, and P. Kasten, "Molten-salt reactor program semiannual progress report for period ending August 31, 1972, ORNL-4832," Oak Ridge National Laboratory, Tech. Rep., 1973.

[80] H. Cheng, Z. Li, B. Leng, W. Zhang, F. Han, Y. Jia, and X. Zhou, "Intergranular diffusion and embrittlement of a Ni–16Mo–7Cr alloy in Te vapor environment," *Journal of Nuclear Materials*, vol. 467, pp. 341–348, 2015.

[81] Y. Jia, Z. Li, X. Ye, R. Liu, B. Leng, J. Qiu, M. Liu, and Z. Li, "Effect of Cr contents on the diffusion behavior of Te in Ni-based alloy," *Journal of Nuclear Materials*, vol. 497, pp. 101–106, 2017.

[82] J. W. Koger, "Chromium depletion and void formation in Fe–Ni–Cr alloys during molten salt corrosion and related processes," *Advances in corrosion science and technology*, pp. 245–318, 1974.

[83] ASM, "ASM Handbook Volume 4, Heat Treating," 2001.

[84] B. Weiss and R. Stickler, "Phase instabilities during high temperature exposure of 316 austenitic stainless steel," *Metallurgical Transactions*, vol. 3, no. 4, pp. 851–866, 1972.

[85] M. J. Donachie and S. J. Donachie, *Superalloys: A Technical Guide*, 2nd ed. ASM International, 2002.

[86] High Temp Metals, "Alloy 800/800AT/800H technical data," 2015. [Online]. Available: http://www.hightempmetals.com/techdata/hitempIncoloy800data.php (Accessed 2017-12-24).

[87] W. Hoffelner, *Materials for Nuclear Plants*. Springer, 2013.

[88] G. Y. Lai, *Challenges in Materials Applications for High-Temperature Service*. ASM International, 2007.

[89] U. Bruch, D. Schuhmacher, P. J. Ennis, and E. te Heesen, "Tensile and Impact Properties of Candidate Alloys for High-Temperature Gas-Cooled Reactor Applications," *Nuclear Technology*, vol. 66, no. 2, pp. 357–362, 1984.

[90] W. B. Jones and R. M. Allen, "Mechanical Behavior of Alloy 800 at 838 K," *Metallurgical Transactions A*, vol. 13, no. 4, pp. 637–648, 1982.

[91] R. Gehlbach and H. McCoy Jr., "Phase Instability in Hastelloy N," in *International Symposium on Structural Stability in Superalloys*, Seven Springs, PA, 1968, pp. 346–366.

[92] J. Davis, "Hardfacing, Weld Cladding, and Dissimilar Metal Joining," in *ASM Handbook Volume 6, Welding, Brazing, and Soldering*. ASM International, 1993, pp. 789–829.

[93] R. Srinivasan and C. S. Hartley, "Coextrusion," in *ASM Handbook Volume 14A, Metalworking: Bulk Forming*. ASM International, 2005, pp. 505–515.

[94] Sandvik, "3R12/4L7 Composite tubes for boilers and other boiler applications." [Online]. Available: https://www.materials.sandvik/globalassets/global/downloads/products_downloads/tubular-products/s-1219-ps-eng_3r12_oct_2016.pdf (Accessed 2017-10-15).

[95] R. C. Trucker, "Thermal Spray Coatings," in *ASM Handbook Volume 5, Surface Engineering*. ASM International, 1994, pp. 497–509.

[96] Taskmaster Technologies Inc., "Thermal Spray Coatings." [Online]. Available: http://taskmaster-inc.com/thermal-spray-coatings/ (Accessed 2017-10-17).

[97] C. Sun, L. Li, M. Fu, and Q. Zhou, "Element diffusion model of bimetallic hot deformation in metallurgical bonding process," *Materials and Design*, vol. 94, pp. 433–443, 2016.

[98] G. F. Vander Voort and R. Fowler, "Low-Load Vickers Microindentation," *Advanced Materials and Processes*, vol. 170, no. 4, pp. 28–33, 2012.

[99] J. H. DeVan and R. B. Evans, "Corrosion behavior of reactor materials in fluoride salt mixtures, ORNL-TM-0328," Oak Ridge National Laboratory, Tech. Rep., 1962.

[100] NiDI (Nickel Development Institute), *High-temperature characteristics of stainless steel*. American Iron and Steel Institute, 2014.

[101] F. Yang, W. Tian, H. Nakano, H. Tsuji, S. Oue, and H. Fukushima, "Effect of Current Density and Organic Additives on the Texture and Hardness of Ni Electrodeposited from Sulfamate and Watt's Solutions," *Materials Transactions*, vol. 51, no. 5, pp. 948–956, 2010.

[102] Nihon Kagaku Sangyo Co., "Nickel Sulfamate," 2014. [Online]. Available: http://www.nihonkagakusangyo.co.jp/english/2015/e2.pdf (Accessed 2018-11-18).

[103] M. I. Ansara, T.G. Chart, P.Y. Chevalier, K. Hack, G. McHugh and P. S. Rand, "Phase diagrams for Fe–Cr–Ni based alloys: Part 1. Phase diagrams for binary and ternary alloys of Fe, Cr and Ni with C and with Si, EUR 9657/I/EN," Commission of the European Communities, Tech. Rep., 1985.

[104] L. Olson, "Private communication," 2018.

[105] E. B Pieraggi, "Diffusion and solid state reactions," in *Developments in High Temperature Corrosion and Protection of Materials*, W. Gao and L. Zhengwei, Eds., 2008, ch. 2.

[106] S. F. Cogan, S. Kwon, J. D. Klein, and R. M. Rose, "Fabrication of large diameter external-diffusion processed Nb_3Sn composites," *IEEE Transactions on Magnetics*, vol. 19, no. 3, pp. 1139–1142, 1983.

[107] Terrestrial Energy, "IMSR Technology: How it works." [Online]. Available: https://www.terrestrialenergy.com/technology/how-it-works/ (Accessed 2018-11-17).

Appendix A

Extra diffusion results

A.1 Calculated diffusion coefficients for elements other than chromium

This section includes calculated diffusion coefficients for nickel, iron, and molybdenum for the diffusion couples with Hastelloy N (Tables A.1, A.2, and A.3), and calculated diffusion coefficients for nickel and iron for the Ni-plated samples (Table A.4 and A.5). The calculated diffusion coefficients in Sections 4.3 and 4.5 are only for chromium.

Manganese was one of the elements whose concentration was measured in EDS line scans of diffusion couples with SS316L because it is more than 1 wt% of SS316L and not including it would have resulted in non-negligible error from the normalization of concentration data to 100%. However, manganese diffusion coefficients are not included here because manganese concentration data was too scattered for calculated diffusion coefficients to be of any use.

For the calculation of molybdenum diffusion coefficients, several of the curve fits were visibly wrong due to spikes in molybdenum enrichment at the diffusion couple interfaces. In order to correct this, the molybdenum concentration data outliers (generally at interfaces) were manually excluded for curve fitting.

The diffusion coefficients in the section were calculated with the assumptions of type A diffusion kinetic regime, microstructural homogeneity (single phase), and concentration-independence. The extent to which these assumptions are valid is discussed in Chapter 5.

Table A.1: Nickel diffusion coefficients D_{Ni} for diffusion couples thermally aged at 700 °C for 1460 h and 5840 h, and $D_{Ni}t$ term for 2 h bonding at 900 °C, calculated from EDS line scan data. Uncertainties are 95% confidence intervals, and the values in the parentheses are average r-squared values from the curve fits.

Alloy combination	$D_{Ni}t$ [m^2] (bonding)	D_{Ni} [$m^2\,s^{-1}$] (700 °C)	
		1460 h	5840 h
800H/Hastelloy N	8.5E-13±1.3E-13 (0.99)	3.8E-20±2.9E-20 (0.93)	1.1E-19±1.1E-20 (0.99)
SS316L/Hastelloy N	7.6E-13±1.6E-13 (0.99)	1.6E-20±3.3E-20 (0.99)	7.7E-20±1.6E-20 (0.99)

Table A.2: Iron diffusion coefficients D_{Fe} for diffusion couples thermally aged at 700 °C for 1460 h and 5840 h, and $D_{Fe}t$ term for 2 h bonding at 900 °C, calculated from EDS line scan data. Uncertainties are 95% confidence intervals, and the values in the parentheses are average r-squared values from the curve fits.

Alloy combination	$D_{Fe}t$ [m^2] (bonding)	D_{Fe} [$m^2\,s^{-1}$] (700 °C)	
		1460 h	5840 h
800H/Hastelloy N	9.2E-13±1.0E-13 (1.00)	6.5E-20±2.2E-20 (1.00)	1.1E-19±7.8E-21 (0.99)
SS316L/Hastelloy N	7.5E-13±7.5E-13 (1.00)	7.2E-20±2.3E-20 (0.99)	7.7E-20±1.2E-20 (0.99)

Table A.3: Molybdenum diffusion coefficients D_{Mo} for diffusion couples thermally aged at 700 °C for 1460 h and 5840 h, and $D_{Mo}t$ term for 2 h bonding at 900 °C, calculated from EDS line scan data. Uncertainties are 95% confidence intervals, and the values in the parentheses are average r-squared values from the curve fits.

Alloy combination	$D_{Mo}t$ [m^2] (bonding)	D_{Mo} [$m^2\,s^{-1}$] (700 °C)	
		1460 h	5840 h
800H/Hastelloy N	1.2E-12±2.7E-13 (0.98)	6.4E-20±5.7E-20 (0.97)	4.7E-20±1.6E-20 (0.98)
SS316L/Hastelloy N	1.1E-12±1.9E-13 (0.97)	6.0E-19±1.2E-19 (0.91)	4.3E-20±3.1E-20 (0.98)

Table A.4: Nickel diffusion coefficients D_{Ni} for Ni-plated samples aged at 700 °C for 3855 h, calculated from EDS line scan data. Uncertainties are 95% confidence intervals, and the values in the parentheses are average r-squared values from the curve fits.

Material combination	D_{Cr} [$m^2\,s^{-1}$] (700 °C)	
	1461 h	3855 h
800H/Ni plating	5.5E-17±8.0E-18 (0.97)	2.0E-17±3.6E-18 (0.97)
SS316L/Ni plating	2.6E-17±4.0E-18 (0.99)	1.6E-17±2.5E-18 (0.99)

Table A.5: Iron diffusion coefficients D_{Fe} for Ni-plated samples aged at 700 °C for 3855 h, calculated from EDS line scan data. Uncertainties are 95% confidence intervals, and the values in the parentheses are average r-squared values from the curve fits.

Material combination	D_{Cr} [$m^2 s^{-1}$] (700 °C)	
	1461 h	3855 h
800H/Ni plating	5.1E-17±7.3E-18 (0.98)	2.0E-17±3.4E-18 (0.97)
SS316L/Ni plating	2.6E-17±3.9E-18 (0.99)	1.6E-17±2.3E-18 (0.98)

A.2 Extrapolation of diffusion results to an end-of-reactor-lifetime for elements other than chromium

The diffusion extrapolation results in Chapter 5 are specific to chromium, whereas the diffusion extrapolation results in this section include elements other than chromium. Figures A.1 and A.2 include diffusion model extrapolation results for all the alloying elements whose diffusion coefficients were calculated from EDS line scans (for the diffusion couples with Hastelloy N, the diffusion coefficients are included in Tables 4.1, A.1, A.2, and A.3, and for the Ni-plated samples, the diffusion coefficients are included in Tables 4.2, A.4, and A.5). Figures A.3, A.4, and A.5 include simulation extrapolation results for elements other than chromium that were included in simulations. The erratic shape of the concentration profiles in Figure A.5 for low-concentration elements (manganese, molybdenum, titanium, and aluminum) is a good example of the dependence of diffusion on activity (i.e. chemical potential) rather than concentration, since corresponding activity profiles were plotted and observed to be consistently downward-sloped towards the righthand side, as one would expect, given

the absence of these elements in Ni plating. However, there were some exceptions: for the activity profiles of some elements for some cladding thicknesses, there was slight upward slope towards the righthand side at the outer edge of the claddings as a result of leached chromium being replaced with nickel.

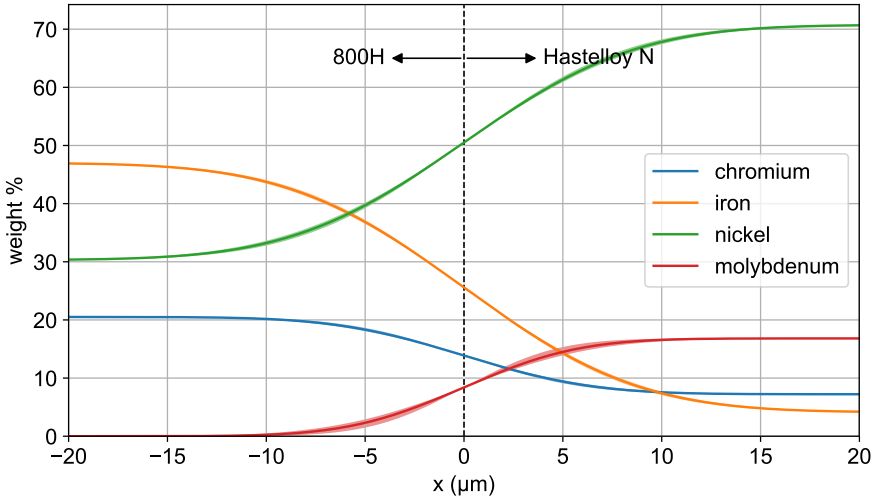

(a) 800H/Hastelloy N.

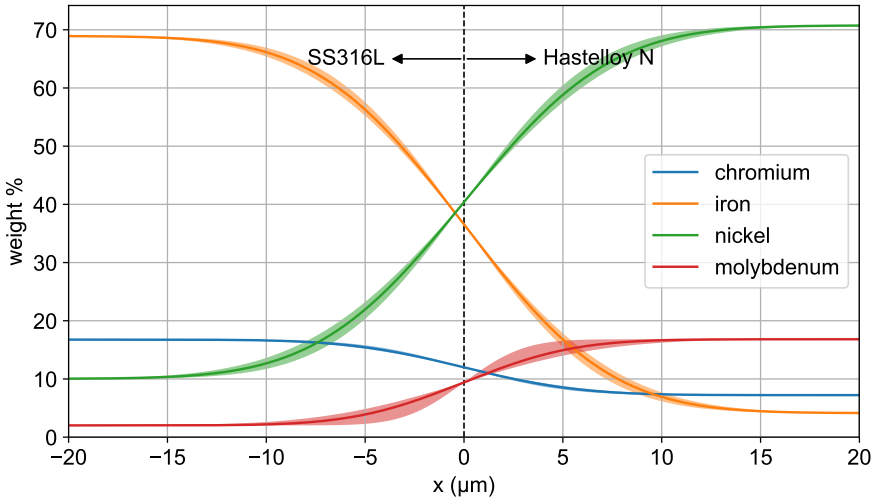

(b) SS316L/Hastelloy N.

Figure A.1: Extrapolated concentration profiles for 7 years of aging at 700 °C for 800H/ Hastelloy N and SS316L/Hastelloy N diffusion couples. The dark lines in the middle of the bands were calculated with average diffusion coefficients for 5840 h of aging. The upper and lower bounds of the pale bands were calculated with the upper and lower limits of the diffusion coefficients, based on their 95% confidence intervals.

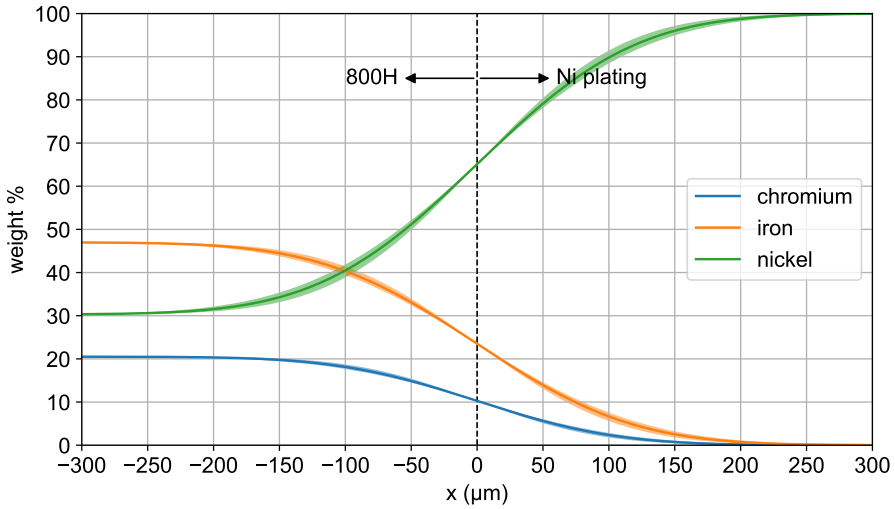

(a) 800H/Ni plating.

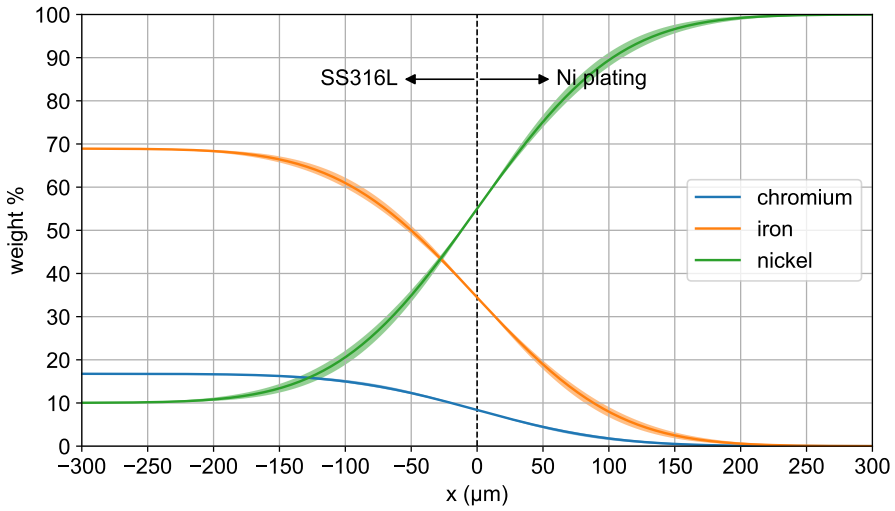

(b) SS316L/Ni plating.

Figure A.2: Extrapolated concentration profiles for 7 years of aging at 700 °C for 800H/Ni plating and SS316L/Ni plating. The dark lines in the middle of the bands were calculated with average diffusion coefficients for 3855 h of aging. The upper and lower bounds of the pale bands were calculated with the upper and lower limits of the diffusion coefficients, based on their 95% confidence intervals.

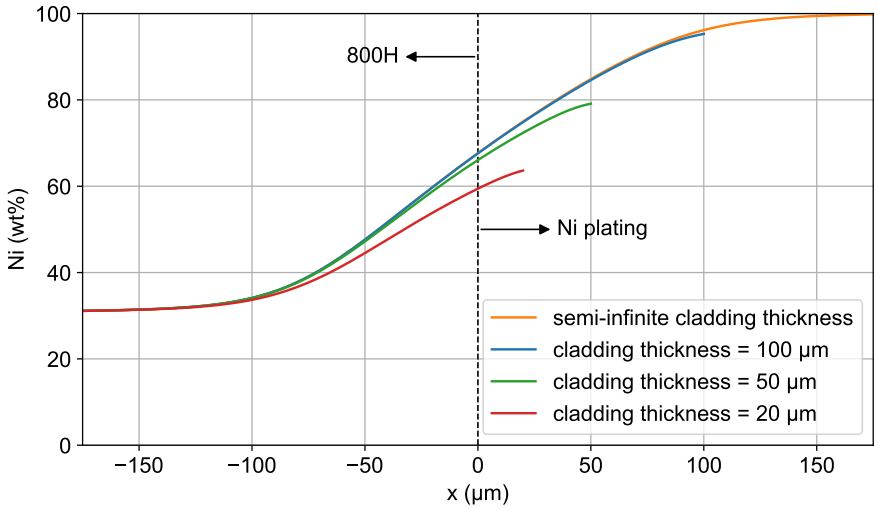

(a) 800H/Ni plating.

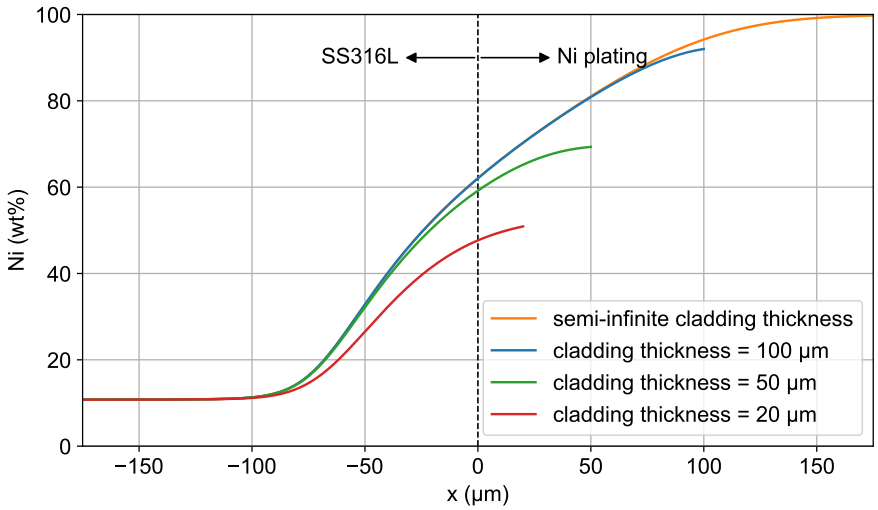

(b) SS316L/Ni plating.

Figure A.3: Extrapolations of nickel diffusion to seven years for varied cladding thickness. A salt–cladding interface boundary condition of near-zero chromium concentration is conservatively assumed.

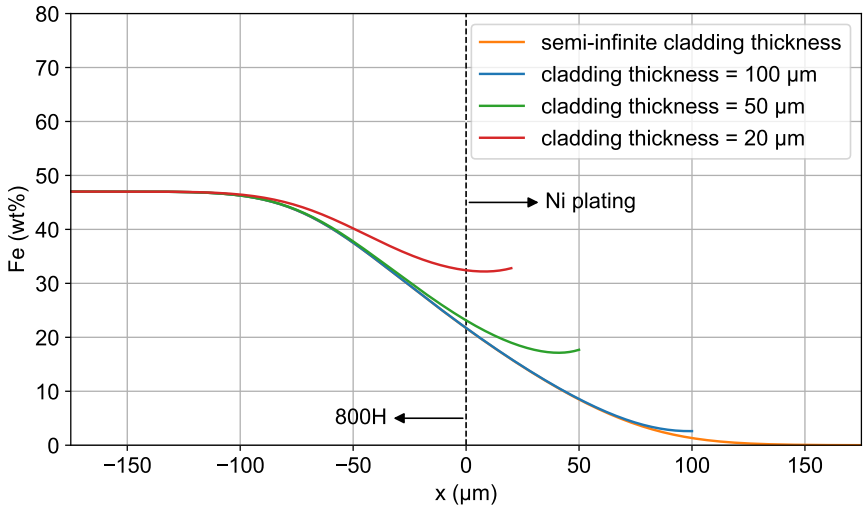

(a) 800H/Ni plating.

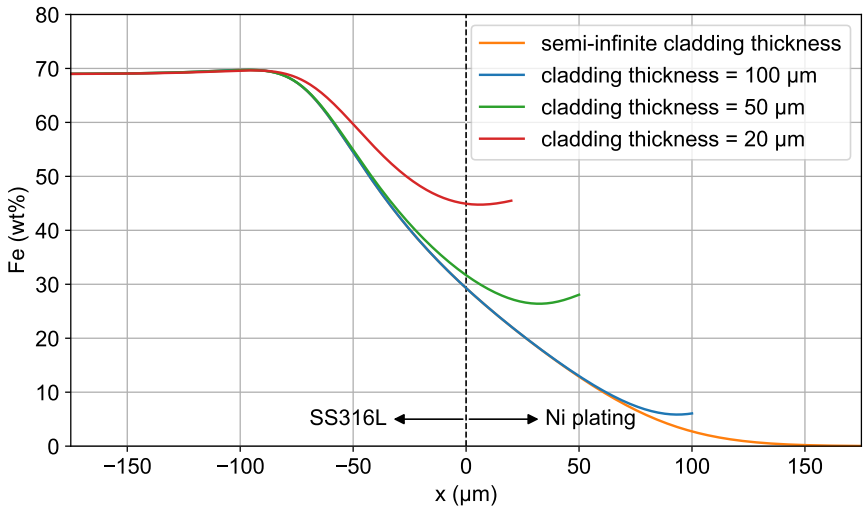

(b) SS316L/Ni plating.

Figure A.4: Extrapolations of iron diffusion to seven years for varied cladding thickness. A salt–cladding interface boundary condition of near-zero chromium concentration is conservatively assumed.

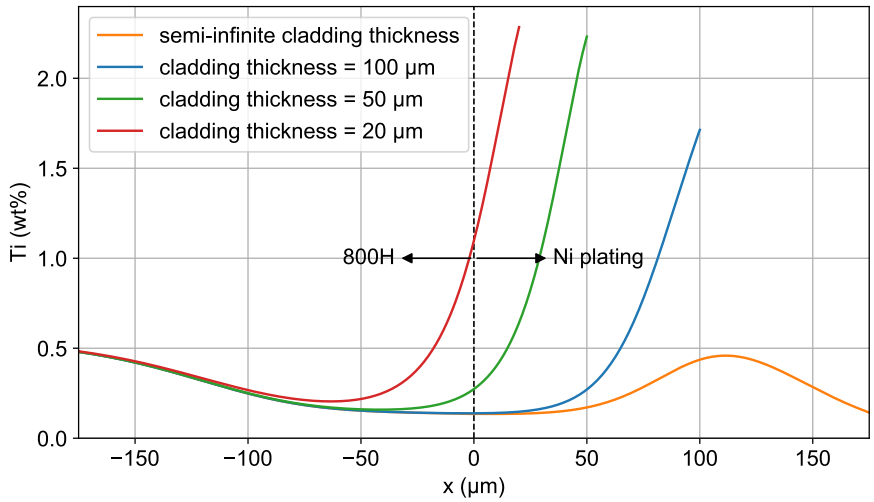

(a) 800H/Ni plating: titanium.

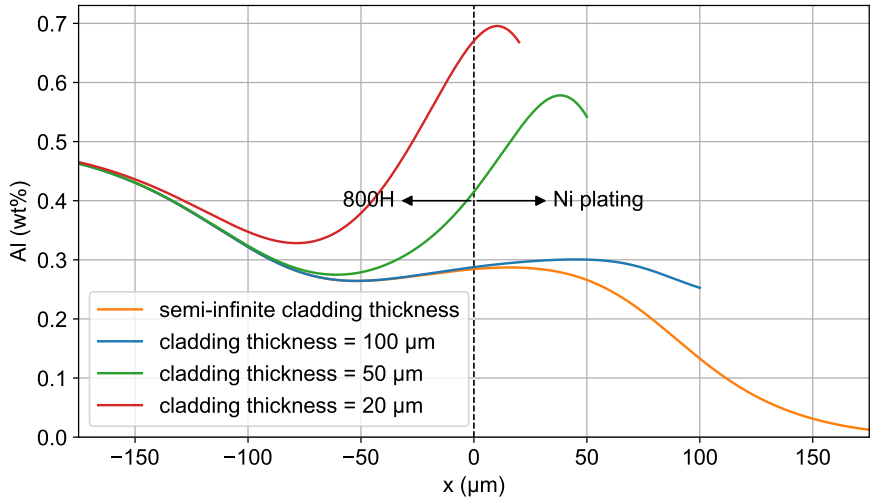

(b) 800H/Ni plating: aluminum.

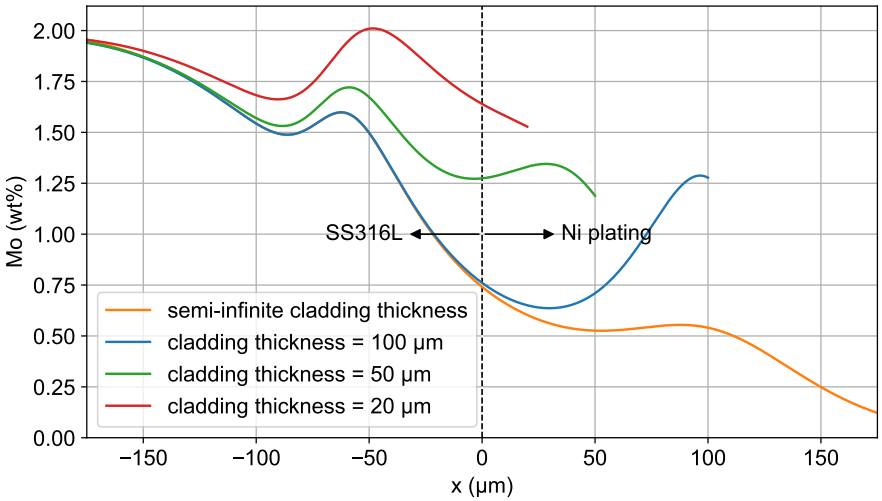

(c) SS316L/Ni plating: molybdenum.

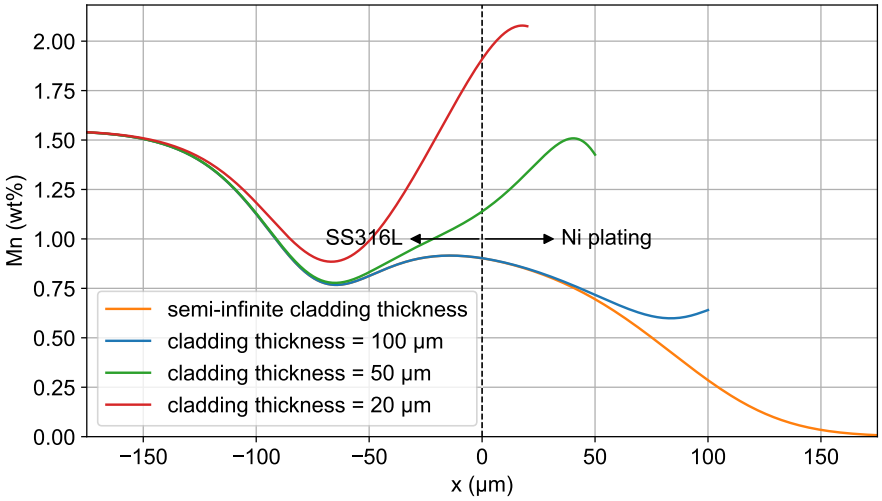

(d) SS316L/Ni plating: manganese.

Figure A.5: Extrapolation of low-concentration element diffusion to seven years for varied cladding thickness. A salt–cladding interface boundary condition of near-zero chromium concentration is conservatively assumed.

A.3 Comparison of concentration profiles

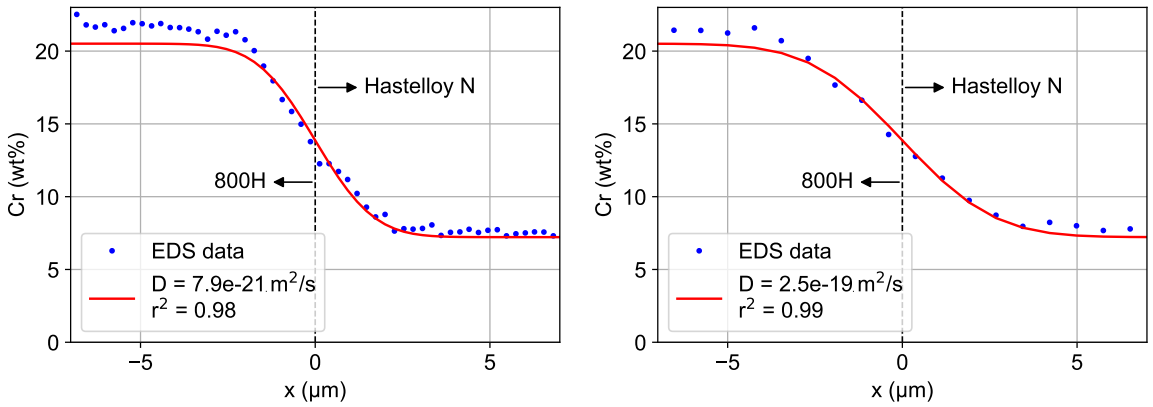

(a) 1460-hour-aged.

(b) 5840-hour-aged.

Figure A.6: Comparison of chromium concentration profiles from EDS line scans of 1460- and 5840-hour aged 800H/Hastelloy N diffusion couples, showing that these concentration profiles are qualitatively the same.

Appendix B

Results for diffusion couples with Ni 200

Ni 200 would not be used in MSRs because of its high carbon content and the resulting graphite and carbide precipitation at high temperatures. The experimental results presented here were collected because an incorrect mill cert was provided by the supplier leading to the false assumption that the carbon concentration in the Ni 200 alloy in this study was 0.01 wt%, which is within the specifications for Ni 201, an alloy that—unlike Ni 200—could be used in MSRs. It was later discovered that the actual carbon concentration in the Ni 200 alloy in this study is 0.05 wt%, which is not within the specifications for Ni 201.

The problem that resulted from the use of Ni 200 with 0.05 wt% carbon is that the carbon activity in this alloy is significantly greater than in the 800H and SS316L structural alloys to which it was diffusion bonded. As a result, carbon diffused from the Ni 200 into the structural alloys during diffusion bonding and thermal aging, causing chromium carbide precipitates to form in the structural alloys towards the interfaces of the diffusion couples. These precipitates caused significant interfacial embrittlement in both 800H/Ni 200 and SS316L/Ni 200, which would definitely be undesirable in reactor components.

After observing the presence of carbides and subsequently having an independent carbon concentration measurement done which revealed the supplier's mistake, the results for diffusion couples with Ni 200 were moved to this appendix section but not removed entirely

because they retain value as an example of the importance of avoiding cladding materials with more carbon activity than in underlying structural alloys and of the importance of proper cleaning of structural alloys prior to cladding fabrication (given that residue from improper cleaning is another potential source of carbon).

B.1 Initial testing of Ni 200

An optical micrograph and a surface profile (bonding surface) of as-received Ni 200 are shown in Figure B.1. The corresponding optical micrographs and surface profiles for the 800H and SS316L structural alloys to which the Ni 200 was bonded are shown in Section 4.1.

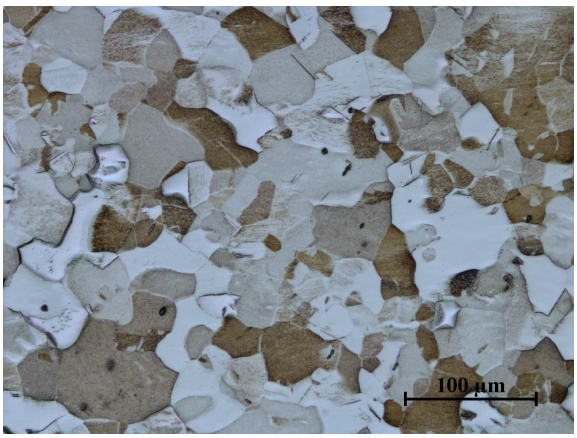

(a) Optical micrograph of Ni 200, 200x. Etched in aqua regia.

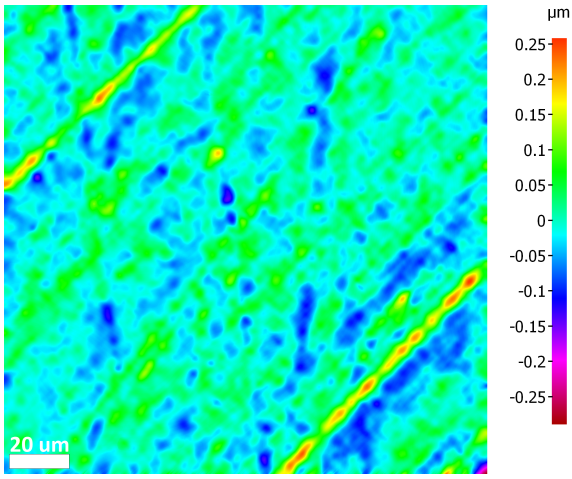

(b) Surface profile. Average height: 0.030 µm.

Figure B.1: Optical micrograph and surface profile (bonding surface) of as-received Ni 200. The average height value was calculated based on the ISO 4287 standard.

B.2 Microstructure in 800H/Ni 200 and SS316L/Ni 200 diffusion couples

Table B.1 summarizes the main microstructure observations for diffusion couples with Ni 200. The analysis results behind these observations are presented in this section.

Table B.1: Main microstructure observations for the 800H/Ni 200 and SS316L/Ni 200 diffusion couples.

	800H	**SS316L**
Ni 200	• Formation of *intragranular* precipitates in 800H towards the interface during diffusion bonding and thermal aging. • Formation of small grains at the interface during diffusion bonding and thermal aging.	• Grain growth in bulk SS316L (away from the interface) during diffusion bonding. • Formation of *intergranular* precipitates in SS316L towards the interface during diffusion bonding, which most likely pinned grain boundaries are prevented grain growth.

Microhardness profiles for as-received, diffusion bonded, and thermally aged 800H/ Ni 200 are shown in Figure B.2. The main observations from these microhardness profiles are the following: (1) an increase in hardness of 800H towards the interface during diffusion bonding and during initial thermal aging, and (2) a decrease in hardness of bulk Ni 200 primarily during diffusion bonding. The gradient in hardness on the 800H side is due to intragranular precipitates, whose density gradient towards the interface can be clearly seen in Figure B.3. The decrease in hardness of bulk Ni 200 is due to grain growth, based on results of grain size analysis that aren't shown here.

The results of EDS point scans of precipitates near the interface of 1460-hour-aged 800H/ Ni 200 are shown in Figure B.4. The composition results show that the intragranular precipitates are carbon- and chromium-rich, indicating that they are chromium carbides ($Cr_{23}C_6$), which is consistent with the TTT diagram in Figure 2.18. The intergranular precipitates are also most likely chromium carbides, but there is no evidence that these formed preferentially towards the interface. Emphasis is placed on the intragranular precipitates because these are the main contributor to the measured increase in hardness towards the interface. These

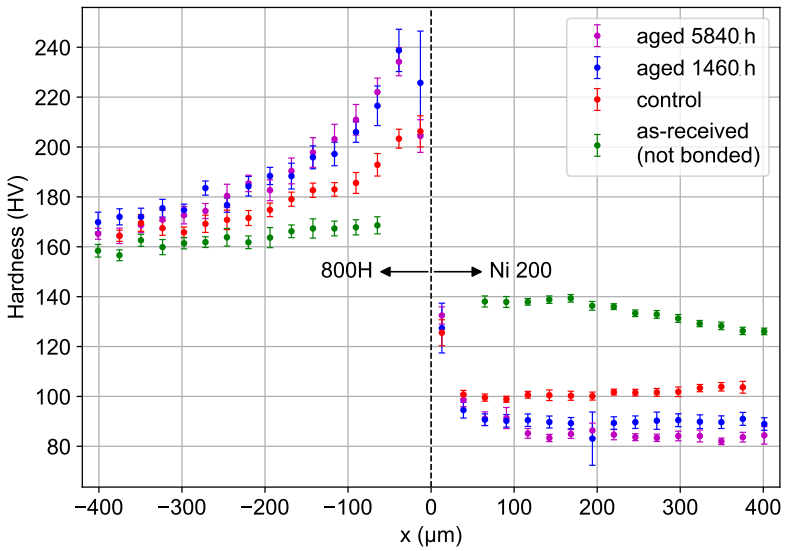

Figure B.2: Microhardness profiles of as-received alloys and 800H/Ni 200 diffusion couples, with a dashed line marking the interface.

carbides formed due to diffusion of carbon from Ni 200, which has significantly greater carbon activity than the 800H.

It can be seen from Figure B.5 that small interfacial grains formed during diffusion bonding and may have grown during thermal aging. At diffusion bonded interfaces, recrystallization and grain overlap are desirable because these are confirmations of metallurgical bonding. It would be undesirable if these grains are intermetallics because this could mean embrittlement, but based on the composition in the interfacial grains and the phase diagram in Figure 5.2, they should be austenitic at equilibrium.

Microhardness profiles for as-received, diffusion bonded, and thermally aged SS316L/ Ni 200 are shown in Figure B.6. The main observations from these microhardness profiles are the following: (1) an increase in hardness of SS316L towards the interface during diffusion bonding and initial thermal aging, (2) a decrease in hardness of the bulk SS316L during diffusion bonding, followed by a slight increase in hardness during thermal aging, and (3) a decrease in hardness of Ni 200 during diffusion bonding and thermal aging. Grain growth occurred in the SS316L except near the interface, where intergranular precipitates most

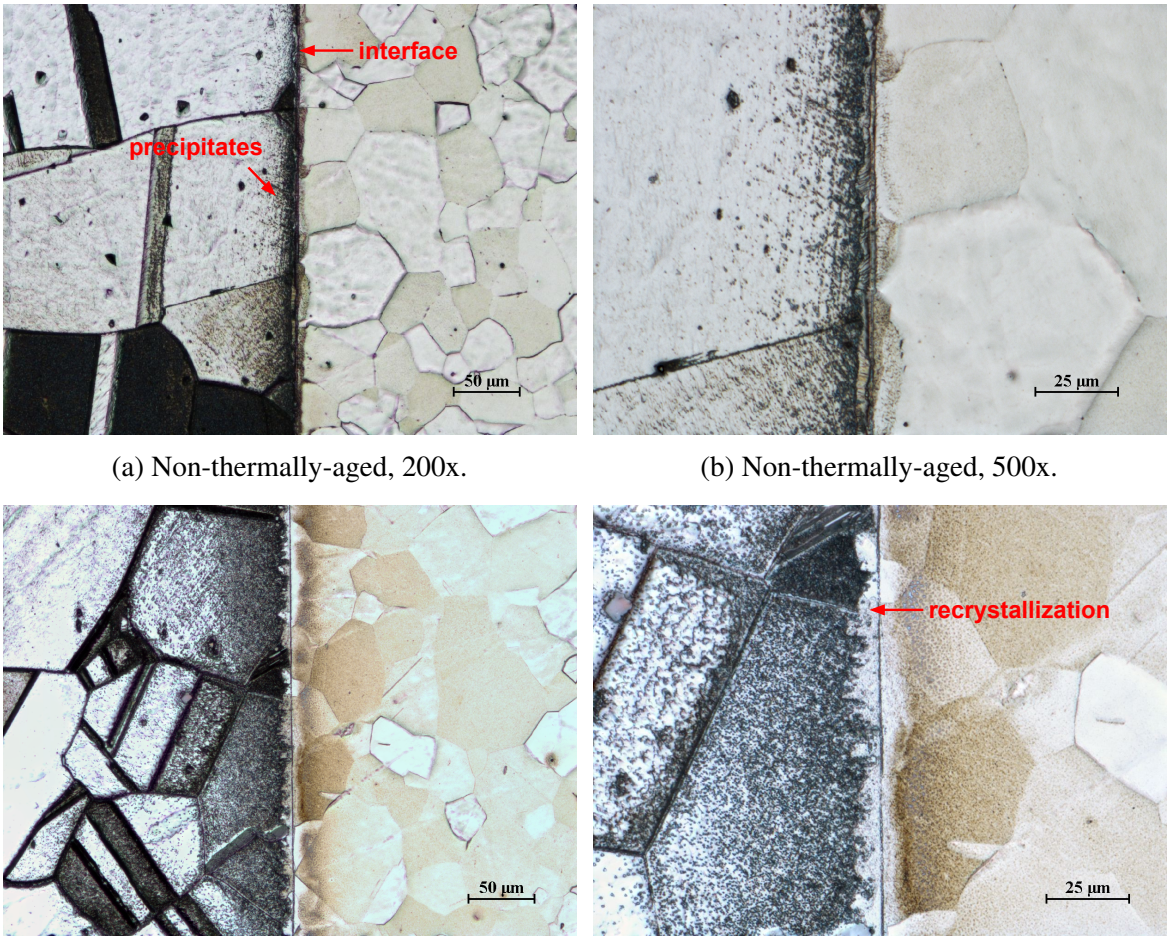

(a) Non-thermally-aged, 200x.

(b) Non-thermally-aged, 500x.

(c) 1460-hour-aged, 200x.

(d) 1460-hour-aged, 500x.

Figure B.3: Optical micrographs of 800H/Ni 200 diffusion couples etched in aqua regia.

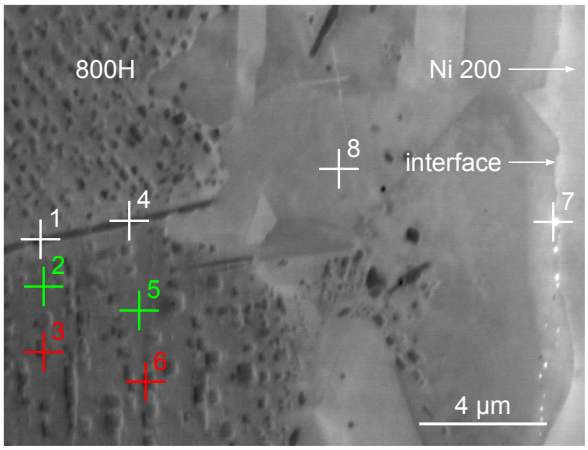

Point	C	Cr	Fe	Ni
1	2.5	47.3	32.0	16.2
2	0.8	12.4	51.1	33.0
3	2.3	53.0	29.4	13.2
4	2.5	46.4	31.8	17.4
5	0.6	14.3	49.6	33.3
6	2.8	54.3	27.8	13.1
7	0.4	8.5	22.2	66.2
8	0.5	9.8	27.0	61.3

Red: Intragranular precipitates
Green: Adjacent matrix

Figure B.4: EDS point scans of precipitates and the matrix in 800H near the interface of a 1460-hour-aged 800H/Ni 200 diffusion couple. Concentrations of the elements Mn, Al, Ti, and Si are omitted because they are small and did not vary significantly. The SEM image was taken in SE mode, 10,000x.

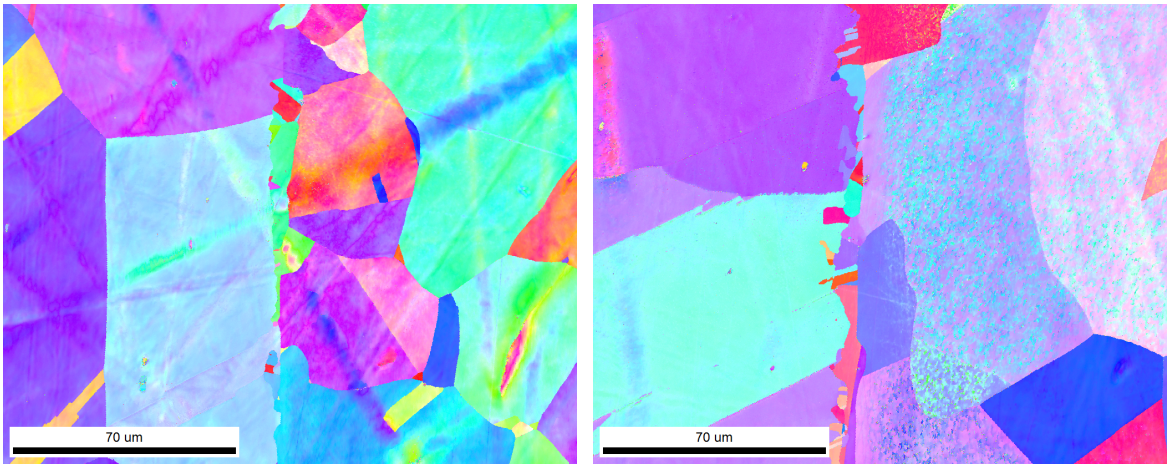

(a) Non-thermally-aged.

(b) 1460-hour-aged.

Figure B.5: EBSD maps of 800H/Ni 200 diffusion couples, 1000x, showing presence of small recrystallized grains at the bonded interfaces. There was drift during data collection, causing these maps to be slightly curved towards the right. The crossing lines in the map on the left are from sub-surface damage—a consequence of imperfect sample polishing.

likely pinned the grain boundaries. The similarity in grain size between as-received SS316L and diffusion bonded SS316L near its interface with Ni 200 is shown in Figure B.8. The distribution of grain size and precipitates in the SS316L can be seen in Figure B.7. The cause of the increase in hardness in SS316L towards the interface is probably a combination of the precipitates and smaller grain size. The cause of the decrease in hardness in the bulk Ni 200 is grain growth, similarly to what was stated earlier for 800H/Ni 200.

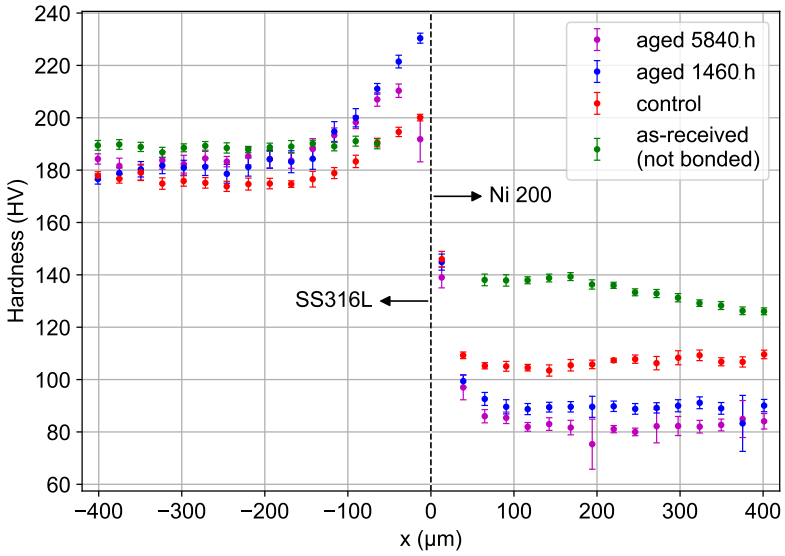

Figure B.6: Microhardness profiles of as-received alloys and SS316L/Ni 200 diffusion couples, with a dashed line marking the interface.

The result of EDS point scans of precipitates near the interface of 1460-hour-aged SS316L/Ni 200 are shown in Figure B.9. These results show a significant increase in chromium, molybdenum, and carbon, and a decrease in iron and nickel at the precipitates, suggesting that the precipitates are primarily carbides. Similar EDS results but for precipitates in bulk SS316L bonded to Ni 200 are shown in Figure B.10, in this case showing less carbon enrichment and more molybdenum enrichment, suggesting that the precipitates are primarily intermetallics, based on the compositions for intermetallics in SS316L/316 in [84, p. 854]. From these two sets of EDS point scan analysis and the relatively high carbon activity in the Ni 200, it is expected that chromium carbides formed in the SS316L, similarly to what

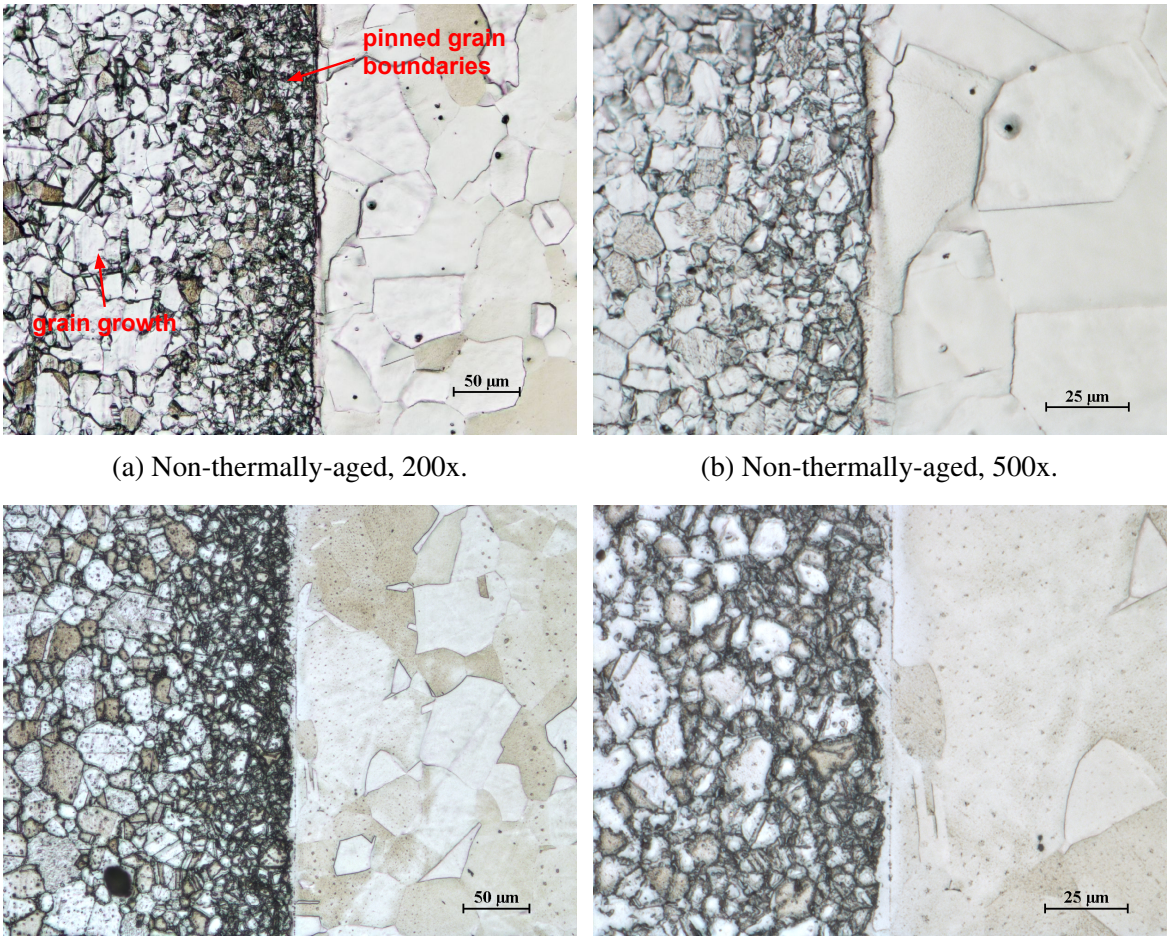

(a) Non-thermally-aged, 200x.

(b) Non-thermally-aged, 500x.

(c) 1460-hour-aged, 200x.

(d) 1460-hour-aged, 500x.

Figure B.7: Optical micrographs of SS316L/Ni 200 diffusion couples etched in aqua regia.

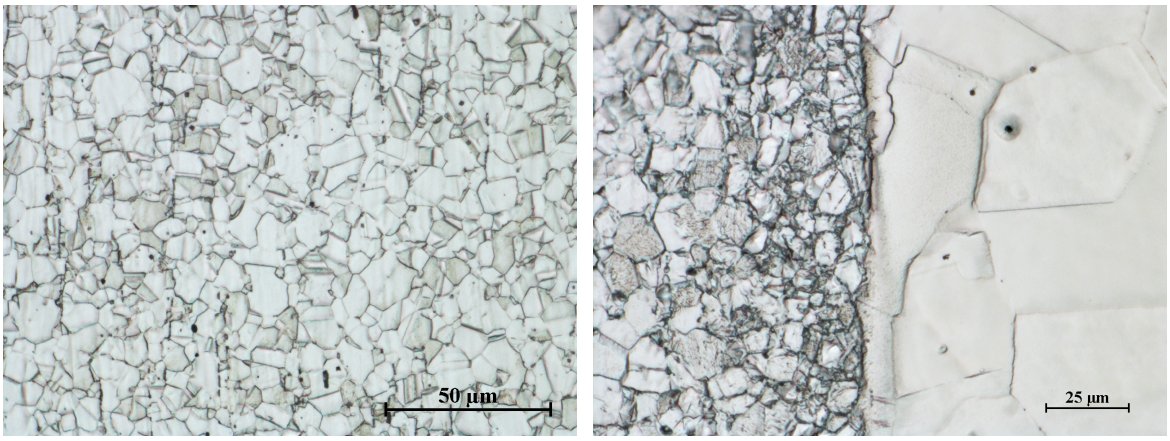

(a) (b)

Figure B.8: Optical micrographs of (a) as-received SS316L and (b) non-thermally-aged SS316L/Ni 200 (same image as Figure B.7b), both etched in aqua regia, 500x. This side-by-side comparison shows that the grain size of SS316L near the interface of SS316L/Ni 200 visually matches that of the as-received SS316L.

occurred in the 800H bonded to Ni 200, except that they formed primarily at grain boundaries rather than within grains. This explains the observed lack of grain growth near the interface in SS316L bonded to Ni 200 because the intergranular precipitates most likely pinned grain boundaries and prevented grain growth.

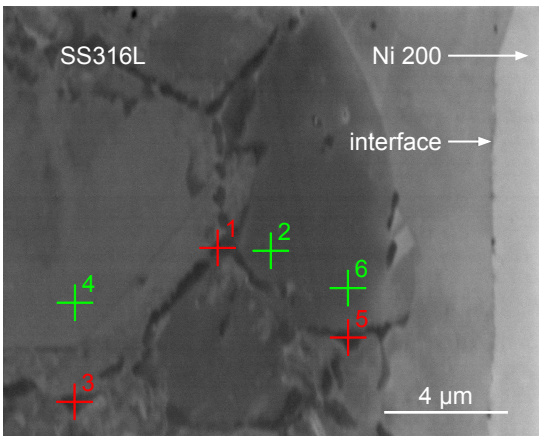

Point	C	Mo	Cr	Mn	Fe	Ni
1	2.6	6.5	46.7	0.8	38.7	4.7
2	1.0	1.3	14.2	1.5	71.2	10.7
3	2.8	6.3	43.9	1.0	41.3	4.8
4	0.9	1.8	16.8	1.6	68.8	10.1
5	2.8	6.2	45.5	0.6	37.2	7.8
6	0.8	1.4	14.1	0.8	72.2	10.7

Red: Intergranular precipitates
Green: Adjacent matrix

Figure B.9: EDS point scans of intergranular precipitates and the matrix in SS316L near the interface of a 1460-hour-aged SS316L/Ni 200 diffusion couple. The SEM image was taken in SE mode, 10 000x.

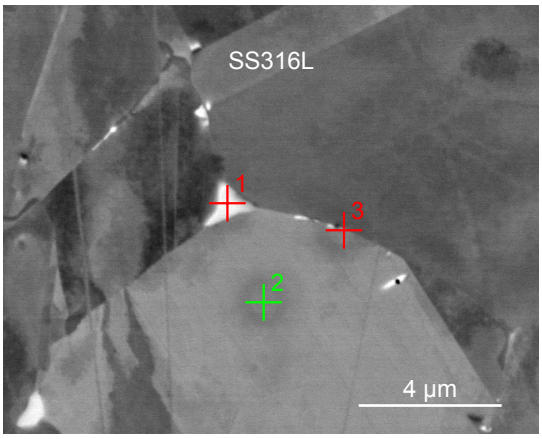

Point	C	Mo	Cr	Mn	Fe	Ni
1	0.8	14.3	22.5	1.2	57.2	4.1
2	0.7	1.9	16.9	1.3	69.7	9.5
3	0.7	2.3	16.2	1.3	69.6	9.9

Red: Intergranular precipitates
Green: Adjacent matrix

Figure B.10: EDS point scans of intergranular precipitate and the matrix in bulk SS316L of a 1460-hour-aged SS316L/Ni 200 diffusion couple. The SEM image was taken in BSE mode, 10 000x.

B.3 Diffusion in 800H/Ni 200 and SS316L/Ni 200 diffusion couples

Typical EDS line scan results for non-thermally-aged and 1460-hour-aged 800H/Ni 200 diffusion couples are shown in Figures B.11 and B.12, respectively. The spikes in chromium concentration in Figure B.12 are due to intragranular chromium carbides, and by examining the shape of the measured concentration profiles, it becomes apparent that these carbides acted as a diffusion barrier. This is consistent with the fact that diffusion in carbides tends to be slow. Also, the precipitate-free layer of grains that grew at the interface on the 800H side is visible in the SEM-BSE images, with the EDS data revealing nearly homogeneous chromium concentration.

Typical EDS line scan results for SS316L/Ni 200 are shown in Figures B.13 and B.14. The spikes in chromium concentration in Figure B.14 are due to chromium-rich intergranular precipitates (primarily carbides, as discussed in Section B.2). Similarly to the effect of the intragranular precipitates on diffusion in 800H/Ni 200, the precipitates in SS316L/Ni 200 slowed diffusion.

Calculated chromium diffusion coefficients for the 800H/Ni 200 and SS316L/Ni 200 diffusion couples are included in Table B.2. The smaller values of these coefficients compared to those in Table 4.2 for Ni-plated samples is probably due to a combination of the larger grain size in Ni 200 and the precipitates in the structural alloys bonded to Ni 200, which did not form in the Ni-plated structural alloys (due to there being less carbon in the Ni plating). However, there is probably considerably more systematic error in the diffusion coefficients in Table B.2 because, based on the significant presence of precipitates, it is inaccurate to assume presence of a single phase, which is required for the use of Equations 2.12 and 2.13. Diffusion coefficients for other elements than chromium and results of diffusion extrapolations are not shown because of their limited usefulness.

Table B.2: Chromium diffusion coefficients D_{Cr} for diffusion couples thermally aged at 700 °C for 1460 h and 5840 h, and $D_{Cr}t$ term for 2 h bonding at 900 °C, calculated from EDS line scan data. Uncertainties are 95% confidence intervals, and the values in the parentheses are average r-squared values from the curve fits.

Alloy combination	$D_{Cr}t$ [m^2] (bonding)	D_{Cr} [$m^2\,s^{-1}$] (700 °C)	
		1460 h	5840 h
800H/Ni 200	6.5E-12±1.2E-12 (0.92)	1.3E-18±6.3E-19 (0.75)	2.8E-18±5.3E-19 (0.82)
SS316L/Ni 200	7.7E-12±1.1E-12 (0.94)	1.7E-18±5.5E-19 (0.65)	2.8E-18±5.6E-19 (0.79)

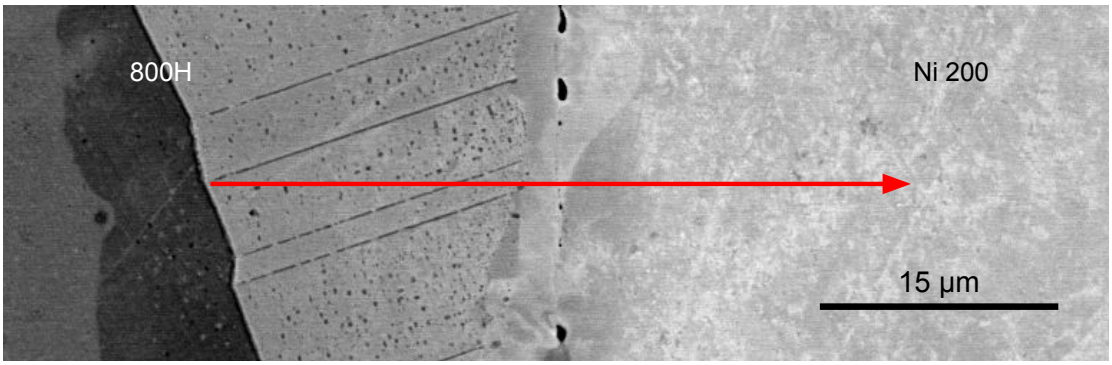

(a) SEM-BSE image of EDS line scan path.

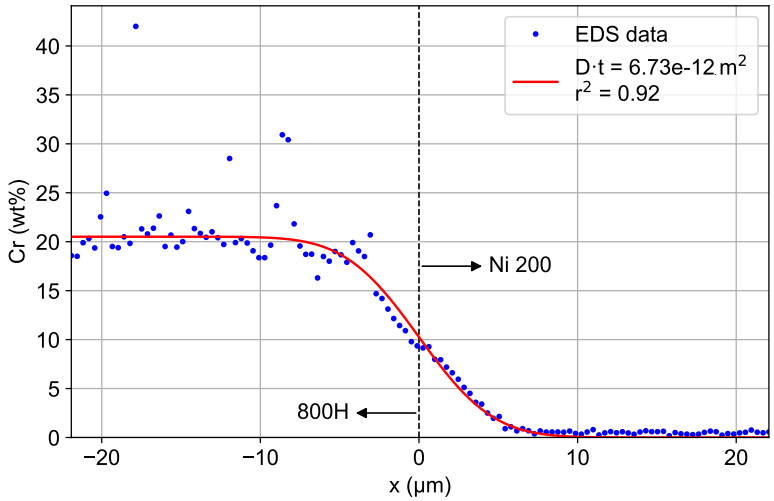

(b) Curve fit of chromium EDS data.

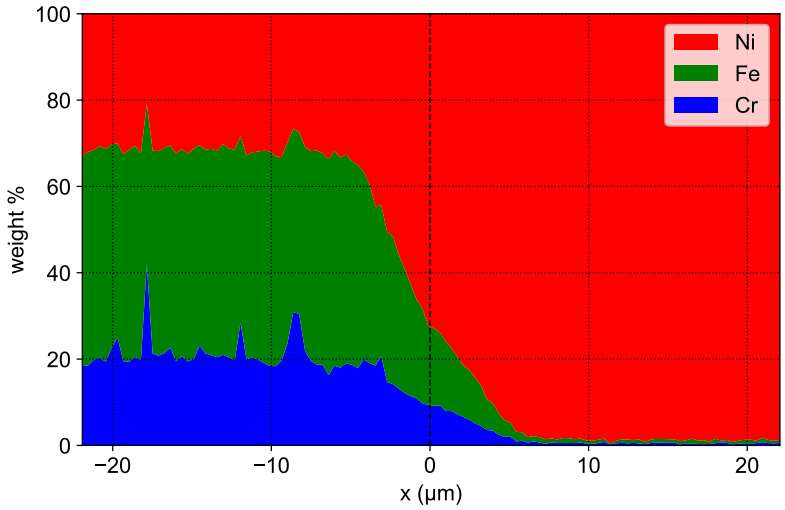

(c) Stacked area plot of major elements (>1wt%)

Figure B.11: Typical EDS line scan data and curve fit for non-thermally-aged 800H/Ni 200 diffusion couples.

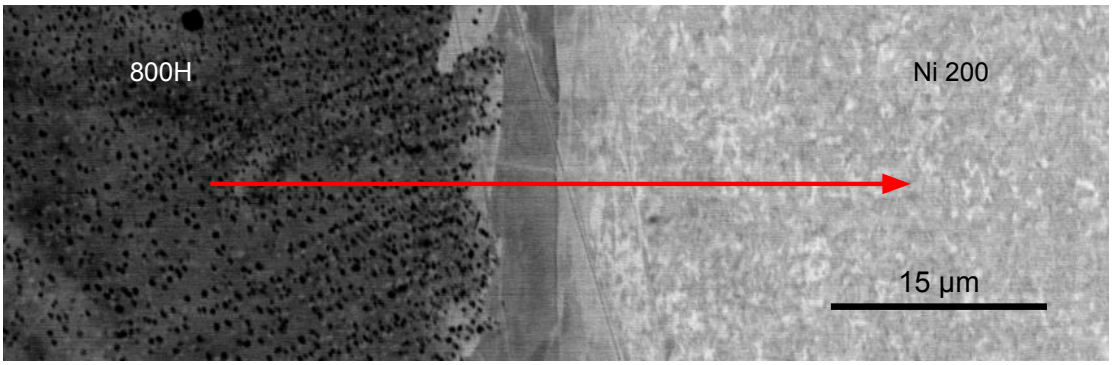

(a) SEM-BSE image of EDS line scan path.

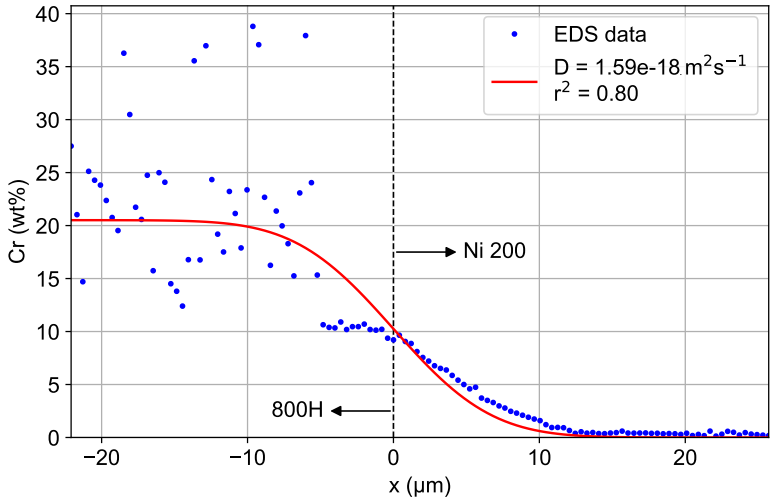

(b) Curve fit of chromium EDS data.

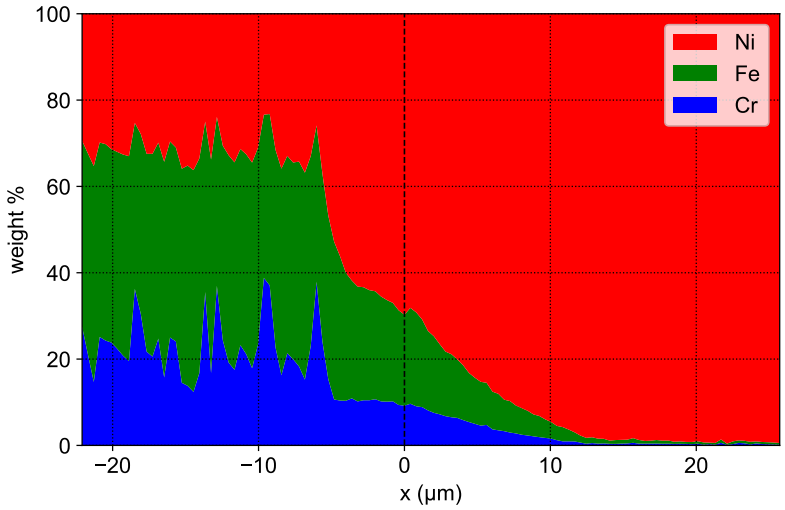

(c) Stacked area plot of major elements (>1wt%)

Figure B.12: Typical EDS line scan data and curve fit for 1460-hour-aged 800H/Ni 200 diffusion couples.

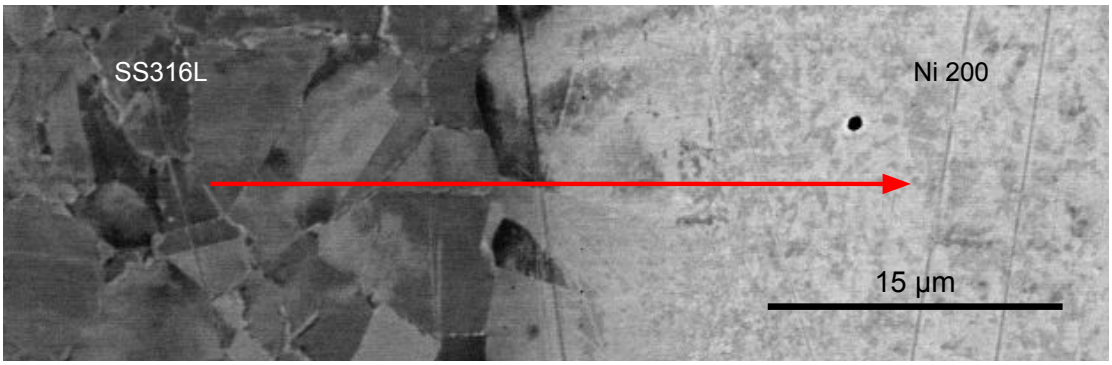

(a) SEM-BSE image of EDS line scan path.

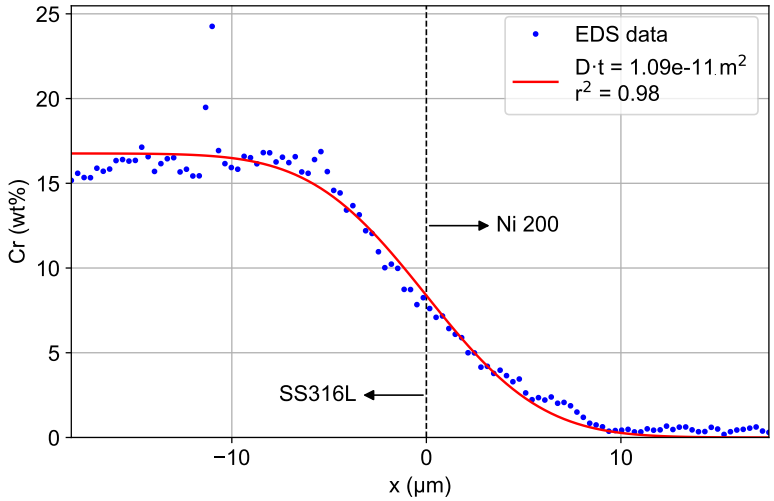

(b) Curve fit of chromium EDS data.

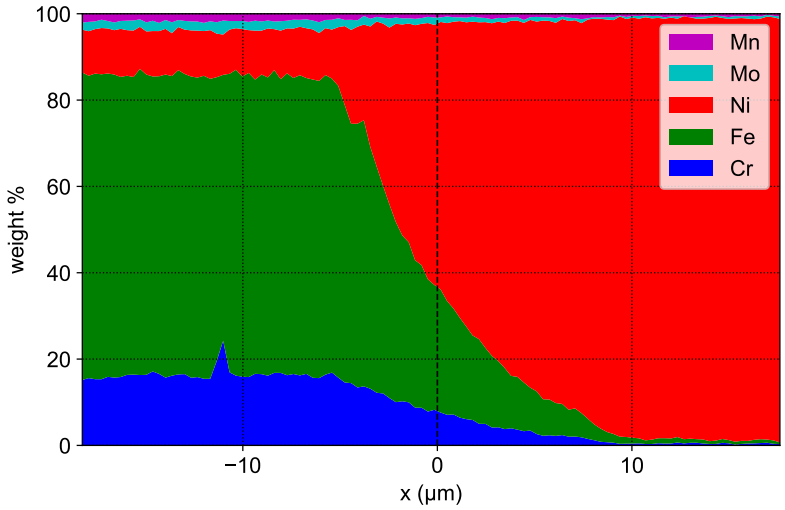

(c) Stacked area plot of major elements (>1wt%)

Figure B.13: Typical EDS line scan data and curve fit for non-thermally-aged SS316L/Ni 200 diffusion couples.

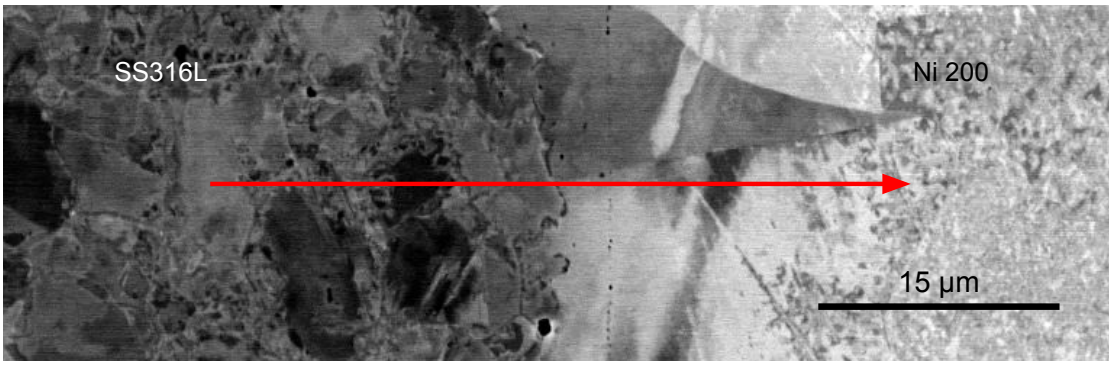

(a) SEM-BSE image of EDS line scan path.

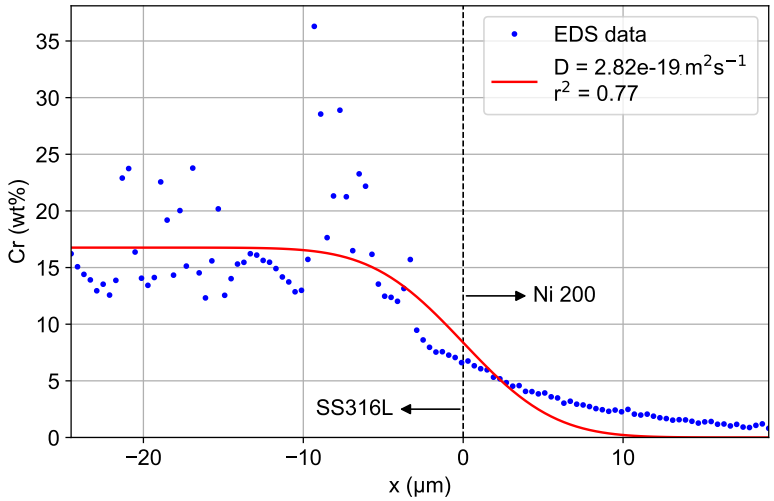

(b) Curve fit of chromium EDS data.

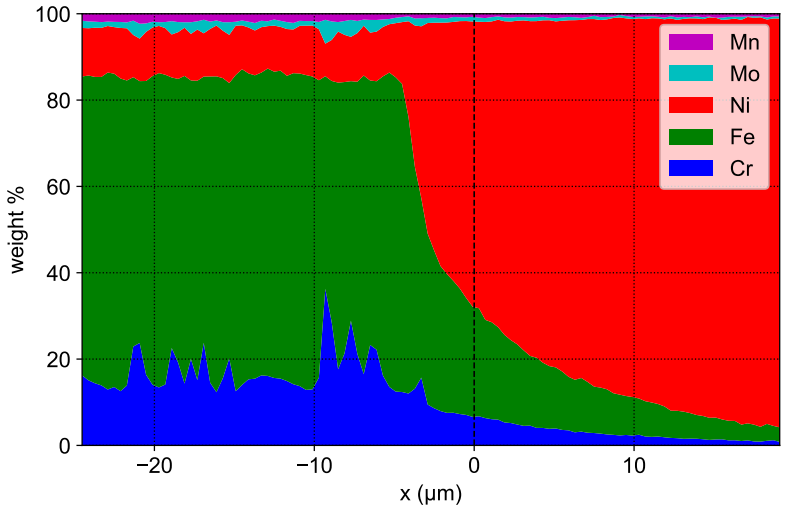

(c) Stacked area plot of major elements (>1wt%)

Figure B.14: Typical EDS line scan data and curve fit for 1460-hour-aged SS316L/Ni 200 diffusion couples.

B.4 Diffusion bonding heat treatment of Ni-plated samples

A batch of Ni-plated samples was exposed to the 900 °C diffusion bonding heat treatment with the same experimental procedures as for actual diffusion bonding but without application of load. Similarly to the Ni-plated samples that weren't exposed to a diffusion bonding heat treatment and were only thermally aged at 700 °C, the Ni-plated samples exposed to a diffusion bonding heat treatment exhibited a lack of interfacial embrittlement, as is seen from the microhardness profiles in Figure B.15. This result supports the conclusion that the formation of carbide precipitates and the resulting interfacial embrittlement in the diffusion couples with Ni 200 is due to the relatively high carbon content in the Ni 200.

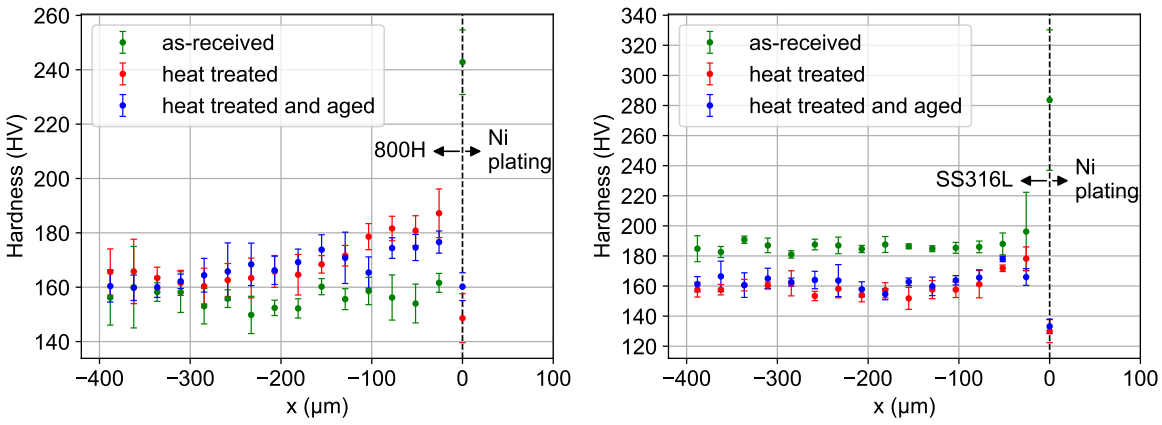

(a) 800H/Ni plating.

(b) SS316L/Ni plating.

Figure B.15: Microhardness profiles of Ni-plated samples exposed to a diffusion bonding heat treatment. In the legend, "heat treated" refers to the 900 °C, 2 h diffusion bonding heat treatment, and "aged" refers to 700 °C exposure for 1461 h.

Appendix C

Phase diagram comparison

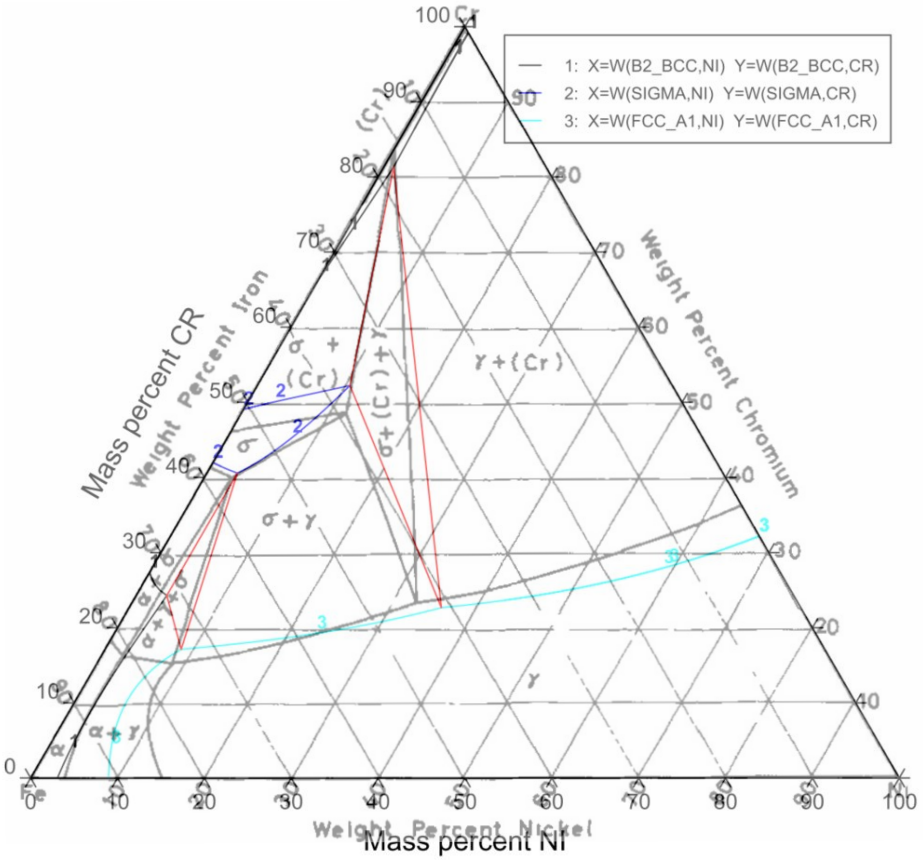

Figure C.1: Overlayed experimental and calculated isothermal phase diagrams for the Cr–Fe–Ni system at 650 °C. The calculated phase diagram has colored lines and was generated with Thermo-Calc. The experimental phase diagram is from [103].

Appendix D

Python scripts

D.1 Main script for calculating diffusion coefficients

```
# -*- coding: utf-8 -*-
"""
Description: This script calls a function that curve fits EDS data and it
    calculates average D values and their confidence intervals for diffusion
    couples of a single material combination and thermal aging time. Similar,
    simpler scripts were used for calculating D for Ni-plated samples and Dt for
    non-thermally-aged diffusion couples.
@author: Cedric Eveleigh
"""

import numpy as np
from numpy import sqrt
from curve_fit_D_function_V4 import curve_fit_D

# ----- User inputs:
element = 'Cr'
plots = True
amp='A1'

# ----- Loading the results csv file:
D_table = np.genfromtxt('D_table_'+element+'.csv',delimiter=',',dtype=float)

# ----- Assigning sample numbers depending on the ampoule:
```

```
if (amp=='A1'):
    sample=['S12','S15','S27']
    a=0
elif (amp=='A2'):
    sample=['S9','S30','S33']
    a=1
elif (amp=='A3'):
    sample=['S18','S21','S24']
    a=2
elif (amp=='A4'):
    sample=['S36','S39','S42']
    a=3
if (amp=='A5'):
    sample=['S13','S16','S28']
    a=0
elif (amp=='A6'):
    sample=['S10','S31','S34']
    a=1
elif (amp=='A7'):
    sample=['S19','S22','S25']
    a=2
elif (amp=='A8'):
    sample=['S37','S40','S43']
    a=3

# ----- Assigning thermal aging time depending on the ampoule:
if (amp=='A1' or amp=='A2' or amp=='A3' or amp=='A4'):
    b=1
    t_hours = 1460
elif (amp=='A5' or amp=='A6' or amp=='A7' or amp=='A8'):
    b=2
    t_hours = 5840

t = t_hours * 3600 #Converting hours to seconds

# ----- Diffusion coefficient calculations:
r_squared=[]
D_700C_all=[]
Dt_total_all=[]
for col in range(0,3): #Looping through the 3 samples per ampoule
    linescan = 0
    D_700C_sample=[]
    Dt_total_sample=[]
```

```
    Dt_900C_sample_avg = D_table[1][col+a*4]
    for loc in range(1,4): #Looping through 9 line scans for a diffusion couple
        for i in range(1,4):
            linescan += 1
            Dt_total_return, D_return, r_squared_return = curve_fit_D(amp,sample[
                col],loc,linescan,element,Dt_900C_sample_avg,t,plots) #Calling
                function for calculating diffusion coefficient and position
                correction factor
            Dt_total_sample.append(Dt_total_return)
            Dt_total_all.append(Dt_total_return)
            D_700C_sample.append(D_return)
            D_700C_all.append(D_return)
            r_squared.append(r_squared_return)
    D_700C_sample_avg = np.mean(D_700C_sample) #Calculating the average diffusion
         coefficient for a diffusion couple
    conf_Dt_900C_sample = D_table[2][col+a*4]
    conf_Dt_total_sample = 1.859548*np.std(Dt_total_sample,ddof=1)/np.sqrt(9)
    conf_D_700C_sample = 1/t*sqrt(conf_Dt_900C_sample**2 + conf_Dt_total_sample
        **2) #Calculating the 95% confidence interval for a diffusion couple
    sample_temp = sample[col]
    D_table[-1+b*4][col+a*4] = sample_temp[1:]
    D_table[0+b*4][col+a*4] = D_700C_sample_avg
    D_table[1+b*4][col+a*4] = conf_D_700C_sample
    D_table[2+b*4][col+a*4] = (t + Dt_900C_sample_avg/D_700C_sample_avg)/3600 #
        Effective aging time for a diffusion couple

#----- Calculating the overall diffusion coefficient, confidence interval, and
    effective diffusion coefficient for each material combination and aging time:
D_700C_all_avg = np.mean(D_700C_all)
conf_Dt_900C_all = D_table[2][3+a*4]
conf_Dt_total_all = 1.705618*np.std(Dt_total_all,ddof=1)/np.sqrt(27)
conf_D_700C_all = 1/t*sqrt(conf_Dt_900C_all**2 + conf_Dt_total_all**2)
D_table[0+b*4][3+a*4] = D_700C_all_avg
D_table[1+b*4][3+a*4] = conf_D_700C_all
D_table[2+b*4][3+a*4] = (t + D_table[1][3+a*4]/D_700C_all_avg)/3600  #Average
    effective aging time
D_table[-1+b*4][3+a*4] = np.mean(r_squared) #Average r-squared value

#----- Saving results to a csv file:
np.savetxt('D_table_'+element+'.csv', D_table, delimiter=',', fmt="%s")
```

D.2 Function for curve fitting EDS data

```
# -*- coding: utf-8 -*-
"""
Description: This script curve fits EDS data for determining interface locations
    and diffusion coefficients.
@author: Cedric Eveleigh
"""

import numpy as np
import matplotlib.pyplot as plt
from numpy import loadtxt, sqrt
from scipy.optimize import curve_fit
from scipy import special #for erfc function

plt.rcParams.update({'font.family': "Arial"})
plt.rcParams.update({'font.size': 13.5})

def curve_fit_D(amp,sample,loc,linescan,element,Dt,t,plots):

    # ----- Data file format differences between SEMs:
    if (amp=='A1' or amp=='A2' or amp=='A3' or amp=='A4'):
        xdata_column = 1
        row_start = 15
    if (amp=='A5' or amp=='A6' or amp=='A7' or amp=='A8'):
        xdata_column = 0
        row_start = 1

    # ----- 1460-hour-aged diffusion couples:
    if (amp=='A1'):
        folder = '../Analysis - EDS_(CANS)/2018.03.23 A1 - S12,S15,S27'
        cladding='Ni 200'
        struct_alloy='800H'
        clad_label_height=17.5
        xscaling = 0.657
        column_Cr = 2
        column_Fe = 3
        column_Ni = 4
    elif (amp=='A2'):
        folder = '../Analysis - EDS_(CANS)/2018.03.27 A2 - S9,S30,S33'
        cladding='Hastelloy N'
        struct_alloy='800H'
```

```
        clad_label_height=2.5
        xscaling = 0.657
        column_Mo = 2
        column_Cr = 3
        column_Fe = 4
        column_Ni = 5
    elif (amp=='A3'):
        folder = '../Analysis — EDS_(CANS)/2018.04.03 A3 — S18,S21,S24'
        cladding='Ni 200'
        struct_alloy='SS316L'
        clad_label_height=12.5
        xscaling = 0.657
        column_Mo = 2
        column_Cr = 3
        column_Mn = 4
        column_Fe = 5
        column_Ni = 6
    elif (amp=='A4'):
        folder = '../Analysis — EDS_(CANS)/2018.04.10 A4 — S36,S39,S42'
        cladding='Hastelloy N'
        struct_alloy='SS316L'
        clad_label_height=2.5
        xscaling = 0.657
        column_Mo = 2
        column_Cr = 3
        column_Mn = 4
        column_Fe = 5
        column_Ni = 6

    # ———— 5840—hour—aged diffusion couples:
    elif (amp=='A5'):
        folder = '../Analysis — EDS_(CCEM)/2018.09.25 A5 — S13,S16,S28'
        cladding='Ni 200'
        struct_alloy='800H'
        clad_label_height=17.5
        xscaling = 0.980392
        column_Cr = 1
        column_Fe = 2
        column_Ni = 3
    elif (amp=='A6'):
        folder = '../Analysis — EDS_(CCEM)/2018.09.29 A6 — S10,S31,S34'
        cladding='Hastelloy N'
        struct_alloy='800H'
```

```
        clad_label_height=2.5
        xscaling = 0.980392
        column_Mo = 4
        column_Cr = 1
        column_Fe = 2
        column_Ni = 3
    elif (amp=='A7'):
        folder = '../Analysis — EDS_(CCEM)/2018.10.02 A7 — S19,S22,S25'
        cladding='Ni 200'
        struct_alloy='SS316L'
        clad_label_height=12.5
        xscaling = 0.980392
        column_Mo = 5
        column_Cr = 1
        column_Mn = 2
        column_Fe = 3
        column_Ni = 4
    elif (amp=='A8'):
        folder = '../Analysis — EDS_(CCEM)/2018.10.03 A8 — S37,S40,S43'
        cladding='Hastelloy N'
        struct_alloy='SS316L'
        clad_label_height=2.5
        xscaling = 0.980392
        row_start = 1
        column_Mo = 5
        column_Cr = 1
        column_Mn = 2
        column_Fe = 3
        column_Ni = 4

    if element=='Cr':
        column = column_Cr
    if element=='Fe':
        column = column_Fe
    if element=='Ni':
        column = column_Ni
    if element=='Mo':
        column = column_Mo
    if element=='Mn':
        column = column_Mn

    # ——— Assigning concentration values:
    if struct_alloy=='800H':
```

```
        Cr_b = 20.51
        Fe_b = 47
        Ni_b = 30.3
        Mo_b = 0
        Mn_b = 0.57
    elif struct_alloy=='SS316L':
        Cr_b = 16.76
        Fe_b = 68.93
        Ni_b = 10.03
        Mo_b = 2.02
        Mn_b = 1.55
    if cladding=='Ni 200':
        Cr_c = 0
        Fe_c = 0
        Ni_c = 99.2
        Mo_c = 0
        Mn_c = 0.25
    elif cladding=='Hastelloy N':
        Cr_c = 7.22
        Fe_c = 4.13
        Ni_c = 70.74
        Mo_c = 16.82
        Mn_c = 0.49

    # ----- Assigning the element concentrations to the global concentration
        variables:
    if element=='Cr':
        C_b = Cr_b
        C_c = Cr_c
    elif element=='Fe':
        C_b = Fe_b
        C_c = Fe_c
    elif element=='Ni':
        C_b = Ni_b
        C_c = Ni_c
    elif element=='Mo':
        C_b = Mo_b
        C_c = Mo_c
    elif element=='Mn':
        C_b = Mn_b
        C_c = Mn_c

    orientation = 1
```

```
# ----- Reversing curve fit function if concentration in cladding is greater
    than in base alloy:
if C_c>C_b:
    temp = C_c
    C_c=C_b
    C_b=temp
    orientation = -1

# ----- Extracting raw EDS data:
filename = folder+'/'+sample+'/'+sample+'_loc'+str(loc)+'_line'+str(linescan)
    +'.csv'
data = loadtxt(filename, delimiter=',',skiprows=row_start)
xdata = data[0:, xdata_column]*xscaling #Position data
ydata = data[0:, column] #Concentration data
xhalf = max(xdata)/2
if max(xdata)>30:
    xtick_spacing = 10
else:
    xtick_spacing = 5

# ----- Curve fitting:
def func(x, Dt_total, corr):
    return C_c + (C_b-C_c)/2 * special.erfc(orientation*(x-corr)/(2 * sqrt(
        Dt_total))/1e6) #1e6 is correction for um to m
index = ~(np.isnan(xdata) | np.isnan(ydata)) #For skipping NaN values (Mo
    concentration values that were manually selected as outliers)
popt, pcov = curve_fit(func, xdata[index], ydata[index], p0=[1e-12,xhalf])
D =  (popt[0] - Dt)/t #Calculating the 700C diffusion coefficient
fig = plt.figure()
xdata = xdata - popt[1]

# ----- Creating a plot:
fig = plt.figure(figsize=(7.5,4.5))
ax = fig.add_subplot(1, 1, 1)
plt.subplots_adjust(left=0.1, right=0.9, top=0.95, bottom=0.125)
y_ticks = np.arange(0, 101, 5)
ax.set_yticks(y_ticks)
x_ticks = np.arange(-1e3, 1e3, xtick_spacing)
ax.set_xticks(x_ticks)
plt.axvline(x=0, color='w',linewidth=1)
plt.axvline(x=0, color='k',linestyle='--', linewidth=1)
plt.plot(xdata, ydata, 'bo', markersize=2.5, label='EDS data') #Plotting EDS
    data
```

```
residuals = ydata[index] - func((xdata[index] + popt[1]), *popt)
ss_res = np.sum(residuals**2)
ss_tot = np.sum((ydata[index] - np.mean(ydata[index]))**2)
r_squared = 1 - (ss_res / ss_tot)
plt.plot(xdata, func((xdata + popt[1]), *popt), 'r-', label='D = %.2e\u202Fm$
    ^2$s$^{-1}$\nr$^2$ = %1.2f' % (D,r_squared)) #Plotting curve fit
plt.xlabel('x (\u03bcm)') #\u03bc is unicode for mu
plt.ylabel(element+' (wt%)')
plt.legend()
plt.xlim(min(xdata),max(xdata))
plt.ylim(ymin=0)
plt.grid(True)
label_xpos = 0.1*(max(xdata)-min(xdata))
plt.annotate(cladding, xy=(0,clad_label_height), xytext=(label_xpos,
    clad_label_height), ha="left", va="center",
            arrowprops=dict(arrowstyle="<|-",facecolor='black'),)
plt.annotate(struct_alloy, xy=(0,2.5), xytext=(-label_xpos,2.5), ha="right",
    va="center",
            arrowprops=dict(arrowstyle="<|-",facecolor='black'),)
if plots==True:
    filename = filename[:-4] #removes .csv from the filename
    fig.savefig('Figs/'+sample+'_'+element+str(linescan)+'.pdf')
print (sample+'_'+element+str(linescan))
plt.show()
plt.close("all")

return(popt[0],D,r_squared) #Returns Dt_total for confidence interval
    calculations, calculated diffusion coefficient, and r-squared value
```